TELAC REPORT 95-8

ANALYSIS OF COMPOSITE ABLATORS USING MASSIVELY PARALLEL COMPUTATION

David Shia
Research Assistant

August, 1995

ANALYSIS OF COMPOSITE ABLATORS USING MASSIVELY PARALLEL COMPUTATION

by

David Shia

Submitted to the Department of Aeronautics and Astronautics on August 11th, 1995 in partial fulfillment of the requirements for the Degree of Master of Science in Aeronautics and Astronautics

ABSTRACT

In this work, the feasibility of using massively parallel computation to study the response of ablative materials is investigated. Explicit and implicit finite difference methods are used on a massively parallel computer, the Thinking Machines CM-5. The governing equations are a set of nonlinear partial differential equations. The governing equations are developed for three sample problems: (1) transpiration cooling, (2) ablative composite plate, and (3) restrained thermal growth testing. The transpiration cooling problem is solved using a solution scheme based solely on the explicit finite difference method. The results are compared with available analytical steady-state through-thickness temperature and pressure distributions and good agreement between the numerical and analytical solutions is found. It is also found that a solution scheme based on the explicit finite difference method has the following advantages: incorporates complex physics easily, results in a simple algorithm, and is easily parallelizable. However, a solution scheme of this kind needs very small time steps to maintain stability. A solution scheme based on the implicit finite difference method has the advantage that it does not require very small times steps to maintain stability. However, this kind of solution scheme has the disadvantages that complex physics cannot be easily incorporated into the algorithm and that the solution scheme is difficult to parallelize. A hybrid solution scheme is then developed to combine the strengths of the explicit and implicit finite difference methods and minimize their weaknesses. This is achieved by identifying the critical time scale associated with the governing equations and applying the appropriate finite difference method according to this critical time scale. The hybrid solution scheme is then applied to the ablative composite plate and restrained thermal growth problems. The gas storage term is included in the explicit pressure calculation of both problems. Results from ablative composite plate problems are compared with previous numerical results which did not include the gas storage term. It is found that the through-thickness temperature distribution is not affected much by the gas storage term. However, the through-thickness pressure and stress distributions, and the extent of chemical reactions are different from the previous numerical results. Two types of chemical reaction models are used in the restrained thermal growth testing problem: (1) pressure-independent Arrhenius type rate equations and (2) pressure-dependent Arrhenius type rate equations. The numerical results are compared to experimental results and the pressure-dependent model is able to capture the trend better than the pressure-independent one. Finally, a performance study is done on the hybrid algorithm using the ablative composite plate problem. It is found that there is a good speedup of performance on the CM-5. For 32 CPUs, the speedup of performance is 20. The efficiency of the algorithm is found to be a function of the size and execution time of a given problem and the effective parallelization of the algorithm. It also seems that there is an optimum number of CPUs to use for a given problem.

Thesis Supervisor: Prof. Hugh L. McManus
Title: Class of 1943 Career Development Assistant Professor

Acknowledgments

I like to begin by thanking Professor McManus for his guidance and financial support during my two year study at MIT. I also would like to thank Professor Lagace for his leadership of the laboratory. Encouragement and supports from everyone in TELAC are deeply appreciated as well. Special thanks go to: Hary, Brian, and Mark. Hary for his guidance and mentorship. Brian for his help with the thesis writing. Mark for teaching me the post-up move.

Finally, I would like to thank my family for their constant financial and spiritual support.

Foreword

This work was performed in the Technology Laboratory for Advanced Composites (TELAC) in the Department of Aeronautics and Astronautics at the Massachusetts Institute of Technology . This work was sponsored by the NASA Marshall grant NAG8-295.

Table of Contents

List of Figures

List of Tables

Nomenclature

A	constant material parameter for the transpiration cooling problem
A_{o_k}	Arrhenius rate constant for the kth reaction
B	constant material parameter for the transpiration cooling problem
c	damping coefficient or constant in Eqn. 4-39 depending on context
c_k	degree of conversion for the kth reaction
C	constant material parameter for the transpiration cooling problem
C_{P_c}	specific heat of the porous charred solid
C_{P_g}	specific heat of the gas
C_{P_i}	specific heat of the ith substance
C_{P_l}	specific heat of the absorbed moisture
C_{P_v}	specific heat of the porous virgin solid
D	constant material parameter for the transpiration cooling problem
e	efficiency
E	overall internal energy or Young's modulus depending on context
E_{a_k}	Arrhenius activation energy of the kth reaction
E_{gen_k}	heat generated by the kth chemical reaction
h	thickness of the plate
h_c	enthalpy per unit mass of charred solid
h_e	enthalpy per unit mass of evaporation gas
h_g	enthalpy per unit mass of the gas

h_i	enthalpy per unit mass of the ith substance
h_l	enthalpy per unit mass of absorbed moisture
h_p	enthalpy per unit mass of pyrolysis gas
h_s	enthalpy per unit mass of virgin solid
k	thermal conductivity
K_z	area-average thermal conductivity in the z direction
K_{zi}^j	area-average thermal conductivity in the z direction at the ith node and jth time step
l_r	reference length in Eqn. 4-40
L	length of the plate
M	average gas molecular weight
m_c	mass of charred solid per unit control volume
m_i	mass of ith substance per unit control volume
m_g	mass of gas per unit control volume
m_l	mass of absorbed moisture per unit control volume
m_s	mass of virgin solid per unit control volume
$\hat{m}_g$	mass flux of gas
$\hat{m}_{gi}^j$	mass flux of gas at the ith node and jth time step
MC	moisture content
n_k	Arrhenius order of the kth reaction
p	effective parallelization
P	internal pressure
P_b	ambient pressure
P_1	fixed boundary pressure at z = 0 for the transpiration cooling problem
P_2	fixed boundary pressure at z = h for the transpiration cooling problem
P_i^j	pressure at the ith node and jth time step

q_{cond}	conduction heat flux
q_{conv}	convection heat flux
Q_c	effective heat of charring reaction
Q_w	effective heat of evaporation reaction
$\overline{Q}_c$	heat of charring reaction
$\overline{Q}_w$	heat of evaporation reaction
$\overline{Q}_k$	chemical heat of reaction of the kth reaction
r	nondimensional constant in Eqn. 2-3
r_e	rate of gas mass generation due to evaporation
r_g	rate of gas mass generation
r_i	rate of mass generation of the ith substance
r_{ik}	rate of generation of substance i by reaction k
r_p	rate of gas mass generation due to pyrolysis
R	universal gas constant
R_c	vapor formation rate
R_k	rate of reaction of the kth reaction
R_w	char formation rate
S	speedup
S_{ijkl}	compliance of the porous solid under mechanical loading
$S_{max,ideal}$	maximum ideal speedup
t	time
t_{c1}	first critical time scale in Eqn. 4-39
t_{c2}	second critical time scale in Eqn. 4-39
t_{cond}	conduction time scale
t_{ex}	excess time
t_{pc1}	first time scale associated with governing equation for pressure (Eqn. 4-27)

t_{pc2}	second time scale associated with governing equation for pressure (Eqn. 4-27)
t_{pc3}	third time scale associated with governing equation for pressure (Eqn. 4-27)
t_{solid}	solid time scale
t_N	execution time using N processors
t_{Tc}	critical time scale associated with Eqn. 4-47
t_{Tc1}	first time scale associated with governing equation for temperature (Eqn. 4-28)
t_{Tc2}	second time scale associated with governing equation for temperature (Eqn. 4-28)
t_{Tc3}	first time scale associated with governing equation for temperature (Eqn. 4-28)
t_1	execution time using one processor
T	temperature
T_1	fixed boundary temperature at z = 0 for the transpiration cooling problem
T_2	fixed boundary temperature at z = h for the transpiration cooling problem
T_{bc}	temperature at which charring begins
T_{bw}	temperature at which evaporation begins
T_{ec}	temperature at which charring ends
T_{ew}	temperature at which evaporation ends
$T_{sat}(P)$	saturation temperature of gas at pressure P
T_i^j	temperature at the ith node and jth time step
u	scalar quantity in Eqn. 4-39
u_i	displacement vector of the porous solid in the ith direction
u_{xi}^j	displacement of the porous solid in the x direction at the ith node and jth time step

u_{yi}^{j}	displacement of the porous solid in the y direction at the ith node and jth time step
u_{zi}^{j}	displacement of the porous solid in the z direction at the ith node and jth time step
v_c	charred solid volume
v_s	virgin solid volume
V_D	velocity of gas flowing inside a porous solid
W	width of the plate
x_1-x_2-x_3	on-axis coordinate system
x-y-z	off-axis coordinate system
α	Amdahl's fraction
α_e	equivalent Amdahl's fraction
α_{ij}	thermal expansion tensor
β_{ij}	moisture expansion tensor
χ_{ij}	charring expansion tensor
δ_{ij}	Kronecker delta
$\Delta(MC)$	changes from a reference value of absorbed moisture content
ΔP	changes from a reference value of the pressure
Δt	time step
ΔT	changes from a reference value of the temperature
Δv_c	changes from a reference value of the char volume
Δx	distance between two neighboring nodes
Δz	distance between two neighboring nodes
ε_{ij}	total strain tensor
ϕ	overall porosity (virgin + charred)
ϕ_c	charred solid porosity
ϕ_s	virigin solid porosity

Φ	ply angle
Λ_{ij}	compliance of the porous solid subjected to an internal pressure
γ	permeability
η	combined heat capacity of the system
μ	average gas viscosity
ν	constant in Eqn. 4-39
ω_n	circular natural frequency
θ	fiber angle
ρ_c	intrinsic density of the porous charred solid
ρ_g	intrinsic gas density inside the pores
ρ_{gi}^j	intrinsic gas density inside the pores at the ith node and jth time step
ρ_s	intrinsic density of the porous solid
σ_{ij}	total stress tensor
σ_{ij}^m	mechanical stress tensor
ς	nondimensional damping coefficient
υ	Poisson's ratio
ξ_k	arbitrary small reaction rate for reaction k

CHAPTER 1

INTRODUCTION

Ablative composite materials have been used in a broad range of applications. The production of solid fuel rocket motors, planetary-entry probes, and reentry vehicles was made possible by these materials. Ablatives are used to protect structures from extreme temperature environments. When these materials are exposed to a high heat flux environment, extreme thermal gradients, internal pressures due to chemical reactions, and thermal and mechanical stresses all develop, which can cause premature failure. Hence, to make full use of these materials, all of these aspects of their response must be more completely understood.

The physical phenomena that happen inside these materials can be characterized by the following processes. When the surface of the ablative is exposed to a high temperature environment, heat is conducted into the material. The temperature of the material below the surface will then rise and a temperature gradient is established inside the material. When the temperature inside the material reaches a high enough value, chemical reactions take place. Gases are generated due to these reactions. Due to the relatively low permeability of the material, these gases are trapped in the material and cause internal pressures to develop. Both the temperature gradient and internal pressure will cause stresses to develop in the materials. Sometimes the values of these stresses are high enough to cause premature failure of the ablative materials. The response of the ablative materials

undergoing these processes needs to be understood to prevent premature failure.

There are typically two approaches to study the responses of composite ablatives. The experimental approach usually requires large scale test specimens which can be prohibitively expensive to manufacture. Moreover, these experiments do not always reveal the details of the underlying physical processes. The analytical approach can give insight to the physical processes that lead to premature failure of such materials if the modeling is done properly. However, in order to obtain these insights, the nonlinear partial differential equations of a very complete analytical model need to be solved. Closed-form solutions are impossible to obtain in most cases. Therefore, numerical solutions are needed.

Two major numerical solution schemes that have been applied to this problem are the finite element method (FEM) and the finite difference method (FDM). In both methods, some simplifications must be made in the governing equations in order to keep the computation tractable. However, it is important that sufficient complexities are included in the computations so that the predicted results can be used with confidence. A great deal of computational power is needed to allow such complexities to be included in a solution algorithm. With the recent arrival of massively parallel computers such as the Thinking Machines' Connection Machine 5 (CM-5), enough computational power has become available to both greatly increase the accuracy of such solutions and lower their turn-around time.

However, to make efficient uses of massively parallel computers, an appropriate solution algorithm needs to be developed. Relatively speaking, FDM results in simpler algorithms than FEM on a parallel computer. Simpler algorithms allow more complexities to be incorporated into an FDM

algorithm. Results computed based on this algorithm will simulate reality more closely. Therefore, a solution algorithm based on FDM is developed on the CM-5 in this work.

In FDM, there are two major types of solutions scheme. They are the explicit finite difference method (EFDM) and the implicit finite difference method (IFDM). The two schemes differ in the way they approximate the derivatives in the governing equations. There are two major advantages of using EFDM. The first advantage is that it leads to a simple algorithm which is easy to program. This implies that complex nonlinear physics is relatively easy to incorporate into the program. The second advantage is that EFDM is well suited to parallel computation. At each time step, the difference equations can be solved at all nodes simultaneously and the solution of the equations at each node requires knowledge only of the states of its immediate neighboring nodes. This minimizes the required communication between processors, keeping the parallel computation efficient.

The major drawback of the EFDM is that computations need to be done at relatively small time steps to maintain stability. The allowable time steps are usually limited by the fastest physical process associated with the problem. In the ablative case, the fastest physical processes are the deformations of the solid material and the internal flow of gases. These two processes can limit the time step to as small as 10^{-6} second. Therefore, modeling using a fully-explicit scheme may be impractical for a typical simulation time which is on the order of 100 seconds. A hybrid algorithm which will be discussed later is proposed to alleviate the time-step problem.

In this work, approaches to solve ablation type problems on massively parallel computers are explored. Analytical models and numerical solution schemes are developed to solve several physical problems of interest.

The three physical problems considered are: (1) transpiration cooling of a plate, (2) ablation of a composite plate, and (3) restrained thermal growth testing. The transpiration cooling problem is used to verify the EFDM. The internal pressure, temperature, and stress distributions are obtained using EFDM and compared to available analytical solutions. The ablative composite plate problem is used to demonstrate the capability of the EFDM scheme to incorporate complex physics and solve parctical problems. A typical solid rocket motor nozzle liner problem is solved, and the solution compared to previous numerical solutions of the problem. The restrained thermal growth problem is used to demonstrate the adaptability of the numerical method. Parametric studies are performed on the effects of different chemical reaction models and the results compared with experimental data.

The present work is organized as follows. In Chapter 2, previous work and relevant background on massively parallel computing are discussed. A concise problem statement is given in Chapter 3. In Chapter 4, the general governing equations are developed. The governing equations are then simplified appropriately for each of the three cases studied: transpiration cooling, ablative composite plate, and restrained thermal growth. The results are presented in Chapter 5. The performance of the hybrid algorithm on the CM-5 is also presented in Chapter 5. The conclusions drawn from the results and recommendations for future research are presented in Chapter 6.

CHAPTER 2

BACKGROUND

The first section of this chapter contains a discussion of the previous analytical and experimental work done in the area of ablative composite materials. A brief discussion of previous work on numerical schemes then follows. In the second section of this chapter, relevant information concerning parallel computation on machines such as the CM-5 is presented. The first part of this section contains a brief discussion on the architecture of the CM-5, as well as how codes using CM-FORTRAN [1] should be written to take advantage of the architecture. In the second part of this section, the metrics for measuring the performance of parallelized codes is presented.

2.1 Experimental Investigations and Modeling

The earliest work done on natural ablative materials was done on wood for fire-retarding purposes (see [2] for more early history). For man-made ablatives, one of the earlier works was done by Moyer and Rindal [3] in 1963 in which the thermal response of materials used as heat shields for reentry vehicles was investigated.

Henderson and his colleagues did extensive experimental work to determine the properties of glass-phenolic ablative composite materials in the early 1980's [4]. Stokes [5] and Hubbert [6] performed many experiments to study the material response of ablative composite materials. The one of particular interest to this study is the restrained thermal growth (RTG) test.

McManus and Springer [7] also did some experimental work on carbon-phenolic ablative materials to validate his model and the CHAR computer code. Florio et al. [8] experimentally determined the volumetric heat transfer coefficient in decomposing polymer composites. This volumetric heat transfer coefficient was used in their study of the assumption of local thermal equilibrium [9].

Much work has been done on modeling the behavior of ablative composite materials. Henderson developed a simple model which included an Arrhenius reaction model, an energy equation, and a steady-state mass flow equation [4]. The model was later refined to include a mass flow equation based on Darcy's law and the thermal expansion of the solid material [10]. These models predicted the internal pressure and temperature predictions distributions but did not give stress distributions. Kuhlmann [11], McManus [12], Sullivan [13], and Weiler [14, 15] developed models which also included the stress distributions inside the solid material. This was achieved by applying the theory of poroelasticity [16-21] in combination with the existing thermochemical and gas flow theories to predict the material's temperature, chemical state, internal pressure, and stresses simultaneously. Each author used a different approach to derive the coupled thermoporoelastic equations. These governing equations are highly nonlinear due to the fact that the coefficients in the constitutive relations are functions of the independent variables (temperatures, pressures, stresses, etc.). When complex chemical reaction models are used, governing equations can be made even more nonlinear. For example, Tai [22] developed a new evaporation model for ablative composite materials which is a function of temperature and pressure.

Sullivan [23, 24] proposed a thermodynamic approach to derive a new set of constitutive relations for decomposing ablative materials. In general, the coefficients in the newly developed constitutive relations are functions of the independent variables and thus the governing equations are highly nonlinear. This approach was proposed to overcome the limitations of the previous models which were all based on porous media flow and poroelasticity. These limitations are: (1) gases generated from chemical reactions act together as a single equivalent fluid, (2) a well-defined boundary exists between the fluid and solid constituents where mechanical equilibrium is maintained and (3) the forces that exists between the solid and fluid constituents are purely mechanical in nature. However, certain carbon fibers used in polymeric composites are known to be hydrophilic (i.e. attract water) when heated to high temperatures [25]. This is due to the presence of activated carbon sites on their surface. Chemical forces then develop between the carbon fibers and water molecules liberated from the resin. These forces may have significant influence on the mechanical behavior of the material. In the only work to date on this problem, chemisorption of H_2O in the matrix was dealt with on an ad-hoc basis in the model developed by Tai and McManus [22].

2.2 Numerical Methods

Due to the complex physics occurring inside an ablative composite material, the models developed so far require the solution of a set of highly nonlinear partial differential equations. Closed form solutions for these governing equations are impossible to obtain. Therefore, numerical schemes have been used. Two types of numerical schemes have been adopted by researchers in this field. Sullivan, Kuhlmann, and Weiler adopted the finite

element method. Other researchers such as Henderson and McManus have used the finite difference method. The finite element method has the advantage that geometry and boundary conditions can be accurately modeled. The major disadvantage of the finite element method is the difficulty in incorporating complex physics (nonlinear constitutive laws for example). The advantage of the finite difference method is that it is relatively easy to incorporate complex physics. The disadvantage of the finite difference method is that geometry and boundary conditions are harder to model than in the finite element method. Within the finite difference method, there are two ways a differential equation can be approximated: (1) the explicit finite difference method (EFDM) and (2) the implicit finite difference method (IFDM). It is easier to incorporate complex physics into the EFDM than the IFDM. However, the EFDM generally requires more computational power than the IFDM. Henderson's original work used the EFDM, because the EFDM was relatively easy to implement [4]. However, it was later abandoned due to limited computational power available at that time. With the recent advances in computational power, the explicit finite difference method is again becoming a viable method for solving the governing equations.

In this work, a numerical scheme called the hybrid algorithm is developed to solve the governing equations. The hybrid algorithm uses both the EFDM and the IFDM to solve the governing equations. For this reason, a brief discussion of these methods is presented using an example based on a simple 1-D heat transfer equation.

The 1-D heat transfer equation is:

$$\frac{\partial T}{\partial t} = k \frac{\partial^2 T}{\partial x^2} \tag{2-1}$$

The EFDM, using forward difference in time and central difference in space [25], can be used to derive the following difference equation:

$$\frac{T_i^{j+1} - T_i^j}{\Delta t} = k \frac{T_{i+1}^j - 2T_i^j + T_{i-1}^j}{\Delta x^2} \tag{2-2}$$

where T_i^j is the temperature at the jth time step and the ith node, Δt is the time step, and Δx is the spacing between two nodes. By rearranging Eqn. 2-2, an expression for T_i^{j+1} is obtained:

$$T_i^{j+1} = rT_{i-1}^j + (1-2r)T_i^j + rT_{i+1}^j \tag{2-3}$$

where $r = (k\Delta t)/\Delta x^2$. It can be seen from Eqn. (2-3) that the value of temperature at the next time step for a given node is found from the known current values of temperature of that node and its immediate neighbors. A finite difference method where the unknown values can be expressed directly in terms of the known values is called an EFDM. The scheme used in Eqn. (2-3) is illustrated graphically in Figure 2-1. In Figure 2-1, the y axis represents time and x axis represents nodal position. As shown in Figure 2-1, the value of temperature at the ith nodal point and $(j+1)$th time step is updated by the known values of the neighboring nodes ($(i-1)$th, ith, and $(i+1)$th nodes) at the jth time step. Eqn. 2-3 is stable for time step sizes that are less than ($\Delta x^2/2k$) [25].

To illustrate IFDM, the Crank-Nicholson scheme is used [26]. In this scheme, the same difference technique as the one in EFDM is used. The only difference is that the spatial derivatives are approximated by taking the average of its central difference at the jth and $j+1$th time step. By applying the IFDM to Eqn. 2-1 the resulting difference equation is:

$$\frac{T_i^{j+1} - T_i^j}{\Delta t} = \frac{k}{2}\left(\frac{T_{i+1}^j - 2T_i^j + T_{i-1}^j}{\Delta x^2} + \frac{T_{i+1}^{j+1} - 2T_i^{j+1} + T_{i-1}^{j+1}}{\Delta x^2} \right) \tag{2-4}$$

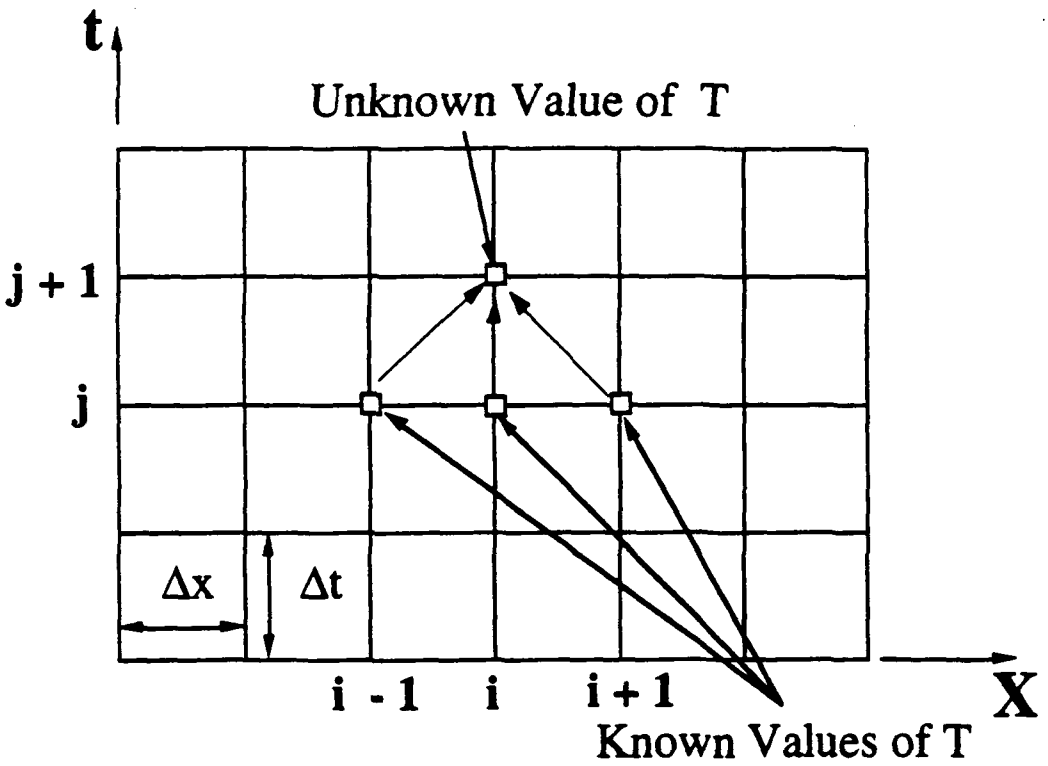

Figure 2-1. Explicit finite difference method for the simple heat conduction equation (Eqn. 2-3).

Rearranging Eqn. 2-4 into a more convenient form,

$$\frac{r}{2}T_{i-1}^{j+1} - (1+r)T_i^{j+1} + \frac{r}{2}T_{i-1}^{j+1} = \frac{-r}{2}T_{i+1}^{j} + (r-1)T_i^{j} - \frac{r}{2}T_{i-1}^{j} \qquad (2\text{-}5)$$

It can be seen readily from Eqn. 2-5 that the value of temperature at a given node is dependent on both the known (jth time step) and the unknown ($j+1$th time step) values of temperature at that and neighboring nodes. The value T_i^{j+1} cannot be solved directly from Eqn. 2-5 as in Eqn. 2-3. If there are N internal nodal points then at the $j+1$th time step Eqn. 2-5 gives N simultaneous equations for the N unknown values in terms of the boundary and jth time step values. Such a difference method is called the IFDM. The IFDM used in Eqn. 2-5 is illustrated graphically in Figure 2-2. The value T_i^{j+1} depends on both the current (jth time step) and future ($j+1$th time step) value of temperature at that and neighboring nodes. The future value of the neighboring nodes depend on the values of their neighbors, and so on, until the problem becomes fully coupled.

If the coefficient (k in our example) is itself a function of temperature, Eqn. 2-1 becomes non-linear. This presents no complication to solving the EFDM (Eqn. 2-3), as k is calculated at timestep j and is thus known. Equation 2-5 requires values of k at both timestep j and timestep $j+1$; thus the matrix solution becomes nonlinear and must be solved iteratively. When k is a constant, Eqn. 2-5 is stable for all positive values of time step size [26]. However, a reasonable time step size must be used to maintain accuracy.

The key characteristics of EFDM and IFDM are shown in the above example. In EFDM, the solution can be obtained from known neighboring nodal values. However, the time step size must be smaller than a given value for EFDM to remain stable. A matrix solution is needed in IFDM and it may need to be iterated to solve non-linear problems. IFDM is more stable than

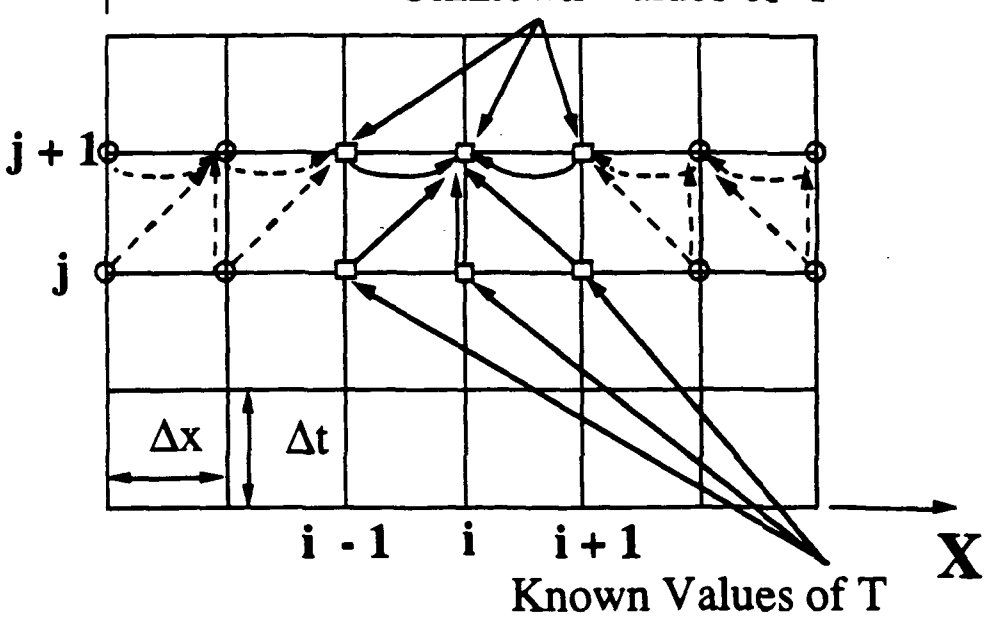

Figure 2-2. Implicit finite difference method (Crank-Nicholson Scheme) for the simple heat conduction equation (Eqn. 2-3).

EFDM. In the above example, the IFDM is stable for all positive values of time step size when k is constant . EFDM is more attractive than IFDM for implementation on parallel computers, since the algorithm can be parallelized more easily (the solution at each node can be obtained directly from known neighboring nodal values). Although it is easier to implement EFDM on parallel computer, sometimes the time step size necessary for stability may become too small for EFDM to be practical. In that case, one may need to use IFDM.

2.3 Parallel Computing on the CM-5

The Connection Machines CM-5 is a massively parallel, SIMD (Single-Instruction Multiple-Data) and MIMD (Multiple-Instruction Multiple-Data) computer. Machines of this type consist of a very large number of processing elements. Each parallel processing element has its own physically connected memory. Intense communication takes place between the processors when data needs to be moved from one memory to another. Efficient algorithms will minimize this communication. For large numerical codes, the regularity of the data structure and the absence of sequential operations are important factors to minimize interprocessor communications on the CM-5 [27].

A schematic drawing of the CM architecture is shown in Figure 2-3. The serial control processor directs the actions of a set of parallel processors. The serial controller also performs all sequential operations. During such operations, the parallel processors do nothing. The parallel processors act on data elements stored in their local memories. Parallel processors are most efficient when acting on large data set, each element of which can be acted on independently. The entire set can then be acted on simultaneously, one processor working on each element.

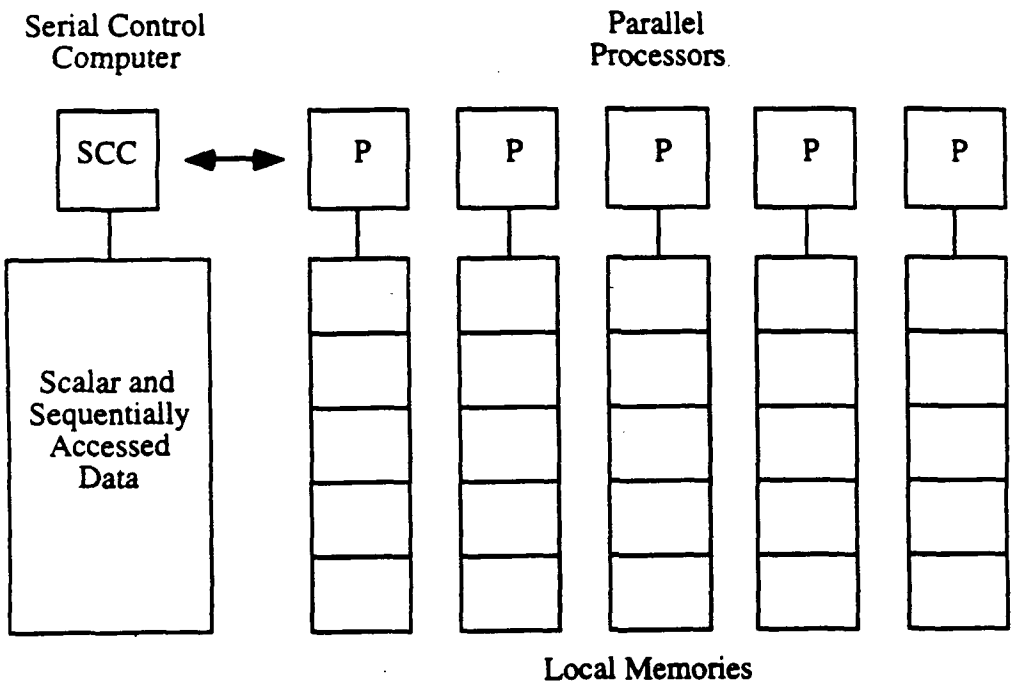

Figure 2-3. Connection Machine architecture [1].

CM FORTRAN is the language used here to implement the solution algorithm on the CM-5 machine. It allows data parallel programming in a language familiar to most researchers since it is actually based on FORTRAN 90. A full description of CM FORTRAN may be found in the Connection Machine documentation [1].

CM FORTRAN does not require the programmer to be concerned about the details of parallelization. The CM FORTRAN compiler performs the parallelization after the code is written. However, the programmer needs to arrange the data structure so that the compiler can parallelize the code in the most optimal way. Optimal parallelization can be achieved by the compiler when data structure is arranged into different sets of *conformable arrays* (arrays that are the same size and shape) and all operations are performed with conformable arrays from the same set. This allows the compiler to assign conformable arrays to the same parallel processor set. When this is done, operations are performed in parallel without communications between different sets of processors.

With the above ideas in mind, it can be seen that the EFDM is a suitable method to solve differential equations on the CM-5. Take the simple heat conduction equation (Eqn. 2-1) as an example. Eqn. 2-3 is obtained using EFDM. For demonstration purpose, it is assumed that there are five nodal points in the mesh. Using the EOSHIFT function, a utility in CM FORTRAN that allows the location of array elements to be shifted by a specified amount, three independent conformable arrays containing the values of, T_i^j, T_{i-1}^j, and T_{i+1}^j at all nodes can be formed. The EOSHIFT function inserts specified values in the appropriate end of an array which are used to define boundary conditions. Then the values of T_i^{j+1} at all nodes can

be obtained with a single operation [28]. This process is illustrated in Figure 2-4. For this reason, the EFDM is very efficient for parallel computations.

The opposite is true for the IFDM. As shown in Eqn. 2-5, the unknowns values of temperature are coupled together. Therefore, in order to obtain solutions, a system of equations needs to be solved at the same time. Typical numerical schemes available for solving systems of equations (Gauss elimination, LU decomposition, and Gauss-Seidel) involve mainly sequential operations which require intense interprocessor communication during which the parallel processors remain idle. Therefore, the computation becomes less efficient.

Although the EFDM is a very efficient method for solving differential equations on the CM-5, it does have a very stringent stability criterion. As mentioned before in chapter 1, the time step for the ablative problem can be as small as 10^{-6} second. The IFDM has a much less stringent stability criterion than the EFDM. In the 1-D heat conduction example, the IFDM is actually unconditionally stable. However, the implementation of IFDM on the CM-5 is not as efficient as that of EFDM.

For any given problem, it is difficult to predict *a priori* which method is the most suitable. The most efficient algorithm will take advantage of the strengths of both methods while minimizing the weaknesses. The hybrid algorithm is developed based on this concept.

2.4 Parallel Computing Performance Measures

For serial algorithms, performance measurement based on millions of floating point instructions per second (MFLOPS) is usually appropriate. However, applying this type of measurement to a parallel algorithm is not appropriate. The reasons are: (1) extra work is done by a

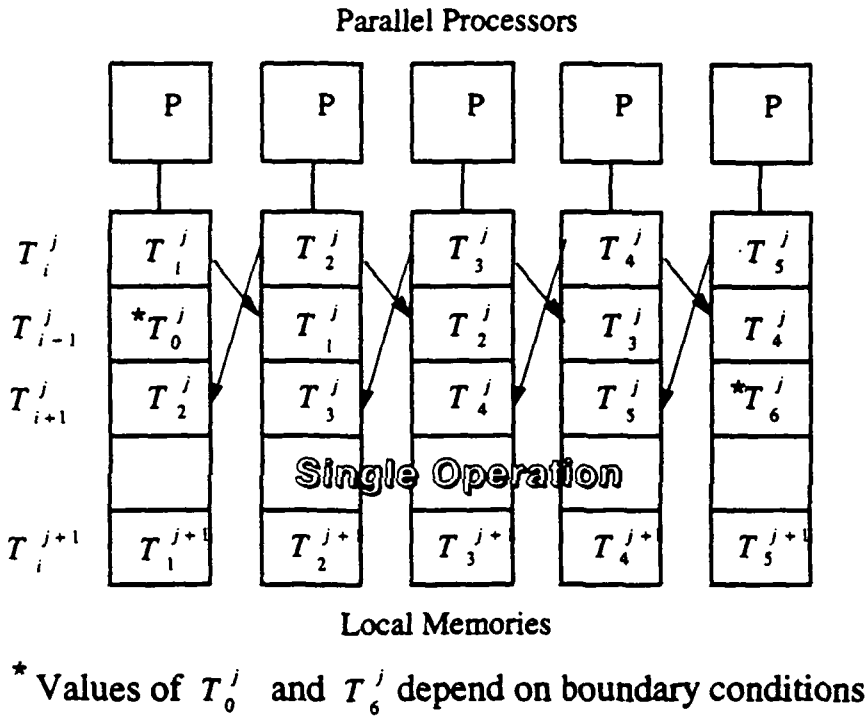

* Values of T_0^j and T_6^j depend on boundary conditions

Figure 2-4. Example computation using parallel processors.

parallel computer in the background and (2) synchronization and communication overhead costs are not reflected in FLOPS. Moreover, it does not give any measure on how effectively the code is parallelized.

The performance of parallel algorithms is most commonly measured in terms of speedup. Speedup of an algorithm executed using N processors is defined as:

$$S = \frac{t_1}{t_N} \tag{2-6}$$

where S is the speedup, t_1 is the execution time using one processor, and t_N is the execution time using N processors.

However, simply measuring the speedup, S, is not sufficient to learn how well a parallel code is written. By applying Amdahl's law [29], one can measure, ideally, how much of an algorithm cannot be parallelized and must be run sequentially. This measure is provided by Amdahl's fraction, α. The idealized t_N can then be written in terms of α and t_1 as:

$$t_N = \alpha t_1 + (1+\alpha)\frac{t_1}{N} \tag{2-7}$$

Substituting Eqn. (2-7) into Eqn. (2-6) and letting N approach infinity, the maximum ideal speedup is obtained:

$$S_{max.ideal} = \lim_{N\to\infty} S = \frac{1}{\alpha} \tag{2-8}$$

The maximum ideal speed up approaches asymptotically to a number governed by α which is the fraction of the sequential algorithm that cannot be parallelized.

It is assumed that the Amdahl's fraction, α, is a constant and depends only on the algorithm. In most engineering problems, α depends not only on the algorithm but also on the problem size. Hence, Amdahl's law is not

directly applicable to measure the performance of an algorithm on CM-5, as overhead costs such as initial setup, opening and closing files, input/output of results, interprocessor communication, and synchronization delays are not taken into account.

To overcome the limitations in Amdahl's law, a measure called the *effective parallelization*, p, has been introduced by E.J. Plaskacz et. al. [30]. In order to compute p, the equivalent Amdahl's fraction, α_e, is calculated first from the measured speedup using Eqns. (2-6) and (2-7):

$$\alpha_e = \frac{\frac{N}{S} - 1}{N - 1} \tag{2-9}$$

Note that α_e represents the fraction of the code that is running serially, and this includes the serial part of an algorithm as well as the overhead costs. The effective parallelization, p, is then given by

$$p = 1 - \alpha_e \tag{2-10}$$

where p represents the fraction of the code that can be completely parallelized.

Efficiency, e, and excess time, t_{ex}, are two additional useful measures of a parallel code's performance. Efficiency is defined by

$$e = \frac{S}{N} \tag{2-11}$$

Excess time measures the time spent by a processor over and above the time required due to ideal speedup and it is given by the following equation:

$$t_{ex} = t_N(1 - e) \tag{2-12}$$

The excess time provides a measure of the total time a parallel computer spends on overhead costs.

CHAPTER 3

PROBLEM STATEMENT

In this work, analytical models and numerical solution schemes are developed to solve three ablation-type problems of interest. The three problems are: (1) transpiration cooling of a uniform plate (2) ablation of a composite plate, and (3) restrained thermal growth of a composite test specimen.

In the transpiration cooling problem, a flat plate made of porous material with gas flowing through the thickness is considered. The in-plane dimensions of the plate are much greater than the through-thickness dimension and all boundary conditions are uniformly applied over the in-plane dimensions of the plate. A one-dimensional analysis in the thickness direction is developed. Given the material and flowing gas properties (assumed constant), the initial conditions (temperature and pressure), and the boundary conditions (temperature and pressure values at both boundaries, tractions at one end, and displacements at the other), temperature, pressure, and stress as functions of time and position through the thickness, and mass flux as a function of time, are obtained. The solution of this problem is used for comparison to exact steady state solutions, and to explore the time scales of different physical aspects of the problem.

In the ablative composite plate problem, a flat plate made of carbon-phenolic material, exposed on one surface to a high temperature environment and insulated on the other, is considered. The in-plane dimensions of the

plate are much greater than the through-thickness dimension and all boundary conditions are uniformly applied over the in-plane dimensions of the plate. A one-dimensional analysis in the thickness direction is developed. Given the material and gas properties, and the initial and boundary conditions, temperature, pressure, and stress as functions of time and position through the thickness, and the maximum pressure as a function of time, are obtained. Initial conditions specified are temperature and pressure, uniformly distributed through the thickness of the plate. Boundary conditions specified on the exposed surface of the plate are the heat flux and ambient pressure values. On the insulated surface, the heat flux and gas mass flux values are set to zero. The solutions of this problem are used to demonstrate the capability of the massively parallel computer algorithm to incorporate complex physics, explore the effects of including additional physics on the solutions, and study the performance of the algorithm.

In the restrained thermal growth (RTG) problem, a cylindrical specimen made of carbon phenolic material heated uniformly at a constant rate and held at a constant longitudinal strain is considered. A one-dimensional model, approximating the cylindrical geometry of the specimen as a strip, is developed. Given the material and gas properties and the initial and boundary conditions, the restraining stress required to hold the specimen at a constant longitudinal strain is obtained as a function of temperature. The properties of the material and gas are functions of temperature and chemical state. The initial conditions are uniformly distributed temperature and pressure values. The boundary conditions at one end of the strip are the values of ambient pressure and surface tractions. At the other end of the strip, the values of the mass flux and displacements are set equal to zero. The solution of the problem is used to demonstrate the capability of the

computer algorithm to incorporate complex physics, to perform a parametric study of two chemical reaction models, and to compare the analytical results to experimental measurements.

CHAPTER 4

THEORY AND IMPLEMENTATION

In this chapter, the general governing equations are developed for three physical problems. Explicit finite difference method (EFDM) or hybrid solution schemes are developed for these problems. The chapter is divided into four main sections: (1) general governing equations, (2) governing equations for transpiration cooling, (3) governing equations for ablative composite plates, and (4) governing equations for restrained thermal growth (RTG) testing. For each case, the general governing equations are simplified appropriately. The implementation of the solution scheme for each of the three problems is also discussed.

4.1 General Governing Equations

The general governing equations used here are based on the model of McManus [12]. The general governing equations are developed based on two models: (1) thermochemical and (2) mechanical models. In the thermochemical model, McManus used a control volume approach to obtain the local mass and energy balance equations. These two equations were used to obtain the internal pressure and temperature distributions inside the control volume. The mechanical model was based on the poroelasticity theory developed by Biot et. al. [19]. This theory takes into account the internal pressure in the calculation of stresses.

The unit control volume of a porous solid used by McManus [12] is shown in Figure 4-1. In general, a porous solid contains both porous virgin and porous charred solids. The volume occupied by the virgin and charred solids are denoted by v_s and v_c, respectively. Initially, the unit control volume consists of porous virgin solid and absorbed moisture only. Due to heating, some of the porous virgin solid is converted to porous charred solid. Gases are then released from the virgin solid into the pores of the virgin and charred solid. Moreover, the gases flow through the walls of the unit control volume. By applying the principles of conservation of mass and energy to the unit control volume, the general 3-D governing equations for pressure and temperature are obtained [12]. Then poroelasticity theory is applied to the unit control volume to obtain the stresses in the porous solid. In this work, only the 1-D form of the general pressure, temperature, and stress governing equations are developed. The reason for this simplification is discussed in the following section.

4.1.1 Geometric Considerations

In the first two cases (transpiration cooling and ablative composite plate), the structure considered is a thin plate depicted in Figure 4-2. The in-plane dimensions are assumed to be much greater than the through-thickness dimension. In addition, the boundary conditions, such as temperature, pressure, and surface tractions, are uniform over the in-plane dimensions. It can then be assumed that all of the derivatives with respect to the in-plane dimensions are zero, hence the temperature, pressure, and stress vary only in the thickness direction. Therefore, only the 1-D governing equations for temperature, pressure, and stress need to be developed. The RTG problem can be simplified to 1-D as well. This is

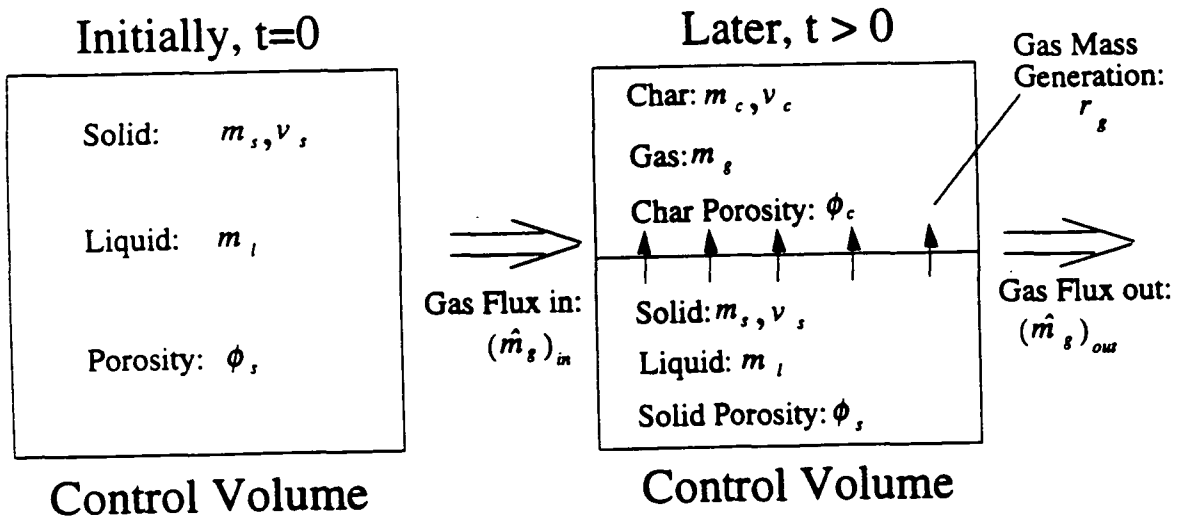

Figure 4-1. Illustration of the unit control volume.

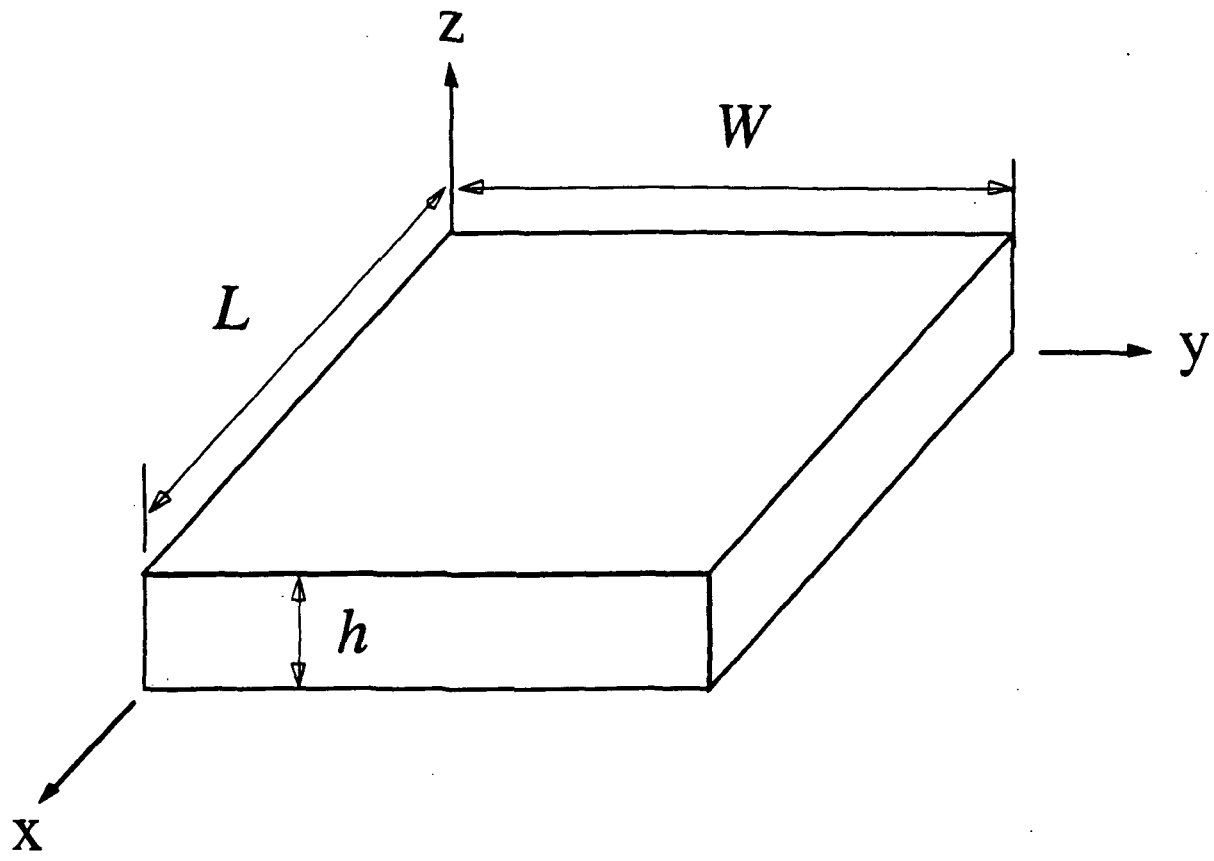

Figure 4-2. Thin plate geometry used in transpiration cooling and ablative composite plate where the length (L) and the width (W) are much greater than the thickness (h).

achieved by considering the variations in temperature, pressure, and stresses along a strip of the material. More details will be discussed in the later sections where the governing equations for the RTG problem are developed.

4.1.2 Mass and Energy Balance Equations

The 1-D gas mass balance (continuity) equation is:

$$\frac{\partial m_g}{\partial t} = -\frac{\partial \hat{m}_g}{\partial z} + r_g \tag{4-1}$$

where m_g is the mass of gas per unit control volume, $\hat{m}_g$ is the mass flux of gas, and r_g is the rate of gas mass generation per unit control volume. The first term of Eqn. 4-1 represents gas mass storage, the second term represents the change of mass due to gas flow, and the last term represents the generation of gas due to chemical reactions.

The velocity of the gas flowing inside the porous solid is assumed to obey Darcy's Law [31]:

$$V_D = -\frac{\gamma}{\mu}\frac{\partial P}{\partial z} \tag{4-2}$$

where V_D is the area-average gas velocity, γ is the permeability of the porous solid, μ is the average viscosity of the gas [32], and P is the internal pressure. Then the mass flux of the gas is:

$$\hat{m}_g = \rho_g V_D \tag{4-3}$$

where ρ_g is the intrinsic density of gas defined as the density of the gas within the pores. The mass of gas per unit control volume is related to its intrinsic density by:

$$m_g = \phi \rho_g \tag{4-4}$$

where ϕ is the porosity of the porous solid.

The gas inside the porous solid is assumed to behave ideally, so the pressure is given by the ideal gas law as:

$$P = \frac{RTm_g}{M\phi} \tag{4-5}$$

where R is the universal gas constant, T is the absolute temperature, and M is the average molecular weight of the gas [32].

The 1-D energy balance equation is:

$$\frac{\partial E}{\partial t} = -\frac{\partial}{\partial z}(q_{cond}) - \frac{\partial}{\partial z}(q_{conv}) + \sum_k E_{gen_k} \tag{4-6}$$

where E is the internal energy inside the control volume, q_{cond} is the heat flux due to conduction, q_{conv} is the heat flux due to convection, and E_{gen_k} is the heat generated by the kth chemical reaction. Equation 4-6 represents the rate of internal energy change inside the control volume due to heat flow by conduction and convection and heat generation by chemical reactions. More specifically, the terms in Eqn. 4-6 are:

$$\begin{aligned} \frac{\partial E}{\partial t} &= \frac{\partial}{\partial t}\sum_i m_i h_i \\ q_{cond} &= -K_z \frac{\partial T}{\partial z} \\ q_{conv} &= h_g \hat{m}_g \\ \sum_k E_{gen_k} &= \sum_k R_k \overline{Q}_k \end{aligned} \tag{4-7}$$

where m_i is the mass per unit control volume of the ith substance, h_i is the enthalpy per unit mass of the ith substance, K_z is the area-average thermal conductivity in the z direction, h_g is the enthalpy per unit mass of the gas, R_k is the rate of reaction of the kth reaction, and $\overline{Q}_k$ is the chemical heat of reaction of the kth reaction. By substituting Eqn. 4-7 into Eqn. 4-6 and applying the ideal gas assumption, the energy equation (Eqn. 4-6) becomes [12]:

$$\left(\sum_i C_{P_i} m_i\right)\frac{\partial T}{\partial t} = \frac{\partial}{\partial z}\left(K_z \frac{\partial T}{\partial z}\right) - C_{P_g}\dot{m}_g \frac{\partial T}{\partial z} + \sum_k R_k \bar{Q}_k - \sum_i r_i h_i \qquad (4\text{-}8)$$

where r_i is the rate of mass generation of the ith substance, C_{P_i} is the specific heat of the ith substance, and C_{P_g} is the specific heat of the gas.

Note that in Eqn. 4-8, the rate of reaction of the kth reaction, R_k, is in general a function of temperature, internal pressure, state of chemical reactions, etc. A reaction rate law is used to predict R_k. The rate of mass generation of the ith substance in Eqn. 4-8, r_i, is given by the sum of contributions from all reactions that produced the ith substance ($r_i = \sum_k r_{ik} R_k$). Finally, the char volume, v_c, is defined in the unit control volume as the ratio of the current mass of charred solid to the mass when all reactions are complete.

Equations 4-1 through 4-8, along with appropriate initial and boundary conditions, and reaction laws (discussed later) provide the necessary relations to obtain the temperature and internal pressure distributions.

4.1.3 Stress Equations

In this section, the summation convention over repeated indices is assumed and comma indicates spatial derivative. The equation of motion for the porous solid without body force is :

$$\rho_s \frac{\partial^2 u_i}{\partial t^2} + c\frac{\partial u_i}{\partial t} = \sigma_{ij,j} \qquad (4\text{-}9)$$

where ρ_s is the density of the porous solid, u_i is the displacement vector of the porous solid in the ith direction, c is the damping coefficient, and σ_{ij} is the total stress tensor. The transient terms on the left hand side of Eqn. 4-9 are due to the inertial and damping effects of the porous solid. The term on the

right hand side of Eqn. 4-9 is associated with the forces developed due to the deformations of the porous solid.

The damping term is introduced in order for the solution of Eqn. 4-9 to reach steady-state. By nondimensionalizing Eqn. 4-9 (see Appendix A.1), a nondimensional damping coefficient is derived [33]:

$$\varsigma = \frac{c}{2\rho_s \omega_n} \tag{4-10}$$

where ς is the nondimensional damping coefficient, and ω_n is the circular natural frequency and is given by $\sqrt{E/(\rho_s h^2)}$. In the transpiration cooling calculation, it will be assumed that the solid response will be underdamped ($\varsigma<1$) and a ς value of 0.1 is used. The value of 0.1 for ς is unrealisticly large. However, in the problems considered the transient effects in stress are not very important, hence a large value of ς is used to damp out the transient effects quickly.

The total stress tensor, σ_{ij}, is defined in reference [12] as:

$$\sigma_{ij} = \sigma_{ij}^m - P\delta_{ij} \tag{4-11}$$

where σ_{ij}^m is the mechanical stress tensor and δ_{ij} is the Kronecker delta. The total stress tensor includes contributions from both the mechanical stresses and internal pressures.

The strain-displacement relation is:

$$\varepsilon_{ij} = \frac{1}{2}\left(u_{i,j} + u_{j,i}\right) \tag{4-12}$$

Strain may be introduced into the porous solid by mechanical stresses, internal pressures, temperature, moisture, and chemical (charring) reactions. Accordingly, the total strain is:

$$\varepsilon_{ij} = S_{ijkl}\sigma_{kl}^m + \Lambda_{ij}\Delta P + \alpha_{ij}\Delta T + \beta_{ij}\Delta(MC) + \chi_{ij}\Delta v_c \tag{4-13}$$

In Eqn. 4-13, α, β, and χ are the temperature, moisture, and charring expansion coefficients, respectively, and ΔP, ΔT, $\Delta(MC)$, and Δv_c are the changes from a reference value of the pressure, temperature, absorbed moisture content, and char volume, respectively. The tensor S_{ijkl} is the compliance of the porous solid under mechanical loading and Λ_{ij} is the compliance of the porous solid when subjected to an internal pressure. The values of these compliance tensors must be determined from experiments.

Once the temperature and internal pressure distributions (Eqns. 4-1 through 4-8) are determined, Eqns. 4-9 through 4-13, together with appropriate initial and boundary conditions, provide a set of relations necessary to obtain the stress distributions inside the porous solid. The specific boundary conditions used for each of the three cases will be discussed in the following sections.

4.2 Transpiration Cooling

To demonstrate the feasibility of using the explicit finite difference method (EFDM) to solve a system of partial differential equations on a CM-5, a sample problem is first solved. The sample problem chosen is the transpiration cooling problem. This problem resembles the ablative composite plate problem with the absence of chemical reactions.

In the transpiration cooling problem, a porous solid, here considered as a plate with a through-thickness temperature gradient, is cooled by sending a gas flow from the cool side to the hot side. This sort of cooling has found applications in the cooling of turbine blades and is under consideration for the surfaces of hypersonic vehicles. The problem is illustrated in Figure 4-3. The pressures and temperatures are fixed at the boundaries. On one end of

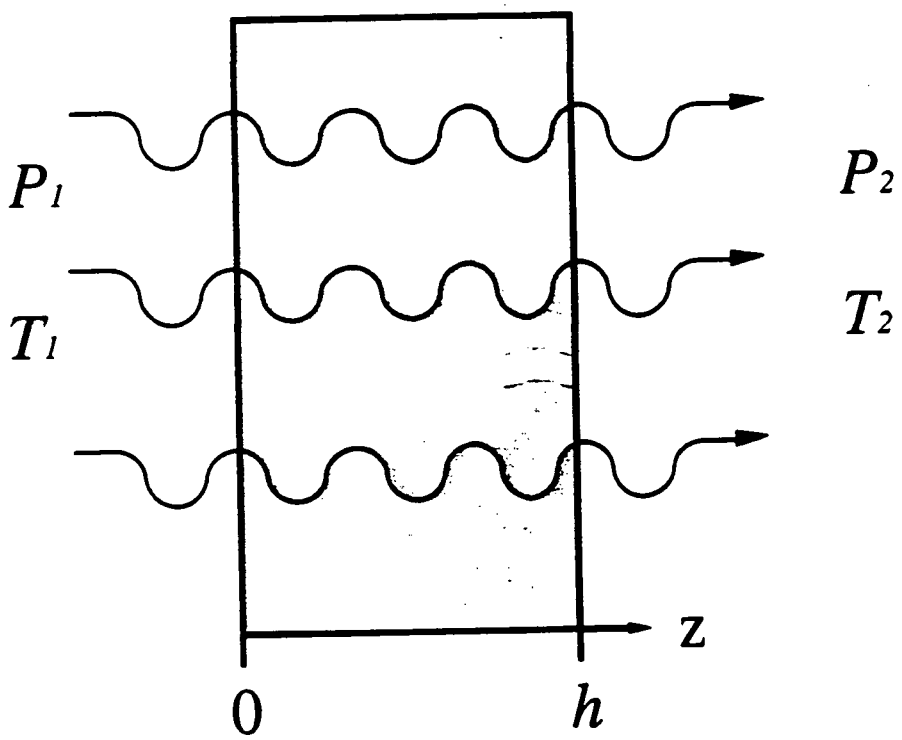

Figure 4-3. Transpiration cooling of a plate of thickness h.

the plate ($z = h$), the value of the mechanical stress is fixed (set to 0). On the other end ($z = 0$), the displacement is fixed (set to 0). It is desired in this problem to find the pressure, temperature, and stress distributions through the thickness of the porous solid matrix. In this problem, all properties associated with both the porous solid and cooling gas are assumed to be constant. Moreover, the porous solid is isotropic and consists of the porous virgin solid only.

4.2.1 Transpiration Cooling Governing Equations

In order to obtain the through-thickness temperature, pressure, and stress distributions, the general 1-D governing equations need to be simplified appropriately for the transpiration cooling problem. Since there are no chemical reactions in the transpiration cooling problem, the gas generation term in the 1-D continuity equation (Eqn. 4-1) is set to zero:

$$\frac{\partial m_g}{\partial t} = -\frac{\partial \hat{m}_g}{\partial z} \tag{4-14}$$

It is assumed that the system consists of two species: an isotropic porous solid and a cooling gas. The two energy generation terms due to chemical reactions in the energy balance equation (Eqn. 4-8) are set to zero. The energy equation (Eqn. 4-8) then simplifies to:

$$\left(C_{P_s} m_s + C_{P_g} m_g\right)\frac{\partial T}{\partial t} = K_z \frac{\partial^2 T}{\partial z^2} - C_{P_g} \hat{m}_g \frac{\partial T}{\partial z} \tag{4-15}$$

where C_{P_s} is the specific heat of the porous solid and m_s is the mass of the porous solid per unit control volume. After some algebraic manipulations (using Eqns. 4-2 through 4-5) Eqns. 4-14 and 4-15 become:

$$\frac{\partial \rho_g}{\partial t} = \frac{\gamma R}{\phi \mu M}\left[T\left(\frac{\partial \rho_g}{\partial z}\right)^2 + 3\rho_g\left(\frac{\partial T}{\partial z}\right)\left(\frac{\partial \rho_g}{\partial z}\right) + \rho_g T\frac{\partial^2 \rho_g}{\partial z^2} + \rho_g^2\frac{\partial^2 T}{\partial z^2}\right]$$

$$\frac{\partial T}{\partial t} = \frac{1}{\left(C_{P_s}(1-\phi)\rho_s + C_{P_g}\phi\rho_g\right)}\left[K_z\frac{\partial^2 T}{\partial z^2} + \frac{C_{P_g}\gamma R}{\mu M}\left(\rho_g T\frac{\partial \rho_g}{\partial z}\frac{\partial T}{\partial z} + \rho_g^2\left(\frac{\partial T}{\partial z}\right)^2\right)\right] \quad (4\text{-}16)$$

The derivation of Eqns. 4-16 is outlined in more details in Appendix A.2. Equations 4-16 are used in the actual computation.

Simplifying the equations of motion to 1-D:

$$\rho_s\frac{\partial^2 u_x}{\partial t^2} + c\frac{\partial u_x}{\partial t} = \sigma_{xx,z}$$

$$\rho_s\frac{\partial^2 u_y}{\partial t^2} + c\frac{\partial u_y}{\partial t} = \sigma_{yx,z} \quad (4\text{-}17)$$

$$\rho_s\frac{\partial^2 u_z}{\partial t^2} + c\frac{\partial u_z}{\partial t} = \sigma_{zx,z}$$

Note that it is assumed in Eqns. 4-17 implicitly that the damping coefficient is the same in all three directions. The equations of motion can be simplified further by making use of Eqns. 4-11 through 4-13. To be consistent with the assumption that the system consists of only the isotropic porous virgin solid and the cooling gas, $\Delta(MC)$ and Δv_c are also set equal to zero in Eqn. 4-13. After some algebraic manipulations, Eqns. 4-17 become:

$$\rho_s\frac{\partial^2 u_x}{\partial t^2} + c\frac{\partial u_x}{\partial t} = Du_{x,zz}$$

$$\rho_s\frac{\partial^2 u_y}{\partial t^2} + c\frac{\partial u_y}{\partial t} = Du_{y,zz} \quad (4\text{-}18)$$

$$\rho_s\frac{\partial^2 u_z}{\partial t^2} + c\frac{\partial u_z}{\partial t} = \frac{1}{A}\left(u_{z,zz} - (A+B)\Delta P_{,z} - C\Delta T_{,z}\right)$$

where

$$A = \frac{2\upsilon^2 + \upsilon - 1}{E(\upsilon - 1)}$$

$$B = -\frac{\Lambda(\upsilon + 1)}{(\upsilon - 1)}$$

$$C = -\frac{\alpha(\upsilon + 1)}{(\upsilon - 1)} \qquad (4\text{-}19)$$

$$D = \frac{E}{2(1 + \upsilon)}$$

E is the Young's modulus of the porous solid, υ is the Poisson's ratio, and the pressure compliance tensor, Λ, is taken from reference [34] for the isotropic and dilute porosity case as:

$$\Lambda = -\frac{1 - 2\upsilon}{E} \qquad (4\text{-}20)$$

The derivation of Eqns. 4-18 are outlined in more detailed in Appendix A.3. Equations 4-16 through 4-20 are incorporated into a computer code on the CM-5 to obtain the through-thickness temperature, pressure, and stress distributions. The computer implementation is discussed in the next section.

4.2.2 CM-5 Implementation - Transpiration Cooling

In order to obtain the through-thickness temperature and pressure distributions, Equations 4-16 are cast into an explicit finite difference form. Forward difference is used for the temporal derivation, backward difference, with respect to the gas flow direction, is applied to all first order spatial derivatives, and central difference is applied to all second order spatial derivatives. The finite difference forms are:

$$\rho_{gi}^{j+1} = \frac{\Delta t \gamma R}{\phi \mu M}\left[T_i^j \left(\frac{\rho_{gi}^j - \rho_{gi-1}^j}{\Delta z} \right)^2 + 3\rho_{gi}^j \left(\frac{T_i^j - T_{i-1}^j}{\Delta z} \right)\left(\frac{\rho_{gi}^j - \rho_{gi-1}^j}{\Delta z} \right) \right.$$
$$\left. + \rho_{gi}^j T_i^j \left(\frac{\rho_{gi+1}^j - 2\rho_{gi}^j + \rho_{gi-1}^j}{\Delta z^2} \right) + \rho_{gi}^{j\,2} \left(\frac{T_{i+1}^j - 2T_i^j + T_{i-1}^j}{\Delta z^2} \right) \right] + \rho_{gi}^j$$

$$T_i^{j+1} = \frac{\Delta t}{\left(C_{P_s}(1-\phi)\rho_s + C_{P_g}\phi\rho_{gi}^j \right)} \left[K_z \left(\frac{T_{i+1}^j - 2T_i^j + T_{i-1}^j}{\Delta z^2} \right) \right. \qquad (4\text{-}21)$$
$$\left. + \frac{C_{P_g}\gamma R}{\mu M} \left(\rho_{gi}^j T_i^j \left(\frac{\rho_{gi}^j - \rho_{gi-1}^j}{\Delta z} \right)\left(\frac{T_i^j - T_{i-1}^j}{\Delta z} \right) + \rho_{gi}^{j\,2} \left(\frac{T_i^j - T_{i-1}^j}{\Delta z} \right)^2 \right) \right] + T_i^j$$

where ρ_{gi}^j is the intrinsic gas density at the ith node and the jth time step, T_i^j is the temperature at the $i$the node and the jth time step, Δz is the distance between two neighboring nodes, and Δt is the time step. These approximation schemes are chosen to ensure stability of the explicit finite difference method [35]. The values of temperature (T) and intrinsic gas density (ρ_g) are obtained by marching forward in time. The values of the internal pressure are calculated using the ideal gas law (Eqn. 4-5) with the known value of T and ρ_g at each time step.

To obtain the through-thickness stress distributions, Eqns. 4-18 are cast into an explicit finite difference form. Central difference is applied to both the temporal and spatial derivatives for stability reasons [35]:

$$u_{xi}^{j+1} = \frac{D}{(1 + c\Delta t/2\rho_s)} \left(\frac{u_{xi+1}^j - 2u_{xi}^j + u_{xi-1}^j}{\Delta z^2} \right) + 2u_{xi}^j + \left(\frac{c\Delta t}{2\rho_s} - 1 \right) u_{xi}^{j-1}$$

$$u_{yi}^{j+1} = \frac{D}{(1 + c\Delta t/2\rho_s)} \left(\frac{u_{yi+1}^j - 2u_{yi}^j + u_{yi-1}^j}{\Delta z^2} \right) + 2u_{yi}^j + \left(\frac{c\Delta t}{2\rho_s} - 1 \right) u_{yi}^{j-1}$$

$$u_{zi}^{j+1} = \frac{1}{(1 + c\Delta t/2\rho_s)A} \left[\left(\frac{u_{zi+1}^j - 2u_{zi}^j + u_{zi-1}^j}{\Delta z^2} \right) - (A + B) \left(\frac{P_{i+1}^j - P_{i-1}^j}{2\Delta z} \right) \right. \qquad (4\text{-}22)$$
$$\left. - C \left(\frac{T_{i+1}^j - T_{i-1}^j}{2\Delta z} \right) \right] + 2u_{zi}^j + \left(\frac{c\Delta t}{2\rho_s} - 1 \right) u_{zi}^{j-1}$$

where $u_{x_i}^j$ is the value of the displacement of the porous solid in the x direction at the ith node and the jth time step, and similarly for $u_{y_i}^j$ and $u_{z_i}^j$. Once the displacements are obtained, the strain-displacement relation (Eqn. 4-12) is used to obtain the strains. By substituting the strain results into the constitutive relations (Eqn. 4-13 with $\Delta(MC)$ and Δv_c set to zero), the through-thickness mechanical stress distributions, σ_z^m, are obtained.

The spatial derivatives are computed simultaneously at all nodes. As discussed before in Chapter 2, this is achieved by declaring multiple conformable arrays for T, ρ_g, and u's in combination with the EOSHIFT command [1] to get arrays that contain the appropriate data elements. By adding and/or subtracting the arrays according to Eqns. 4-21 and 4-22, the finite difference approximation for the spatial derivative are obtained in unison for all nodes. This is repeated for each time step until the values of T, ρ_g, and u's reach steady state. The results are shown and discussed in Chapter 5.

4.3 Ablative Composite Plate

To demonstrate that complex physics can be incorporated into the EFDM easily, the ablative composite plate problem is solved. Two major complexities arise in the ablative composite plate problem that are not encountered in the transpiration cooling problem. The first complexity is that the material properties are no longer constants. In general, they are functions of temperature (T) and char volume (v_c) [12]. The second complexity is that chemical reactions take place in the ablative composite problem. The chemical reaction model used in this study is the two-step reaction model by McManus [12]. These additional complexities are incorporated into the current model.

The geometry of a typical ablative composite plate is shown in Figure 4-4. Composite plies with fibers at an angle θ (usually 45°) are built up at an angle Φ to the heated surface. When the surface of the plate is exposed to high temperatures (e.g. during rocket firing), the heat conducts into the material, causing it to degrade and release gases. These gases create internal pressure which can eventually exceed the cross-ply strength of the composite, resulting in delaminations (ply-lifts) [12].

The boundary conditions are described by referring to Figure 4-4. On one side of the plate ($z = 0$) the displacements are fixed. That side is also insulated and impermeable to heat and mass flux. The other side ($z = h$) is open to ambient environment where the heat flux, pressure, and applied mechanical loads are specified as functions of time. Initial conditions are specified uniformly through the thickness. Geometry, initial conditions, and all of the surface conditions (heat flux, pressure, and applied mechanical load) are uniform in the x and y directions. Hence, the solutions (pressure, temperature, stress) vary only in the z direction.

4.3.1 Governing Equations - Ablative Composite Plate

There two sources from which gases can be generated in this problem: (1) evaporation of absorbed moisture and (2) charring of the porous solid. The gas generation due to the first and second source will be denoted by r_e and r_p, respectively. The 1-D continuity equation (Eqn. 4-1) now becomes:

$$\frac{\partial m_g}{\partial t} = -\frac{\partial \dot{m}_g}{\partial z} + r_e + r_p \qquad (4\text{-}23)$$

Note that the gas generation term in Eqn. 4-1, r_g, is now given by r_e and r_p, which denote rates of gas generation due to evaporation and pyrolysis

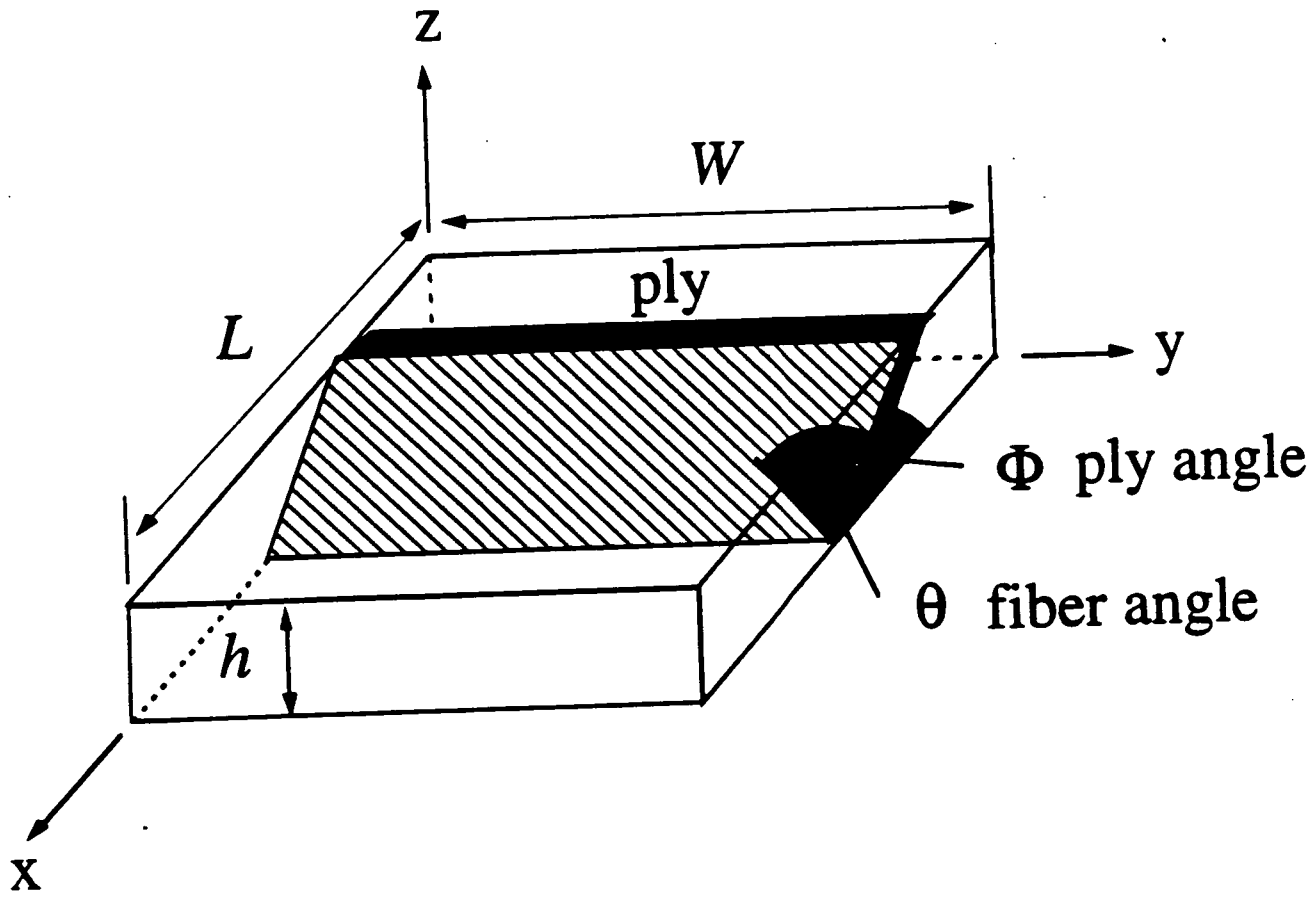

Figure 4-4. Ablative composite plate geometry.

reactions, respectively. Moreover, the terms r_e and r_p are given by the following expressions [12]:

$$\begin{aligned} r_e &= R_w m_s + (MC)\rho_s R_c \\ r_p &= R_w(\rho_s - \rho_c) \end{aligned} \tag{4-24}$$

where R_w is the vapor formation rate, R_c is the char formation rate, ρ_c is the intrinsic density of the charred solid, and MC is the instantaneous moisture content defined as the ratio of the liquid mass over the solid mass. Assuming evaporation and charring reactions are temperature-rate dependent, R_w and R_c are given as [12]:

$$\begin{aligned} R_w &= \frac{1}{T_{ew} - T_{bw}} \frac{\partial T}{\partial t} \quad T_{bw} < T < T_{ew} \quad \text{and} \quad \partial T/\partial t > 0 \\ R_w &= 0 \qquad\qquad T \le T_{bw} \text{ or } T \ge T_{ew} \text{ or } \partial T/\partial t \le 0 \end{aligned} \tag{4-25}$$

and

$$\begin{aligned} R_c &= \frac{1}{T_{ec} - T_{bc}} \frac{\partial T}{\partial t} \quad T_{bc} < T < T_{ec} \quad \text{and} \quad \partial T/\partial t > 0 \\ R_c &= 0 \qquad\qquad T \le T_{bc} \text{ or } T \ge T_{ec} \text{ or } \partial T/\partial t \le 0 \end{aligned} \tag{4-26}$$

where T_{bw} is the temperature at which the evaporation begins, T_{ew} is the temperature at which the evaporation ends, T_{bc} is the temperature at which charring begins, and T_{ec} is the temperature at which charring ends. Note that T_{bw}, T_{ew}, T_{bc}, and T_{ec} are functions of pressure. By applying Darcy's law (Eqn. 4-2) and the ideal gas law (Eqn. 4-5), the 1-D continuity equation (Eqn. 4-23) becomes:

$$\begin{aligned} \frac{\partial P}{\partial t} = {} & \frac{T}{\phi}\frac{\partial}{\partial z}\left(\frac{\gamma}{T\mu}\right)P\frac{\partial P}{\partial z} + \frac{\gamma}{\phi\mu}\frac{\partial P}{\partial z}\frac{\partial P}{\partial z} + \frac{P\gamma}{\phi\mu}\frac{\partial^2 P}{\partial z^2} + \frac{RT}{\phi M}(r_p + r_e) \\ & + \frac{P}{T}\frac{\partial T}{\partial t} - \frac{P}{\phi}\frac{\partial \phi}{\partial t} \end{aligned} \tag{4-27}$$

Eqn. 4-27 is used to obtain the internal pressure distribution. The detailed derivation of Eqn. 4-27 is outlined in Appendix B.1.

The ablative composite plate is a system containing four components: (1) porous virgin solid, (2) porous charred solid, (3) absorbed moisture, and (4) flowing gases due to evaporation and charring. The sum of the internal energies of these four components contribute to the total internal energy of the system. Specifying the energy equation (Eqn. 4-8) to this case:

$$\frac{\partial T}{\partial t} = \frac{1}{\eta}\left[\frac{C_{P_g} m_g \gamma}{\phi \mu}\frac{\partial P}{\partial z}\frac{\partial T}{\partial z} + \frac{\partial K_z}{\partial z}\frac{\partial T}{\partial z} + K_z\frac{\partial^2 T}{\partial z^2} + R_c Q_c + R_w Q_w\right] \tag{4-28}$$

where Q_c and Q_w are the effective heat of charring (pyrolysis) reaction and evaporation reaction, respectively. They are given as [12, 22]:

$$\begin{aligned} Q_c &= \left(\overline{Q}_c + \rho_s h_s - \rho_c h_c - (MC)\rho_s h_e + (MC)\rho_s h_l - (\rho_s - \rho_c)h_p\right) \\ Q_w &= \left(\overline{Q}_w - m_s h_e + m_s h_l\right) \end{aligned} \tag{4-29}$$

where $\overline{Q}_c$ is the heat of charring reaction, $\overline{Q}_w$ is the heat of evaporation reaction, h_s is the specific enthalpy of the virgin solid, h_c is the specific enthalpy of the charred solid, h_p is the specific enthalpy of the pyrolysis gas, h_l is the specific enthalpy of the absorbed moisture, and h_e is the specific enthalpy of the evaporation gas. The combined heat capacity of the system, η, is given as:

$$\eta = C_{P_s} m_s + C_{P_c} m_c + C_{P_l} m_l + C_{P_g} m_g \tag{4-30}$$

where C_{P_s} is the specific heat of the virgin solid, C_{P_c} is the specific heat of the charred solid, C_{P_l} is the specific heat of the absorbed moisture, C_{P_g} is the specific heat of the flowing gases, m_s is the porous virgin solid mass per unit control volume, m_c is the porous charred solid mass per unit control volume, m_l is the absorbed moisture mass per unit control volume, and m_g is the flowing gases mass per unit control volume. Eqn. 4-28 is used to obtain the

through-thickness temperature distributions of the plate. The derivation of Eqn. 4-28 is described in detail in Appendix B.2.

To obtain the through-thickness stress distributions, it will be shown that the time scale associated with the solid deformations is much smaller than the time scales associated with the temperature and pressure responses. Therefore, the response of the solid matrix is approximately steady-state on the time scales of the temperature and pressure responses. This is justified by the results of the transpiration cooling problem and will be discussed further in Chapter 5.

The development here for the stress governing equations is based on the work by McManus [12]. The equations of motion for the solid matrix in steady-state condition (Eqn. 4-9) become:

$$\sigma_{ij,j} = 0 \tag{4-31}$$

which are just the equilibrium equations. As discussed before in section 4.1, the problem allows the simplification to 1-D. With this simplification, Eqn. 4-31 becomes:

$$\sigma_{iz,z} = 0 \tag{4-32}$$

By substituting the definition of the total stress tensor (Eqn. 4-11) into Eqn. 4-32, the following relations are obtained:

$$\begin{aligned} \sigma^m_{xz,z} &= 0 \\ \sigma^m_{yz,z} &= 0 \\ \sigma^m_{zz,z} - P_{,z} &= 0 \end{aligned} \tag{4-33}$$

For the ablative composite plate problem, the boundary condition at the fixed surface ($z = 0$ in Figure 4-3) is:

$$u_i = 0 \tag{4-34}$$

At the free surface ($z = h$ in Figure 4-3), the boundary condition is:

$$\begin{aligned} \sigma_{iz}^{m} &= T_i^b \\ P &= P_b \end{aligned} \tag{4-35}$$

where T_i^b is the mechanically applied traction on the free surface in the ith direction and P_b is just the ambient pressure. The results, after integrating Eqn. 4-33 through the thickness (in the z direction) and applying the surface boundary conditions (Eqn. 4-35), are:

$$\begin{aligned} \sigma_{xz}^{m} &= T_1^b \\ \sigma_{yz}^{m} &= T_2^b \\ \sigma_{zz}^{m} &= T_3^b + \left(P - P_b\right) \end{aligned} \tag{4-36}$$

The strain-displacement relations for the present problem are:

$$\begin{aligned} \varepsilon_{xx} &= \varepsilon_{yy} = \varepsilon_{xy} = 0 \\ \varepsilon_{zz} &= u_{z,z} \\ \varepsilon_{xz} &= \frac{1}{2} u_{x,z} \\ \varepsilon_{yz} &= \frac{1}{2} u_{y,z} \end{aligned} \tag{4-37}$$

Substituting the strain-displacement relations (Eqn. 4-37) into the constitutive equations (Eqn. 4-13) yields:

$$\begin{aligned} 0 &= S_{xxkl}\sigma_{kl}^{m} + \Lambda_{xx}\Delta P + \alpha_{xx}\Delta T + \beta_{xx}\Delta(MC) + \chi_{xx}\Delta v_c \\ 0 &= S_{yykl}\sigma_{kl}^{m} + \Lambda_{yy}\Delta P + \alpha_{yy}\Delta T + \beta_{yy}\Delta(MC) + \chi_{yy}\Delta v_c \\ \frac{\partial u_x}{\partial z} &= S_{xzkl}\sigma_{kl}^{m} + \Lambda_{xz}\Delta P + \alpha_{xz}\Delta T + \beta_{xz}\Delta(MC) + \chi_{xz}\Delta v_c \\ \frac{\partial u_y}{\partial z} &= S_{yzkl}\sigma_{kl}^{m} + \Lambda_{yz}\Delta P + \alpha_{yz}\Delta T + \beta_{yz}\Delta(MC) + \chi_{yz}\Delta v_c \\ \frac{\partial u_z}{\partial z} &= S_{zzkl}\sigma_{kl}^{m} + \Lambda_{zz}\Delta P + \alpha_{zz}\Delta T + \beta_{zz}\Delta(MC) + \chi_{zz}\Delta v_c \\ 0 &= S_{xykl}\sigma_{kl}^{m} + \Lambda_{xy}\Delta P + \alpha_{xy}\Delta T + \beta_{xy}\Delta(MC) + \chi_{xy}\Delta v_c \end{aligned} \tag{4-38}$$

Equations 4-38 are a set of six equations in the six unknowns, the three displacements u_x, u_y, and u_z, and the three stresses σ_{xx}^{m}, σ_{yy}^{m}, and σ_{xy}^{m}.

The other three stresses are given by Eqn. 4-36. Equations 4-38 are solved with the boundary conditions specified in Eqns. 4-34.

4.3.2 CM-5 Implementation - Hybrid Algorithm

In this section the numerical method used to solve the governing equations for pressure and temperature (Eqns. 4-27 and 4-28) is discussed. Due to the stringent stability criterion of the explicit finite difference method (EFDM), the critical time scale for stability needs to be identified. A method for identifying the time scale is proposed. Based on this method, the time scales associated with the temperature and pressure governing equations are identified. From these time scales, the most critical one for stability is determined numerically. A time step is then chosen for the calculation. The basic idea of the hybrid algorithm is that implicit finite difference method (IFDM) is applied for the regions where the time step is greater than the critical time scale, and EFDM is used in the regions where the time step is smaller than the critical time scale. How the critical time scale for the ablative composite problem is identified is discussed in the following paragraphs.

To identify the time scales, the following two generic equations are considered:

$$\frac{\partial u}{\partial t} = -v\frac{\partial u}{\partial x}$$
$$\frac{\partial u}{\partial t} = c\frac{\partial^2 u}{\partial x^2} \qquad (4\text{-}39)$$

where u is some scalar quantity, and v and c are constants. Critical time scales associated with Eqns. 4-39 are [6]:

$$t_{c1} = \frac{l_r}{|v|}$$
$$t_{c2} = \frac{l_r^2}{|c|} \qquad (4\text{-}40)$$

where t_{c1} is the critical time scale for the first equation of Eqns. 4-39, t_{c2} is the critical time scale for the second equation of Eqns. 4-39, and l_r is some reference length such as the spacing between nodes.

By comparing the first three terms on the right hand side of the pressure governing equation (Eqn. 4-27) to Eqns. 4-39, three time scales are identified by comparison to Eqns. 4-40:

$$t_{pc1} = \frac{l_r}{\left| \frac{T}{\phi} \frac{\partial}{\partial z} \left(\frac{\gamma}{T\mu} \right) P \right|}$$
$$t_{pc2} = \frac{l_r}{\left| \frac{\gamma}{\phi\mu} \frac{\partial P}{\partial z} \right|} \qquad (4\text{-}41)$$
$$t_{pc3} = \frac{l_r^2}{\left| \frac{P\gamma}{\phi\mu} \right|}$$

In Eqns. 4-41, t_{pc1}, t_{pc2}, and t_{pc3} are the time scales associated with the governing equation for pressure. The first two equations in Eqns. 4-41 are found by comparing the first two terms on the right hand side in the governing equation for pressure (Eqn. 4-27) to the first equation in Eqns. 4-40. The third equation in Eqns. 4-41 is found by comparing the third term on the right hand side of Eqn. 4-27 to the second equation in Eqns. 4-40. The time scales associated with the governing equation for temperature (Eqn. 4-28) are determined in a similar way:

$$t_{Tc1} = \frac{l_r}{\left| \frac{C_{P_i} m_g \gamma}{\phi \mu \eta} \frac{\partial P}{\partial z} \right|}$$

$$t_{Tc2} = \frac{l_r}{\left| \frac{1}{\eta} \frac{\partial K_z}{\partial z} \right|} \qquad (4\text{-}42)$$

$$t_{Tc3} = \frac{l_r^2}{\left| \frac{K_z}{\eta} \right|}$$

The pressure and temperature governing equations (Eqn. 4-27 and Eqn. 4-28) are first solved using the EFDM. The explicit finite difference form of the pressure governing equation used in computation is:

$$P_i^{j+1} = P_i^j + \frac{\Delta t}{(\phi M/RT)_i^j} \left\{ \left(\frac{m_g \gamma}{\phi \mu} \right)_i^j \left(\frac{P_{i+1}^j - 2P_i^j + P_{i-1}^j}{\Delta z^2} \right) \right.$$
$$+ \left[\left(\frac{m_g \gamma}{\phi \mu} \right)_i^j - \left(\frac{m_g \gamma}{\phi \mu} \right)_{i-1}^j \right] \frac{(P_{i+1}^j - P_i^j)}{\Delta z^2} + \left(\frac{P \phi M}{RT^2} \right)_i^j \left(\frac{\partial T}{\partial t} \right)_i^j \qquad (4\text{-}43)$$
$$\left. - \left(\frac{PM}{RT} \right)_i^j \left(\frac{\partial \phi}{\partial t} \right)_i^j + r_{pi}^j + r_{ei}^j \right\}$$

Equation 4-43 is determined using forward difference for time, backward difference, with respect to the gas flow direction, for the spatial gradients of the coefficients, forward difference, with respect to the gas flow direction, for the pressure gradient, and central difference for the second spatial derivative of pressure. This scheme was chosen to maintain stability and accuracy [26, 36]. The explicit finite difference form of the temperature governing equation used in computation is:

$$T_i^{j+1} = T_i^j + \frac{\Delta t}{\eta_i^j} \left[\left(\frac{K_{zi}^j - K_{zi-1}^j}{\Delta z} \right) \left(\frac{T_{i+1}^j - T_j^i}{\Delta z} \right) + K_{zi}^j \left(\frac{T_{i+1}^j - 2T_i^j + T_{i-1}^j}{\Delta z^2} \right) \right.$$
$$\left. + \left(\frac{C_{P_i} m_g \gamma}{\phi \mu} \right)_i^j \left(\frac{P_{i+1}^j - P_i^j}{\Delta z} \right) \left(\frac{T_{i+1}^j - T_i^j}{\Delta z} \right) + (R_c Q_c)_i^j + (R_w Q_w)_i^j \right] \qquad (4\text{-}44)$$

Equation 4-44 is determined by forward difference for time, backward difference, with respect to the gas flow direction, for the spatial gradients of the coefficients, forward difference, with respect to the gas flow direction, for the spatial gradients of temperature and pressure, and central difference for the second spatial derivative of temperature. Again, the scheme is chosen for stability reason [26, 36].

In the computation of pressure and temperature (Eqns. 4-43 and 4-44), the gas mass, m_g, is determined from the ideal gas law (Eqn. 4-5). The pressures and temperatures are determined by Eqns. 4-43 and 4-44. The six time scales associated with the problem are calculated as well. In the computation of the time scales, the reference length, l_r, is set equal to the spacing between the nodes, Δz. From the six identified time scales (Eqns. 4-41 and. 4-42), it is found in practice that the third equation in Eqn. 4-41 gives the smallest time scale [37]. Therefore, pressure response controls the critical time scale. This implies that for stability reasons in the EFDM, the time step taken in Eqn. 4-43 has to be smaller than the smallest value of the critical time scale.

In Figure 4-5, a semi-log plot of the critical time scale vs. position is plotted along with the representative time scales associated with heat conduction ($t_{cond} = \Delta z^2/2K_z/\eta$) and porous solid deformation ($t_{solid} = \Delta z/2\sqrt{E/\rho_s}$). This plot is generated by solving Eqns. 4-43 and 4-44 using from an EFDM solution at a simulation time of 10 seconds. The solution was for a 3cm thick plate, finely meshed with 251 nodes. The problem solved is more completely described in section 5.2. Note that the abrupt changes in the critical time scale curve are not numerical artifacts. These abrupt changes denote the boundaries of different regions of material response. It can be seen from Figure 4-5 that the smallest value of the critical time scale occurs on the

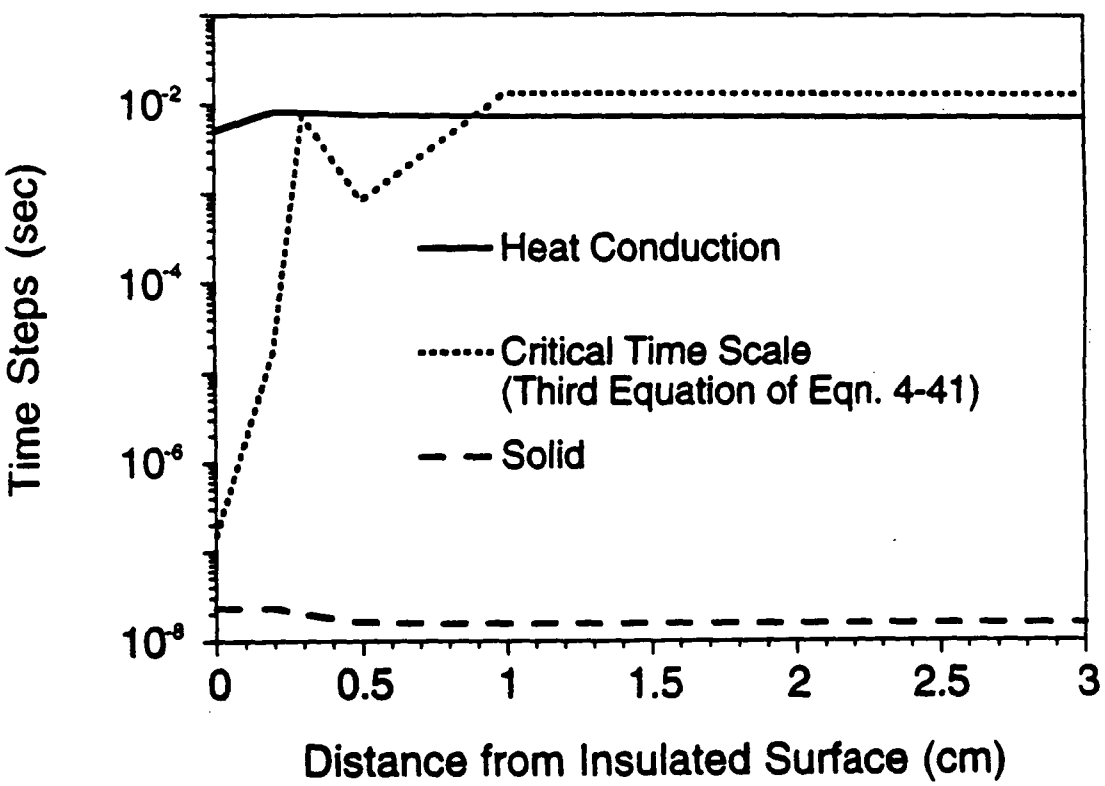

Figure 4-5. Semi-log plot of the conduction time scale, the porous solid time scale, and the critical time scale vs. thickness of the ablative composite plate.

surface and is almost of the same order of magnitude as the time scale associated with solid deformation. However, near the insulated end, the critical time scale is on the same order of magnitude as the one associated with heat conduction. The reason for this large variation is due to the through-thickness variation in permeability. Permeability varies by a factor on the order of 10^6 from the exposed surface to the insulated end. Depending on the degree of permeability, the ablative composite plate can be divided into three regions of material response in the thickness direction: (1) char region, (2) reaction region, and (3) virgin region. This is illustrated in Figure 4-6. This can also be seen from Figure 4-5; the char region extends from about 0 cm to 0.4 cm, the reaction region extends from about 0.4 cm to about 1.0 cm, and the virgin region extends from about 1.0 cm to 3.0 cm.

If the explicit finite difference equations for pressure and temperature (Eqns. 4-43 and 4-44) are applied to all three regions, the time step is governed by the extent of the char region. Typically, the char region is not a critical region where accurate information on pressure and temperature is desired [12]. Therefore, to remove the stringent stability criterion, Eqns. 4-43 and 4-44 are only applied to the reaction and virgin regions (Figure 4-6).

In the char region, it is also assumed that the gas storage term can be neglected [12]. The pressure distribution is then determined from a finite difference formulation of Darcy's law [12]:

$$\hat{m}_{gi}^{j} = -\frac{1}{2\Delta z}\left[\left(\frac{m_g \gamma}{\phi \mu}\right)_i^j + \left(\frac{m_g \gamma}{\phi \mu}\right)_{i+1}^j\right]\left(P_{i+1}^j - P_i^j\right) \qquad (4\text{-}45)$$

The ideal gas law (Eqn. 4-5) is used to determine m_g, and the result is:

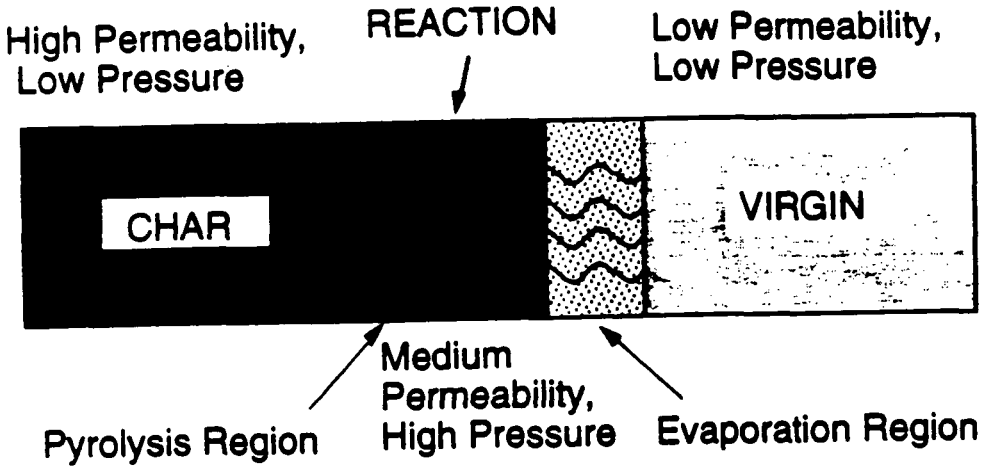

Figure 4-6. Three regions of an ablative composite plate: (1) char regions, (2) reactions region, and (3) virgin region. The reaction region is comprised of two sub-regions: (A) evaporation region and (B) pyrolysis region.

$$\hat{m}_g^i = -\frac{(P_i^j)(P_{i-1}^j)}{2\Delta z}\left[\left(\frac{M\gamma}{RT\mu}\right)_i^j - \left(\frac{M\gamma}{RT\mu}\right)_{i+1}^j\right] + \frac{(P_i^j)^2}{2\Delta z}\left(\frac{M\gamma}{RT\mu}\right)_i^j - \frac{(P_{i-1}^j)^2}{2\Delta z}\left(\frac{M\gamma}{RT\mu}\right)_{i+1}^j \quad (4\text{-}46)$$

Equation 4-46 results in a quadratic equation for the unknown pressure value at the ith node. It can be solved progressively from the node closest to the surface to the last node in the char region once the mass flux of gas is known. The gas mass flux ($\hat{m}_g$) can be calculated by assuming that all gas mass generated in this zone flows to the surface immediately. To calculate $\hat{m}_g$, the gas storage term on the left hand side of the continuity equation (Eqn. 4-23) is set to zero. The continuity equation (Eqn. 4-23) is then integrated numerically over the thickness of the char region.

The energy equation used in the char region is:

$$\frac{\partial T}{\partial t} = \frac{1}{\eta}\left[\frac{\partial}{\partial z}\left(K_z\frac{\partial T}{\partial z}\right) - C_{P_g}\hat{m}_g\frac{\partial T}{\partial z} + R_c Q_c + R_w Q_w\right] \quad (4\text{-}47)$$

Note that the energy equation shown in Eqn. 4-47 is in a different form from the one used in the reaction and virgin regions (Eqn. 4-28). The reason is that $\hat{m}_g$ is obtained in the char region by integrating the continuity equation (Eqn. 4-23). In the other two regions, $\hat{m}_g$ is given by the Darcy's law (Eqn. 4-2). To obtain the explicit finite difference form of Eqn. 4-47 the same scheme used to obtain Eqn. 4-44 is also used on Eqn. 4-47:

$$T_i^{j+1} = T_i^j + \frac{\Delta t}{\eta_i^j}\left[\left(\frac{K_{zi}^j - K_{zi-1}^j}{\Delta z}\right)\left(\frac{T_{i+1}^j - T_i^j}{\Delta z}\right) + K_{zi}^j\left(\frac{T_{i+1}^j - 2T_i^j + T_{i-1}^j}{\Delta z^2}\right) - \left(C_{P_g}\hat{m}_g\right)_i^j\left(\frac{T_{i+1}^j - T_i^j}{\Delta z}\right) + \left(R_c Q_c\right)_i^j + \left(R_w Q_w\right)_i^j\right] \quad (4\text{-}48)$$

Note that in Eqn. 4-48, $\hat{m}_g$ is already known from the numerical integration of the steady-state (gas mass storage term is zero) continuity equation (Eqn. 4-23).

There is no time scale associated with the pressure calculation in the char region (Eqn. 4-46), so stability is no longer a concern. That is not the case for the temperature calculation, since there are still time scales associated with the energy equation (Eqn. 4-47). It has been identified numerically that the most critical time scale associated with the energy equation (Eqn. 4-47) is [37]:

$$t_{Tc} = \frac{\Delta z}{\frac{C_{P_g} \hat{m}_g}{\eta}} \tag{4-49}$$

This time scale is associated with the heat convection process. Its magnitude is high enough to allow the time steps used in Eqns. 4-43 and 4-44 to be used in Eqn. 4-48 as well. A flow-chart of the overall algorithm is shown in Figure 4-7.

The stress distributions are obtained by solving the system of equations in Eqns. 4-38. A standard LU decomposition scheme is adopted to solve the system of equations. Since Eqns. 4-38 are derived based on the assumption that the response of the porous solid reaches steady-state immediately, there is no time scale associated with the problem, i.e. no stability problem. As mentioned before, the steady-state assumption is justified by the results from the transpiration problem which are shown in Chapter 5. Also, as shown in Figure 4-5, the time scale associated with the porous solid response is quite small (about 10^{-6} second). The time scales of the other aspects of the ablative composite plate problem are typically on the

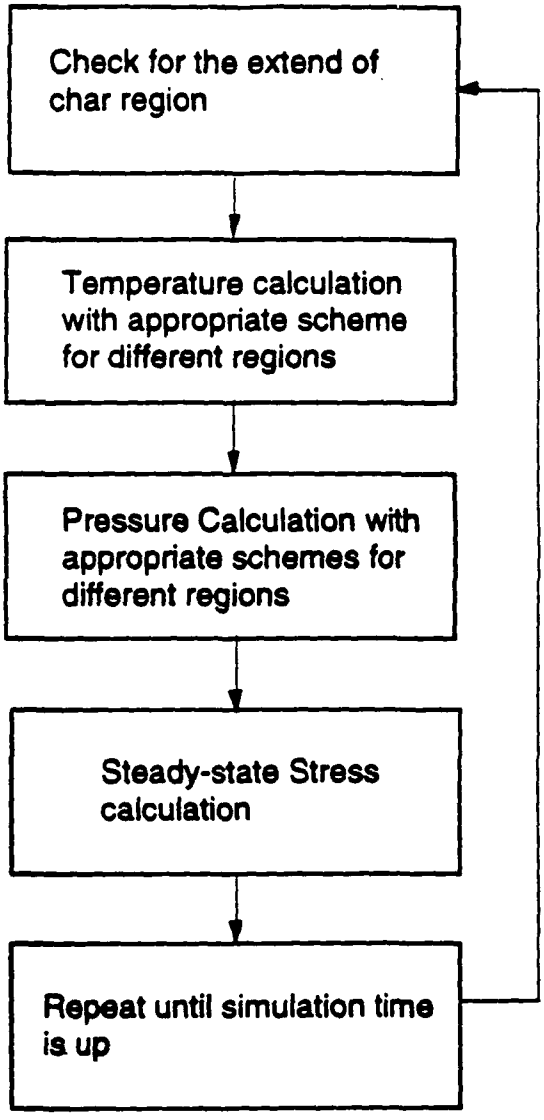

Figure 4-7. Flow chart of the overall algorithm.

order of 10^{-3} second. Therefore, it is quite reasonable to assume the porous solid response reaches steady state immediately.

4.4. Restrained Thermal Growth

Restrained thermal growth (RTG) experiments were performed by Stokes [5] and Hubbert [6] on carbon phenolic specimens preconditioned to three different mixture contents: wet (8.0% water by weight), as-received (3.6% water by weight) and dry (0.27% water by weight). The specimens were cylindrical (0.5 in. diameter and 1.0 in. long). These specimens were heated uniformly at a constant rate of temperature change. The stress required to hold the specimen at a constant longitudinal strain was recorded (Figure 4-8). The specimens were fabricated so that the plane of the carbon fabric was perpendicular to the longitudinal axis of the specimen.

Figure 4-9 is a plot of the restraining stress vs. temperature as measured by Stokes [5]. Sullivan et. al. [38] divided the specimen response in Figure 4-9 into three temperature regions: the thermoelastic, transition, and poroelastic regions. The temperature in the thermoelastic region ranges from room temperature (297 K) to approximately 450 K. In this region, the measured stress is a result of elastic thermal expansion. At some temperature, usually above the cure temperature, secondary hydrogen bonds break down and the materials softens. The region above this temperature, roughly between 450 K to approximately 600 K for carbon-phenolic materials, has been identified as the transition region. Two things happen in this region: (1) the measured stress decreases considerably due to material softening and (2) the specimen begins to undergo pyrolysis and gases begins to accumulate in the specimen. The poroelastic region is at temperatures above 600K. In the poroelastic region the internal pressure becomes large

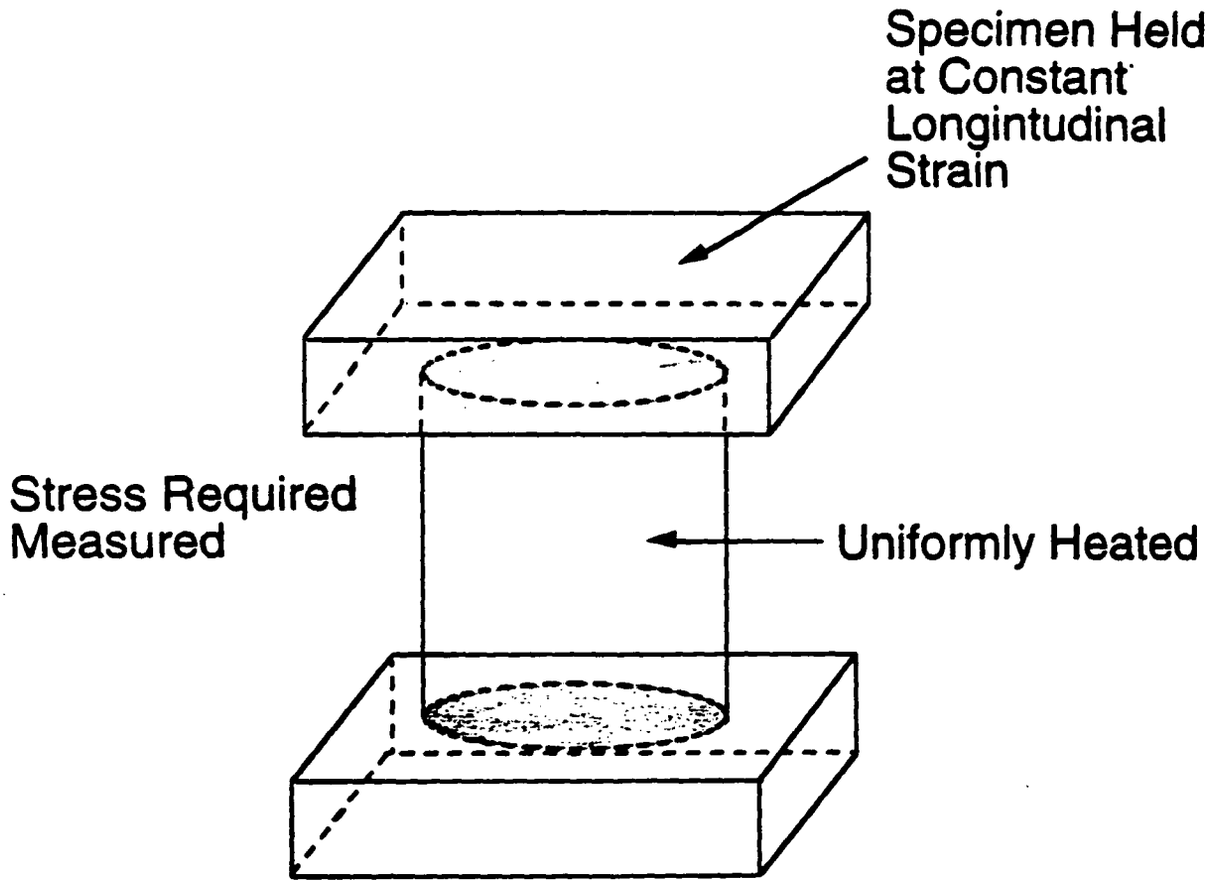

Figure 4-8. Schematic drawing of an experimental setup for RTG testing.

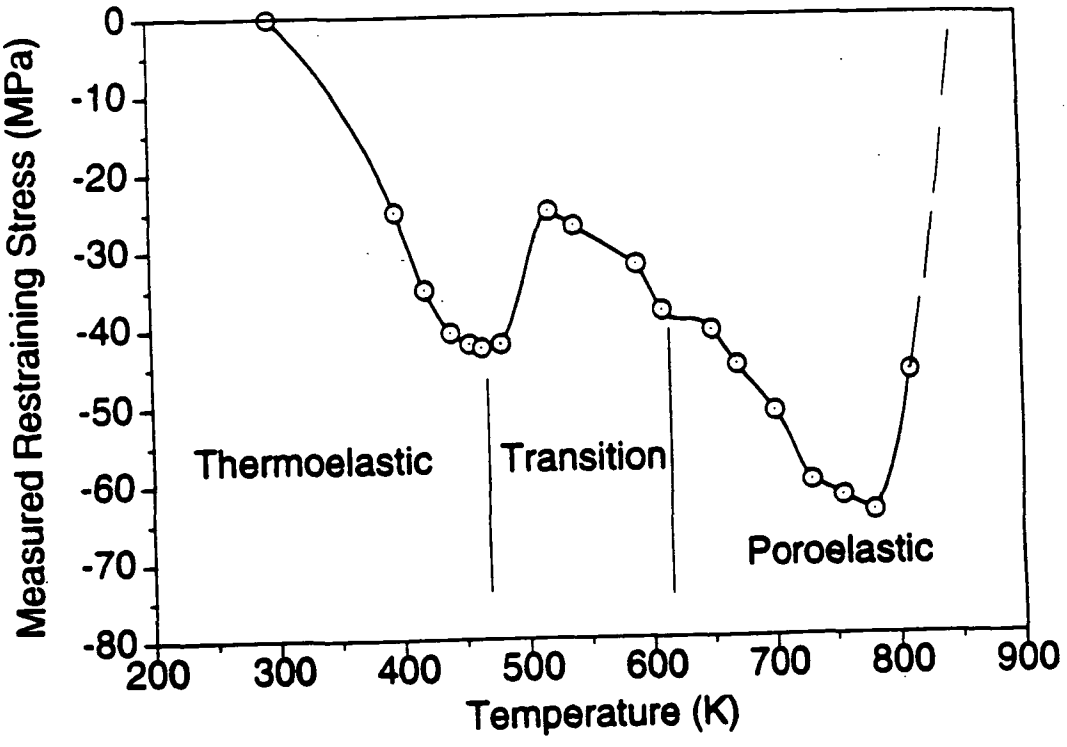

Figure 4-9. Experimental results of RTG testing [5].

and the specimen response is governed by the internal pressure and the material's poroelastic response.

Since the specimens were heated uniformly during the RTG tests, the specimen response does not change along the specimen length. Therefore, the RTG specimen response may be simulated by considering only a cross-sectional slice of the cylindrical test specimens. In reference [38], the longitudinal stress needed to keep the displacement constant was calculated by a finite element method using three-noded, constant-strain, triangular finite elements. Since the specimen response in the RTG test is axisymmetric about the specimen centerline, only one-quarter of the specimen was modeled. The finite element mesh used is shown Figure 4-10. In reference [38], the specimen response is simulated using a 2-D code. In this work, due to the limitations of the current code, a 1-D approximation of the specimen response is used. Referring to Figure 4-10, the 1-D code will be applied along the strip at $y=0$. The current 1-D code cannot be used for quantitative comparison since it is not cast in polar coordinates. However, it can be used to perform parametric studies where only qualitative comparison is necessary. In this study, the effects of pressure-independent and pressure-dependent Arrhenius type chemical reaction rate equations are compared to experimental data.

The pressure distribution along the strip is approximated by using the same governing equation for pressure calculation as in the ablative composite plate case. The only difference in this case is that the z-direction is now replaced by the x-direction. The energy equation is not needed because the heating rate, $\partial T/\partial t$, is specified in the RTG tests. Only stress governing equations are needed.

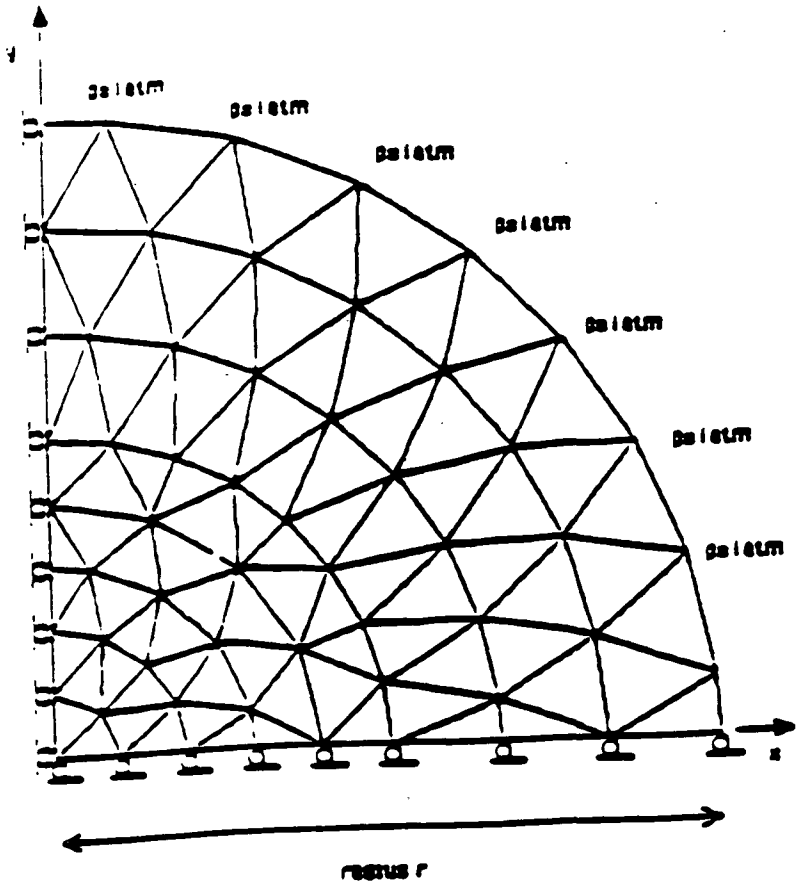

Figure 4-10. Finite element mesh used for RTG analysis [38]. Radius is 0.635cm.

4.4.1 Governing Equations for RTG - Stresses

In the RTG test, the longitudinal displacement was held fixed. Therefore, the specimen can be modeled closely by the plane-strain assumption. Under the plane-strain assumption, ε_{xx}, ε_{yz} and ε_{xz} are zero. With these three strains being zero, the strain-displacement relations (Eqn. 4-12) become:

$$\begin{aligned} \varepsilon_{xx} &= u_{x,x} \\ \varepsilon_{xy} &= \frac{1}{2}\left(u_{x,y} + u_{y,x}\right) \\ \varepsilon_{yy} &= u_{y,y} \end{aligned} \tag{4-50}$$

In reference [38], the material of the RTG specimen is assumed to be transversely isotropic with the plane of isotropy (x-y plane) coincident with that of the carbon cloth (Figure 4-10). Directly from the constitutive equations for transversely isotropic material under the plane-strain assumption [39] , the transverse shear stresses σ_{xz} and σ_{yz} are zero. Note that there is no y variation along the strip in the x-direction ($\partial/\partial y = 0$). Also, referring to Figure 4-10, the displacement u_y is zero along the strip. With these two simplifications, the strain-displacement relations (Eqn. 4-50) become:

$$\begin{aligned} \varepsilon_{xx} &= u_{x,x} \\ \varepsilon_{xy} &= 0 \\ \varepsilon_{yy} &= 0 \end{aligned} \tag{4-51}$$

Applying the constitutive equations again [39], σ_{xy} can be shown to be zero. The equilibrium equation in this case is:

$$\sigma_{xx,x} = 0 \tag{4-52}$$

Integrating the equilibrium equation over the length of the strip and applying the definition of total stress tensor (Eqn. 4-11) and the traction free boundary condition at $x=r$, an expression for σ_{xx} is obtained:

$$\sigma_{xx}^{m} = (P - P_b) \tag{4-53}$$

The following two equations are used to solve for u_x and σ_{yy}^{m}:

$$\begin{aligned} u_{x,x} &= S_{xxxx}\sigma_{xx}^{m} + S_{xxyy}\sigma_{yy}^{m} + \Lambda_{xx}\Delta P + \alpha_{xx}\Delta T + \beta_{xx}\Delta(MC) + \chi_{xx}\Delta v_c \\ 0 &= S_{yyxx}\sigma_{xx}^{m} + S_{yyyy}\sigma_{yy}^{m} + \Lambda_{yy}\Delta P + \alpha_{yy}\Delta T + \beta_{yy}\Delta(MC) + \chi_{yy}\Delta v_c \end{aligned} \tag{4-54}$$

along with the boundary condition:

$$u_x = 0 \qquad x = 0 \tag{4-55}$$

Eqn. 4-54 is derived by specializing the constitutive equations in Eqn. 4-13 to the RTG problem. With σ_{xx}^{m}, σ_{xy}^{m}, and σ_{yy}^{m} known, the restraining stress, σ_{zz}^{m}, can be calculated with the following equation derived from Eqn. 4-13:

$$\sigma_{zz}^{m} = -\frac{1}{S_{zzzz}}\left(S_{zzxx}\sigma_{xx}^{m} + S_{zzyy}\sigma_{yy}^{m} + \Lambda_{zz}\Delta P + \alpha_{zz}\Delta T + \beta_{zz}\Delta(MC) + \chi_{zz}\Delta v_c\right) \tag{4-56}$$

4.4.2 Governing Equations for RTG - Arrhenius Type Rate Equations

In modeling the RTG tests, Sullivan et. al [38] modeled the chemical reactions by using a 4-step Arrhenius type rate equation:

$$R_k = \frac{\partial c_k}{\partial t} = -A_{a_k} c_k^{n_k} \exp\left(\frac{-E_{a_k}}{RT}\right) \tag{4-57}$$

where c_k is the degree of conversion for the kth reaction, A_{a_k}, n_k, and E_{a_k} are the Arrhenius constants and k = 1, 2, 3, 4. However, McManus [40] argued that Eqn. 4-57 is not a proper physical model of the chemical reactions, since it can generate gases even if the pressure at the point of generation is higher than the saturation pressure of the assumed gaseous substance. For this reason, McManus [40] developed a pressure-dependent Arrhenius type rate

equation such that the gas generation rate above the saturation pressure proceeds at an arbitrarily small rate. McManus further assumed that the mechanism that limits the reaction rate is due to an increase in the activation energy (E_{a_k}) with pressure. Eqn. 4-57 is then solved for E_{a_k} at a known value of pressure:

$$E_{a_k} = RT_{sat}(P) ln\left[\frac{C_k^{n_k} A_{a_k}}{\xi_k}\right] \tag{4-58}$$

where $T_{sat}(P)$ is the saturation temperature of the gas at pressure P and ξ_k is the arbitrarily small reaction rate, R_k. In computing the value of E_{a_k}, a value of 0.01 is selected for ξ_k [40]. It is assumed that in the first two steps of the chemical reactions the gas produced is steam. Therefore, $T_{sat}(P)$ can be determined from the steam tables [41]. The resulting E_{a_k} for the first two steps of the chemical reaction are tabulated in Table 4.1. The latter two steps of the 4-step chemical reaction model are assumed to be pyrolysis reactions and are independent of pressure. Therefore, the activation energies are constant. The values for the activation energy of the pyrolysis reactions are tabulated in Table 4.2. The other Arrhenius constants for pressure-dependent and pressure-independent models are tabulated in Tables 4.2 and 4.3.

4.4.3 CM-5 Implementation - RTG

Both the pressure-dependent and pressure-independent Arrhenius rate equations are incorporated into the pressure computation (Eqn. 4-43). More details can be seen in Appendix C. The pressure value is then determined for

Table 4.1. Pressure-dependent Activation Energy (E_a) [40].

Pressure (atm)	Reaction 1 E_{a_1} MJ/kg mole	Reaction 2 E_{a_2} MJ/kg mole
0	88.76	117.24
1	88.76	117.24
2	90.64	117.24
5	98.24	117.24
10	104.71	117.24
20	112.11	117.24
50	124.13	119.23
100	135.00	129.67
200	147.94	142.10
2000	147.94	142.10

Table 4.2. Pressure-dependent Arrhenius Constants [40].

Model	Reaction Number	E_{a_i} MJ/kg mole	A_{o_i} 1/sec	n_i
Pressure-dependent Arrhenius	1	*	1.20×10^{10}	3.5
	2	*	4.05×10^{9}	6.5
	3	211.4	3.86×10^{14}	6.5
	4	272.1	5.58×10^{13}	3.3

*See Table 4.1.

Table 4.3. Arrhenius Constants for Pressure-independent Model [40].

Model	Reaction Number	E_{a_i} MJ/kg mole	A_{o_i} 1/sec	n_i
Pressure-independent Arrhenius	1	88.76	1.20×10^{10}	3.5
	2	117.24	4.05×10^{9}	6.5
	3	211.4	3.86×10^{14}	6.5
	4	272.1	5.58×10^{13}	3.3

each time step. The temperature value at each time step is determined from the know heating rate, dT/dt. Then, σ_{zz}^{n} along the strip $y = 0$ (Figure 4-9) is determined from Eqn. 4-56. The resulting σ_{zz}^{n} calculated based on pressure-dependent and pressure-independent Arrhenius type rate equations are presented and discussed in Chapter 5.

CHAPTER 5

RESULTS AND DISCUSSIONS

In this chapter, results from the solutions of the three problems considered are presented and discussed. The results of the transpiration cooling analysis are used to verify the explicit finite difference method (EFDM) and to justify an important simplification used in the solutions of the ablative composite plate and RTG problems: the steady-state assumption in the stress calculations. Results from the ablative composite plate problem are used to demonstrate the capability of the hybrid algorithm to incorporate complex physics. An improvement in the model made possible by including the gas storage term in the pressure calculation is studied parametrically. The RTG results are used to study another, different, complex problem. The effects of two different chemical reaction models, a pressure-independent Arrhenius type rate equation and a pressure-dependent Arrhenius type rate equation are explored with this model. Finally, a performance study of the hybrid algorithm is presented and discussed.

5.1 Transpiration Cooling

In this problem, a plate made of porous material (aluminum) heated on one side is cooled by sending a gas flow (H_2O vapor) from the cool side to the hot side. The properties of the porous plate and the cooling gas used in the computation are listed in Table 5.1. The temperature and pressure values are fixed on both sides of the porous plate (Figure 4-2). On one side of the

Table 5.1 Properties for Porous Plate and Cooling Gas.

Properties	Symbol	Units	Value
Specific Heat of Porous Solid	C_{P_s}	J/(kg K)	167
Specific Heat of Gas	C_{P_g}	J/(kg K)	2000
Porosity of Solid	ϕ	dimensionless	0.05
Area-average Thermal Conductivity	K_c	W/(m K)	150
Permeability of Porous Solid	γ	m^2	$1x10^{-17}$
Gas Viscosity	μ	N s/m^2	$1x10^{-5}$
Molecular Weight of Gas	M	kg/kmole	18
Young's Modulus of Porous Solid	E	Pa	$70x10^9$
Poisson's Ratio of Porous Solid	υ	dimensionless	0.3
Damping Coefficient of Porous Solid	c[a]	N s/m^4	$1.0x10^8$
Intrinsic Density of Porous Solid	ρ_s	kg/m^3	2700
Plate Thickness	h	mm	30
Thermal Expansion Coefficient of Porous Solid	α	1/K	$1.2x10^{-5}$

[a] Value of the damping coefficient is computed from Eqn. 4-10 by setting the nondimensional damping coefficient, ς, to 0.1.

plate (z = 0mm), the displacements are fixed. On the other side of the plate (z = 30mm), the surface tractions are prescribed. The values used for the temperature, pressure, and surface tractions on the boundaries are listed in Table 5.2. Initially, the temperature and pressure distributions in the porous plate are uniform and the porous plate has zero displacement and velocity. The initial temperature, pressure, displacement, and velocity values are given in Table 5.3.

To verify the explicit finite difference method (EFDM), the computed steady-state temperature and pressure distributions are compared with analytical solutions for two different values of boundary pressure. The pressures used (0.2 MPa and 2.0 MPa) resulted in steady state gas mass fluxes of $\hat{m}_g$=0.034 and 4.90 kg/s m^2, respectively. The analytical solutions for the steady-state temperature and pressure distributions are given by the following three equations [42, 43]:

$$T(z) = \frac{T_2 - T_1}{\left[1 - exp(h/\delta)\right]}\left[1 - exp(z/\delta)\right] + T_1 \tag{5-1}$$

$$P(z) = \sqrt{\left[P_{max}^2 - \left(P_{max}^2 - P_2^2\right)\frac{z}{h}\right]} \tag{5-2}$$

or

$$P(z) = \sqrt{\left[P_{max}'^2 - \frac{2Rh\hat{m}_g}{M\gamma}F(z)\right]} \tag{5-3}$$

where δ, P_{max}, P'_{max}, and $F(z)$ are given by:

$$\delta = \frac{K_z}{\hat{m}_g C_{P_g}} \tag{5-4}$$

$$P_{max} = \sqrt{\frac{2h\hat{m}_g RT\mu}{M\gamma} + P_2^2} \tag{5-5}$$

Table 5.2 Boundary Conditions

	z = 0 mm	z = 30 mm
Pressure (Pa)	P_1=2x10^5 or 2x10^6	P_2=1x10^5
Temperature (K)	T_1=273	T_2=373
Tractions (Pa)	T_i^b = unknown	T_i^b = 0
Displacement (m)	u_i=0	u_i=unknown

Table 5.3 Initial Condition Everywhere in Plate.

Initial Temperature (K)	273
Initial Pressure (Pa)	$1x10^5$
Initial Displacement (m)	0
Initial (velocity)	0

$$P'_{max} = \sqrt{\frac{2h\hat{m}_g R\mu}{M\gamma} F(h) + P_2^2} \tag{5-6}$$

$$F(z) = T_1 \frac{z}{h} + \frac{1}{2}(T_2 - T_1)\frac{z^2}{h^2} \tag{5-7}$$

The notation used is given in Table 5.1; R is the universal gas constant. The steady-state temperature distribution (Eqn. 5-1) can be derived from the governing equation of temperature for the transpiration cooling problem (Eqn. 4-15) by setting the left hand side to zero and assuming that all coefficients on the right hand side are constant. The first steady-state pressure distribution (Eqn. 5-2) is derived using Darcy's law (Eqn. 4-2) by assuming constant coefficients and uniform through-thickness temperature distribution. The second steady-state pressure distribution (Eqn. 5-3) is derived in the same manner as in Eqn. 5-2 with a linearly varying temperature distribution through the thickness. Equation 5-2 which is exact only for a uniform temperature, is used for the relatively high mass flux case ($\hat{m}_g$ = 4.90 kg/s m^2) which is insensitive to the temperature distribution. Equation 5-3 is used for the relatively low mass flux case ($\hat{m}_g$ = 0.034 kg/s m^2) where the through-thickness temperature distribution can be approximated as linear. The computed results are shown in Figures 5-1 and 5-2 along with the analytical solutions for temperature and pressure. As shown in Figures 5-1 and 5-2, the computed results agree fully with the analytical solutions. These results lend confidence in the EFDM solution scheme.

Transient temperature distributions are shown in Figure 5-3. The temperature distribution rises from the initial condition to the steady-state distribution in approximately one second. The relatively fast response is due to the high thermal conductivity material assumed in the computation. The time for the temperature distribution to reach steady-state has been checked

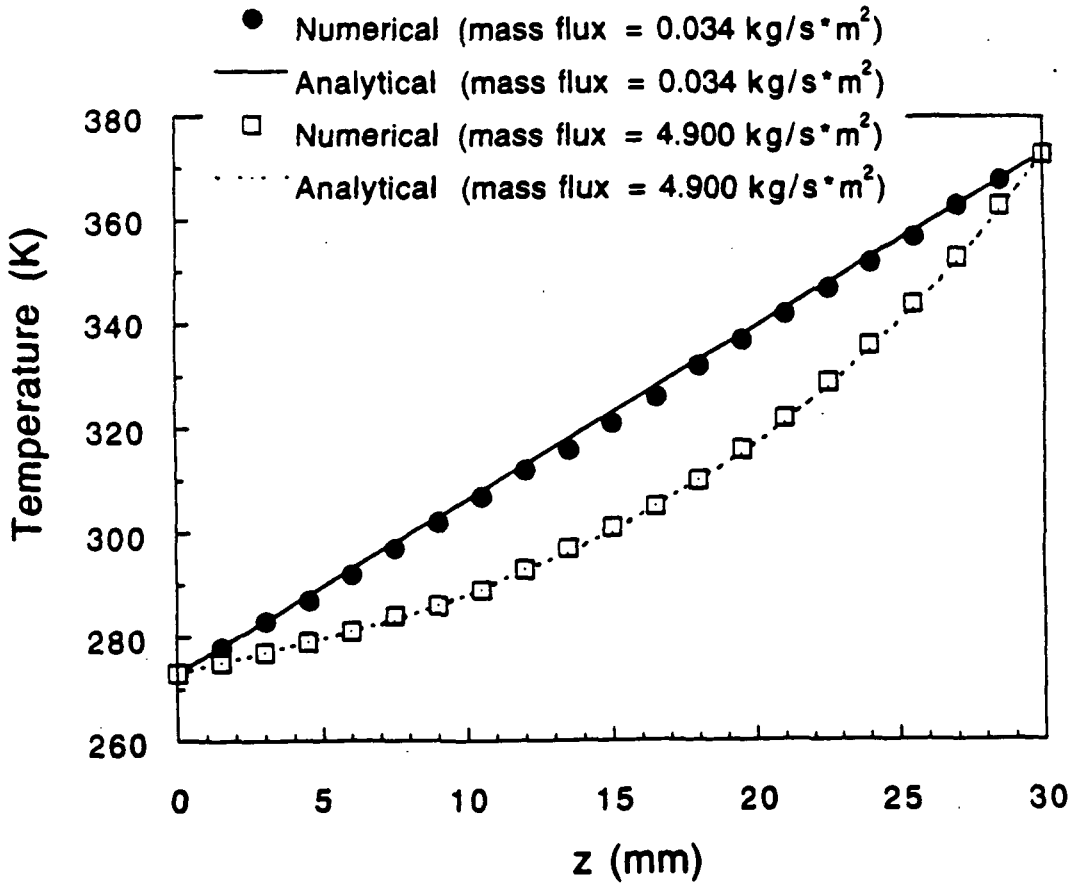

Figure 5-1. Numerical and analytical steady-state temperature distributions for two different gas mass fluxes.

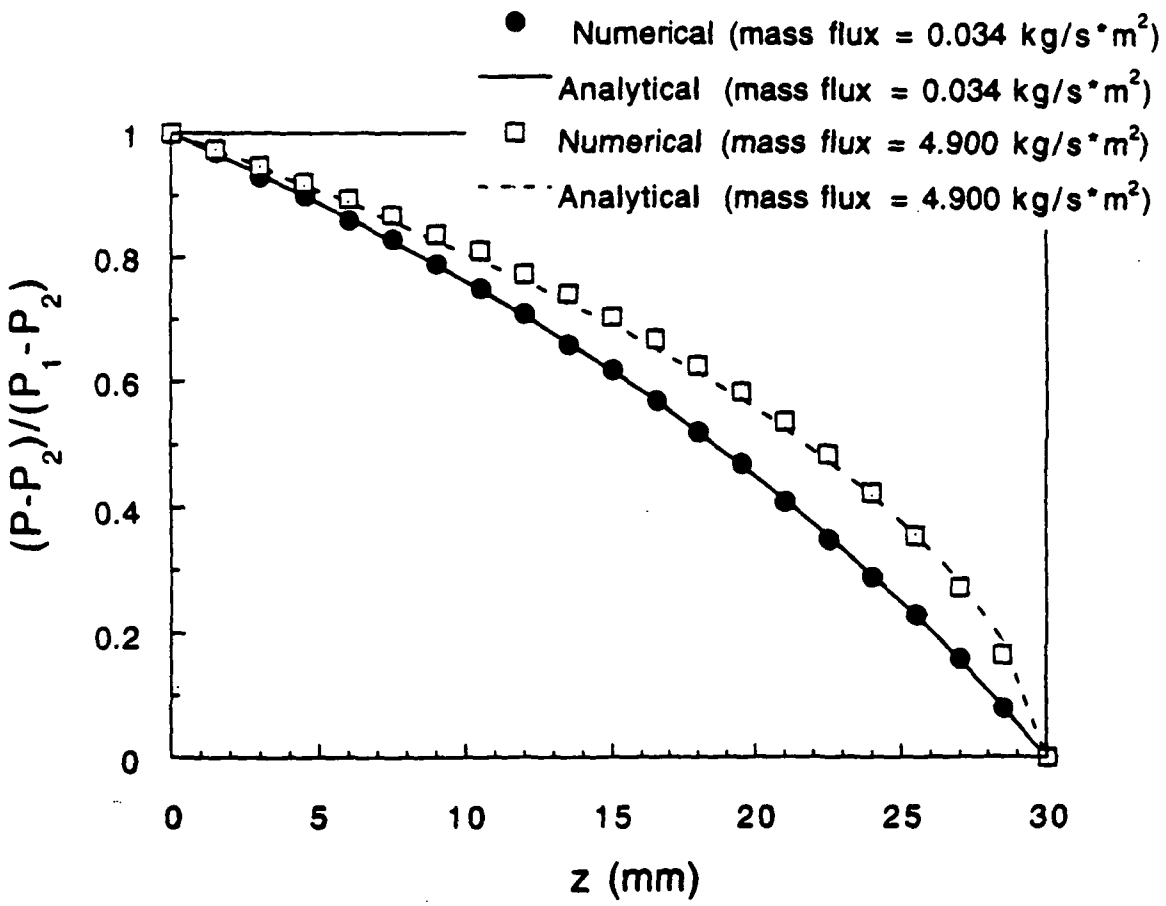

Figure 5-2. Numerical and analytical steady-state pressure distributions for two different gas mass fluxes.

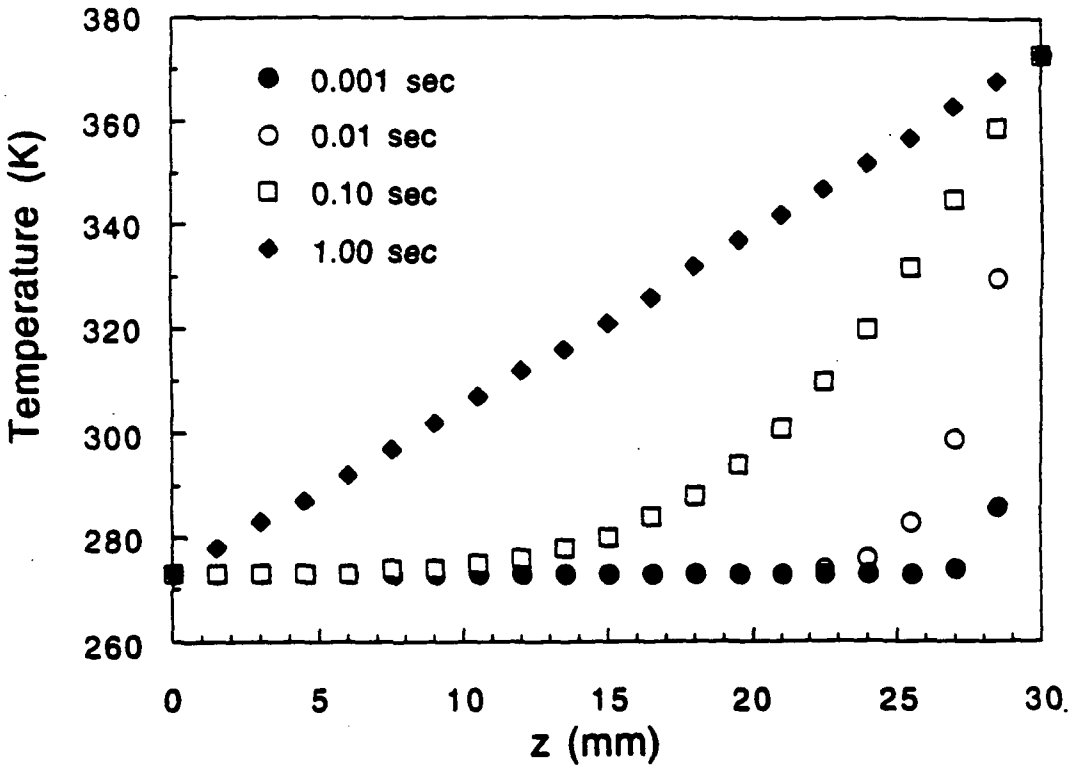

Figure 5-3. Transient temperature distributions for four different simulation times: (1) 0.001 second, (2) 0.01 second, (3) 0.10 second, and (4) 1.00 second.

against an available analytical solution [44]. This time is found to be in good agreement with the analytical solution. The analytical solution in reference [44] is obtained by ignoring the gas mass flux term in Eqn. 4-15. The comparison made here is appropriate, but reasonable, since the gas mass flux is relatively small in this case ($\hat{m}_g$ = 0.034 kg/s m^2).

Transient pressure distributions are shown in Figure 5-4. There are two things worth noting: (1) there is a small spatial oscillation in the pressure distribution early in the analysis (0.001 second) and (2) the pressure distribution reaches steady state about 100 times faster than the temperature distribution. The small spatial oscillation in pressure is due to a sharp temperature rise near one boundary (z = 30mm) which increases the gas pressure before the flow of gas from the other boundary (z = 0 mm) reaches there. This sharp rise in temperature can be seen from Figure 5-3 at 0.001 second.

Transient stress distributions (σ_z'') are shown in Figure 5-5 for four different simulation times: (1) 0.001 second, (2) 0.01 second, (3) 0.10 second, and (4) 1.00 second. The steady-state gas mass flux value is 0.034kg/s m^2 which corresponds to P_1 = 0.2 MPa in Table 5.2. The stress response is relatively fast. This conclusion is reached by noting that the stress distribution has the same shape as the pressure distribution by about 0.001 second. This result is predicted for steady-state stresses by poroelasticity theory [16-21]. At a very early time (t = 0.0001 sec), a transient oscillation in stress can be seen from Figure 5-6. This is caused by an impulsive application of the surface pressure (P_1). In the actual situation, the application of surface pressure is relatively gradual. When the surface pressure is applied gradually, the effects of the oscillatory transient stress is

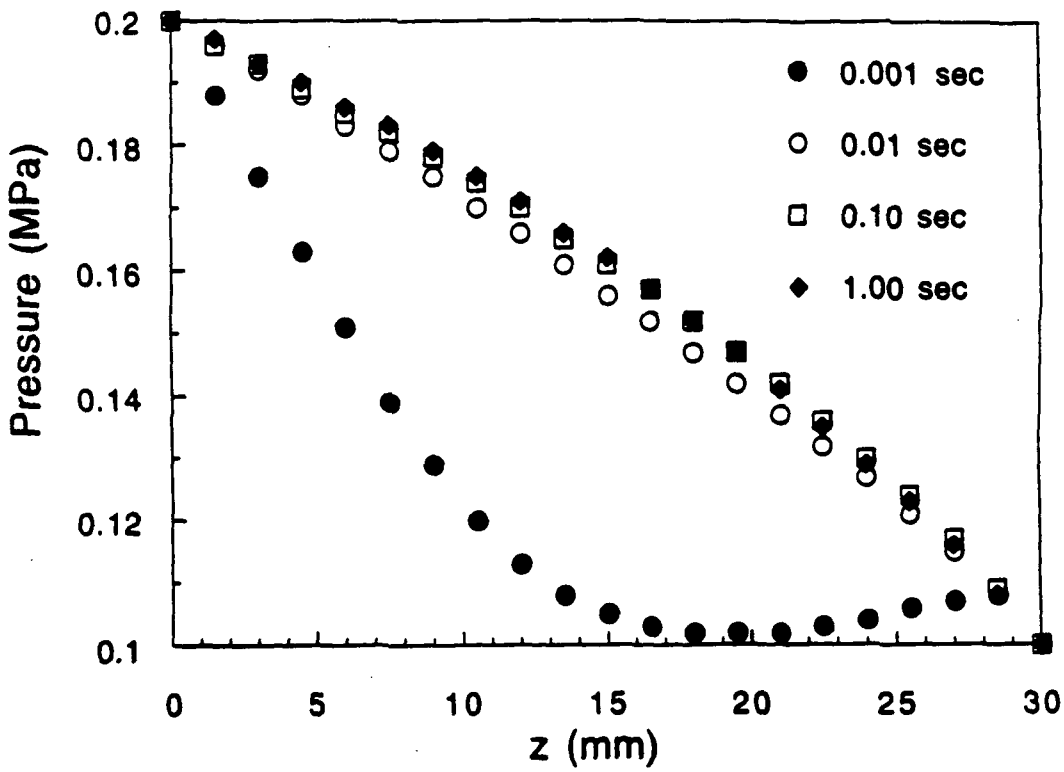

Figure 5-4. Transient pressure distributions for four different simulation times: (1) 0.001 second, (2) 0.01 second, (3) 0.010 second, and (4) 1.00 second.

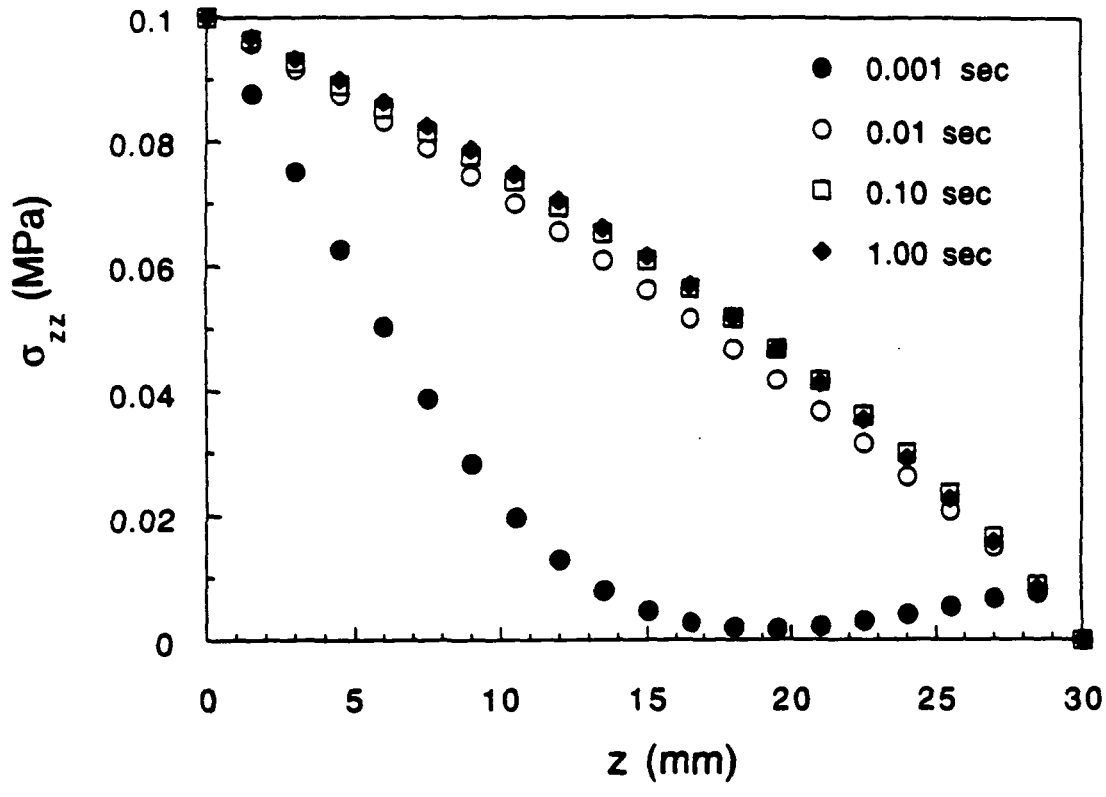

Figure 5-5. Transient stress (σ_{zz}^{m}) distribution for four different simulation times: (1) 0.001 second, (2) 0.01 second, (3) 0.10 second, and (4) 1.00 second.

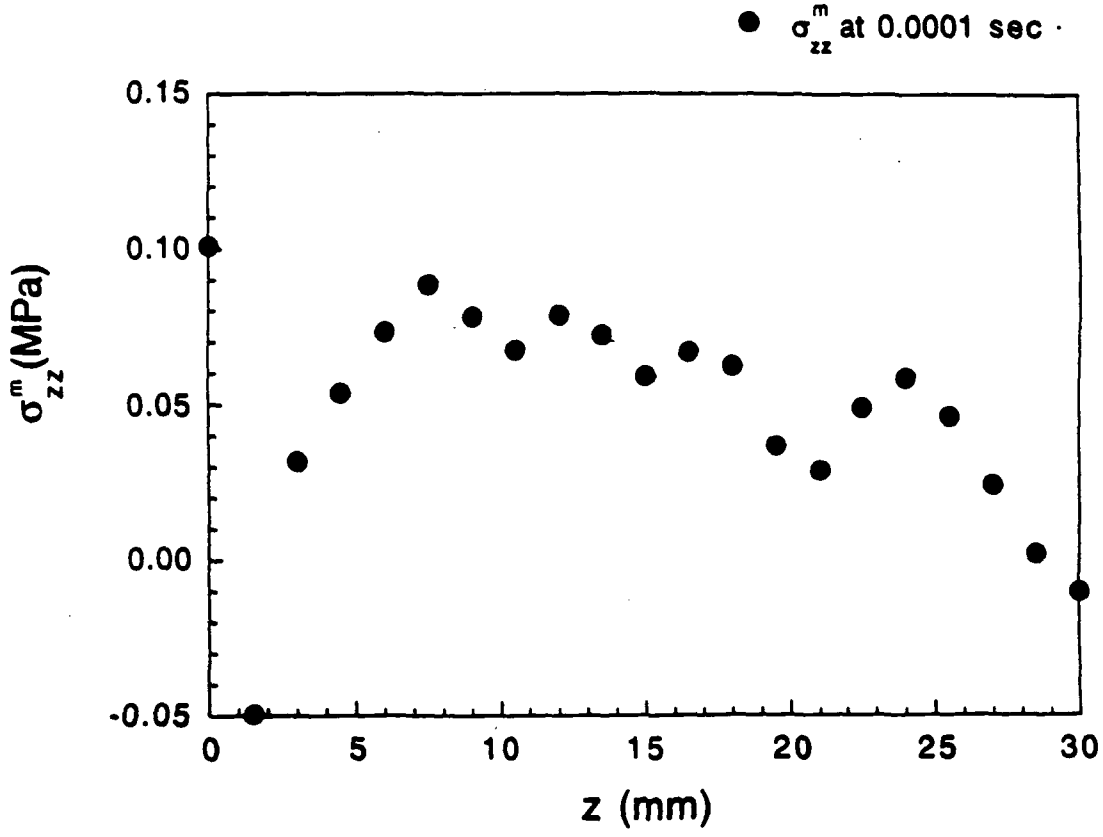

Figure 5-6. Transient stress (σ^m_{zz}) distribution for simulation time of 0.0001 second. The expected oscillatory stress distribution is observed.

not significant. In order to mimic the actual situation more closely in the analysis, an unrealistically high damping value ($\varsigma = 0.1$) was used to reduce the effects of the transient stress.

The temperature, pressure, and stresses all reach steady state at different times. This observation suggests that each physical process (temperature, pressure, and stress) has its own characteristic time scale ($t_{temperature} << t_{pressure} << t_{stress}$). In EFDM, if a single time step Δt is used for all calculations, it must be smaller than the characteristic time scale of the fastest physical process (in this case, that of stress) to assure overall stability of the numerical scheme. The slower physical processes (in this case, temperature and pressure) are calculated with time steps smaller than required. Therefore, the computations are done many more times than necessary.

A first step made towards alleviating the stability problem in the EFDM is to assume that the stress response is quasistatic. The assumption is justified since the oscillatory transient stress is neither important nor realistic. The quasistatic stress response assumption is in agreement with the assumptions made without justification by Kuhlmann [11], McManus [12], and Sullivan [13].

The same idea can be extended to the pressure calculation as well. Notice that in this analysis the pressure distribution reaches steady-state about 100 times faster than that of temperature due to the relatively high value of permeability assumed for the porous plate. This observation suggests that when the permeability of the porous plate is high enough, it can be assumed that the pressure response is quasistatic.

5.2 Ablative Composite Plate

In this sample problem, an ablative composite plate is used to model the lining of a rocket nozzle exit cone. The in-plane dimensions of the lining are much greater than the through-thickness dimension. Also, heat flux, pressure, and surface tractions are assumed to uniformly applied over the surface of the lining. Hence a 1-D analysis will suffice to capture the response of the lining. The properties of the ablative composite plate (FM5055) and the flowing gases are taken from reference [12]. These properties are listed in Appendix E. The properties given are on-axis (x_1-x_2-x_3) properties (see Figure 5-7). In order to relate the on-axis properties to the off-axis (x-y-z) properties, two rotations need to be performed. The first rotation is about the x_3 axis and the second rotation is about the y axis. The method used to rotate the properties is described in Appendix F.

The geometry of the plate is shown in Figure 4-4. The plate has a thickness h equal to 3cm. The ply and fiber angles are $\Phi = 15^\circ$ and $\theta = 45^\circ$, respectively. On the exposed side of the plate (z = 3cm), heat flux, ambient pressure, and surface tractions are specified. On the insulated side (z = 0cm), the heat flux, gas mass flux, and displacements are specified. Initially, the temperature and pressure are uniformly distributed through the thickness of the plate. The initial values of the temperature and pressure are 25 °C and 1 atm, respectively. The initial moisture content (MC_o) is 3 percent. The simulation time is 105 seconds. In the first 100 seconds, the boundary conditions on the surface (z = 3cm) are held constant. In the last five seconds, the ambient temperature, the ambient pressure, and the convective heat transfer coefficient are reduced over a five second period to

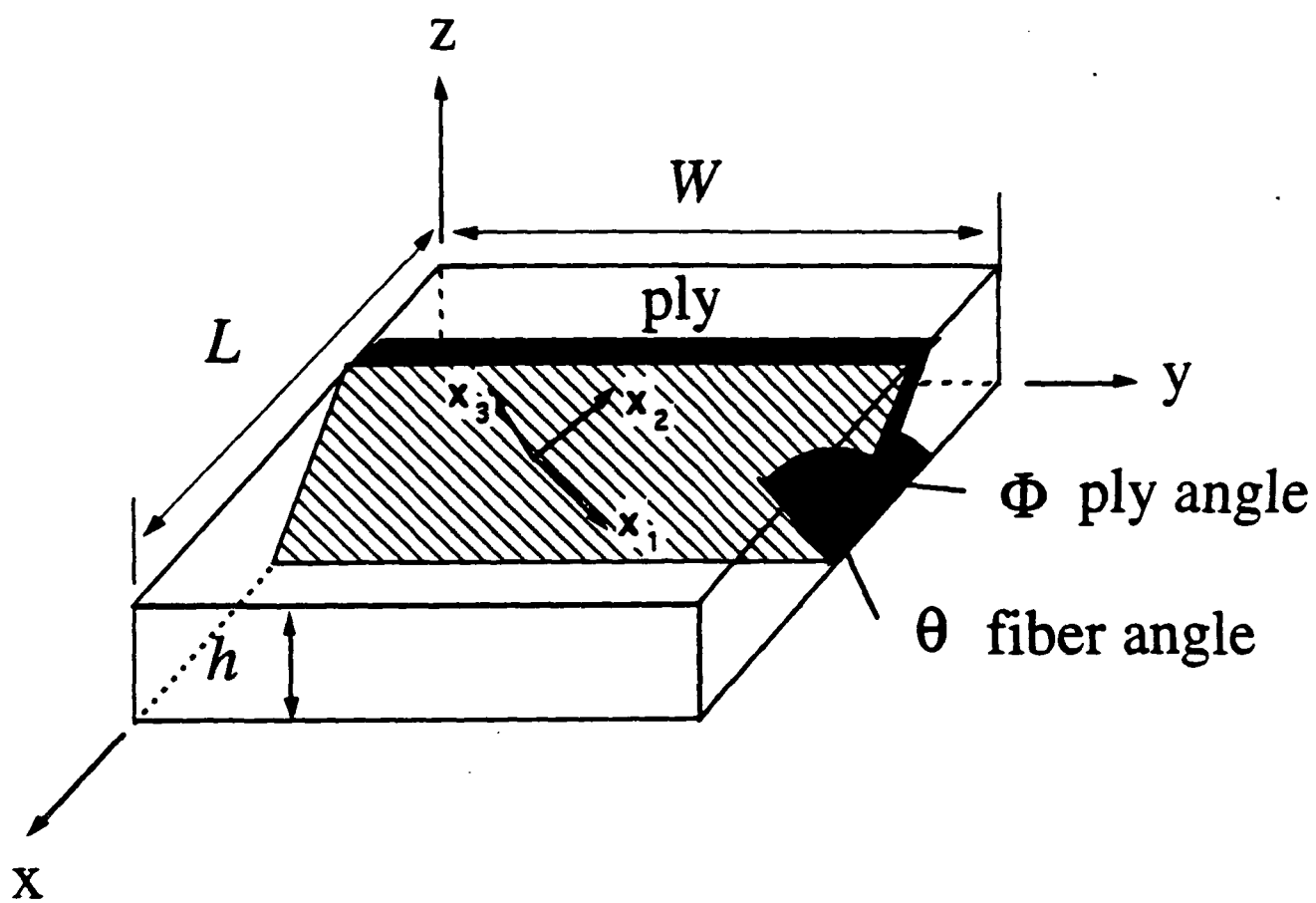

Figure 5-7. On-axis and off-axis coordinate systems [12]. The on-axis system is denoted by x_1-x_2-x_3. The off-axis system is denoted by x-y-z.

25°C, 1 atm, and 90 W/m^2, respectively. These conditions are used to simulate the firing (time < 100 sec) and shutoff (time > 100 sec) of the rocket motor. The boundary and initial conditions are listed in Tables 5.4 and 5.5.

The temperature and pressure distributions are obtained using the hybrid algorithm described in Section 4.3.2 of Chapter 4. A mesh of 251 nodes and a fixed time step of 0.001 second are used. Whenever the critical time scale ($\Delta t_{cr} = \Delta z^2/|P\gamma/\phi\mu|$) becomes less than 0.001 second at a given node, the solution scheme for pressure and temperature at that node is switched from EFDM to IFDM automatically by the code.

Temperature distributions at 10, 50, 80 and 104 seconds are shown in Figure 5-8. As expected, the temperature is highest at the surface of the plate for the first 100 seconds since the surface is exposed to the ambient environment of the rocket motor. After shutoff, the value of temperature on the surface drops below that on the inside. This is shown by the temperature distribution at 104 second. These four temperature distributions are almost the same as those obtained by McManus [12]. Note that the previous temperature distributions were obtained without the inclusion of the mass storage term in Eqn. 4-27. Hence, the results suggest that the mass storage term does not have much effect on the through thickness temperature distributions.

Four pressure distributions are shown in Figure 5-9 at 10, 50, 80, and 104 seconds. The first three pressure distributions reach a peak then drop off. These results are different from the results shown in reference [12] which did not include the mass storage term.

Table 5.4. Boundary Conditions.

Boundary Conditions	
z = 0mm	z = 30mm
Surface Emissivity none	Surface Emissivity[a], $\varepsilon = 5.1\text{x}10^{-1}$
Boltzmann's Constant none	Boltzmann's Constant[a], $\sigma = 5.670\text{x}10^{-8}$ W/m^2 K^4
Surface Absorptivity none	Surface Absorptivity[a], $\alpha = 4.9\text{x}10^{-1}$
Effective Black Body Temp. none	Effective Black Body Temp.[a], $T_e = 3023$ K
Convective Heat Transfer Coef. none	Convective Heat Transfer Coef.[b,c], $h_{c1} = 450$ W/m^{2}K $h_{c2} = 100$ W/m^2 K
Ambient Temperature, N/A	Ambient Temperature[b,c], $T_{\infty 1} = 3023$ K $T_{\infty 2} = 298$ K
Insulated $\mathbf{q}_{tot} = 0.0$ W/m^2	Heat Flux, $\mathbf{q}_{tot} = \mathbf{q}_{rad}$[a]$+\mathbf{q}_{conv}$[b]
Impermeable, $\hat{m}_g = 0.0$ kg/s m^2	Ambient Pressure[c], $P_{b1} = 10$ MPa $P_{b2} = 0.1$ MPa
Fixed Displacements, $u_i = 0$ mm	Surface Tractions, $T_i^b = 0$ MPa

[a]The radiative heat flux, $\mathbf{q}_{rad}$, is given by the expression: $\mathbf{q}_{rad} = \sigma\left(\varepsilon T_{surf}^4 - \alpha T_e^4\right)$.

[b]The convective heat flux, $\mathbf{q}_{conv}$, is given by the expression: $\mathbf{q}_{conv} = h_c(T_{surf} - T_\infty)$.

[c]For the first 100 seconds the convective heat transfer coefficient, ambient temperature, and ambient pressure are given by the value with the subscript one. For times greater than 100 seconds, these values are reduced linearly over a five second period to the value with the subscript two.

Table 5.5. Initial Conditions Everywhere in Plate.

Initial Pressure	Initial Temperature
0.1 MPa	298 K

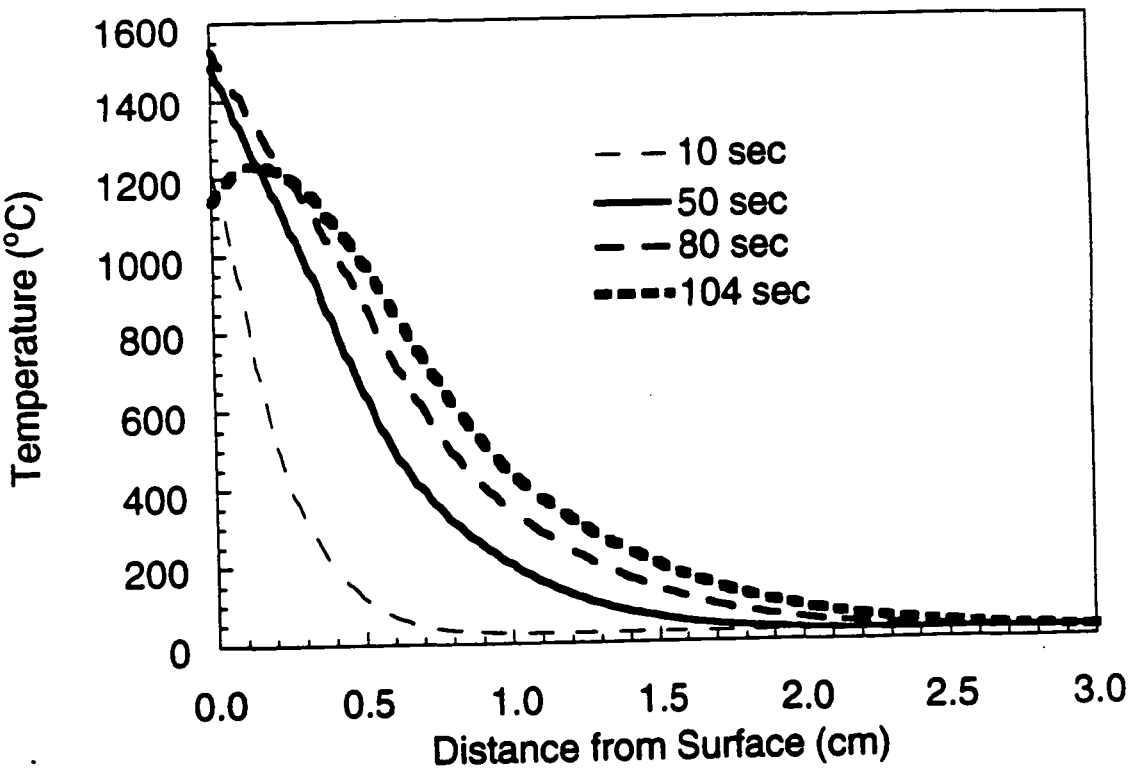

Figure 5-8. Through-thickness temperature distributions at 10, 50, 80, and 104 seconds.

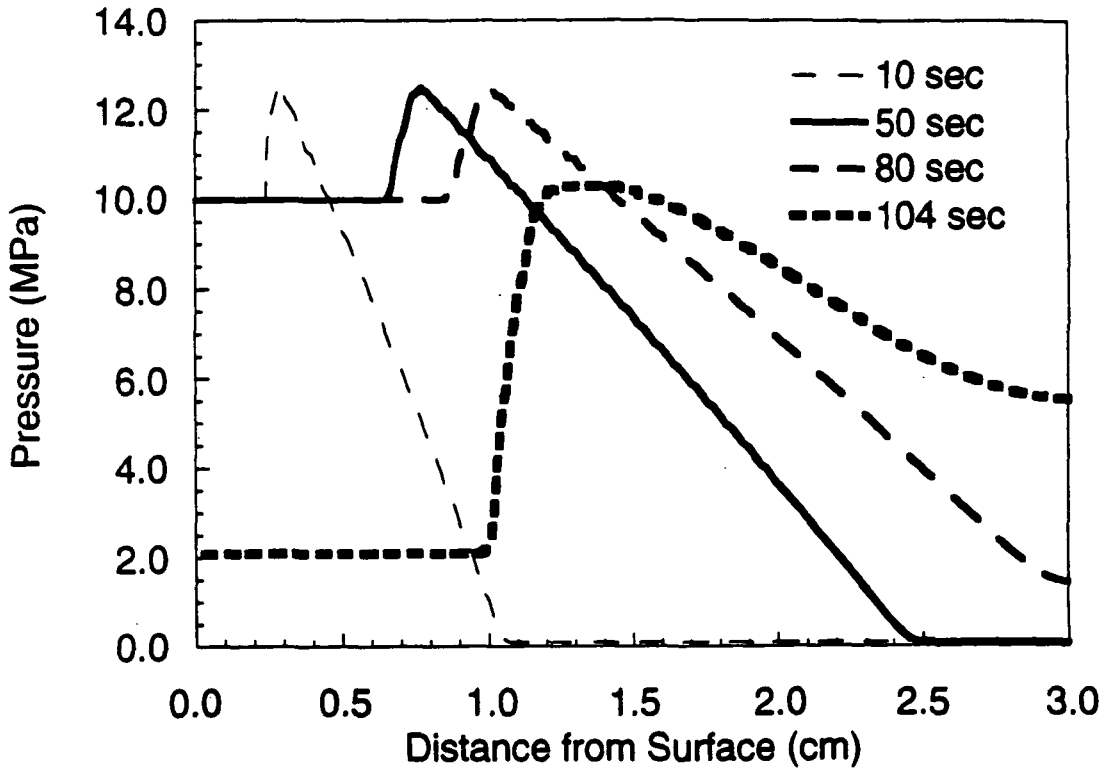

Figure 5-9. Through-thickness pressure distributions at 10, 50, 80, and 104 seconds.

However, the locations where the maximum pressures occur are approximately the same in the results of this study and that of reference [12]. Also notice that when the peak pressure value is reached, it remains relatively constant in magnitude and simply moves inward as time progresses. This observation implies that a continuous chemical reaction front is established [40]. In order to capture this phenomena, a relatively fine mesh needs to be used. In this case, a mesh containing 251 nodes is used. According to reference [40], a mesh of at least 151 nodes is necessary to capture this phenomena. At 104 seconds, the ambient pressure is lowered from 10MPa to 2MPa. The peak pressure value at 104 seconds is lower than that of previous times. However, the difference between the boundary and the maximum internal pressure is the largest at this time. It was found in reference [12] that this difference is critical to the mechanism that causes delaminations (ply-lifts). The value of pressure differential at which ply-lifts occur for the current geometry ($\Phi = 15^\circ$ and $\theta = 45^\circ$) has been shown in [12] to be 6MPa. Then, according to Figure 5-9, ply-lifts are going to occur at 104 seconds since the pressure differential at that time is 8MPa. This is in agreement with reference [12].

The maximum pressure differential predicted by the current pressure model is compared with the values predicted by the previous model [12]. The results are shown in Figure 5-10. Overall, the current pressure model predicts a lower maximum pressure value than the previous model. In reference [12], it has been found that for smaller ply angle, $\Phi = 5^\circ$, ply-lifts can occur before the rocket motor shuts off. This implies that under the same conditions as analyzed in the previous study, the prediction by the current model may differ from that of the previous model. Also notice that the maximum pressure differential value predicted by the current model is

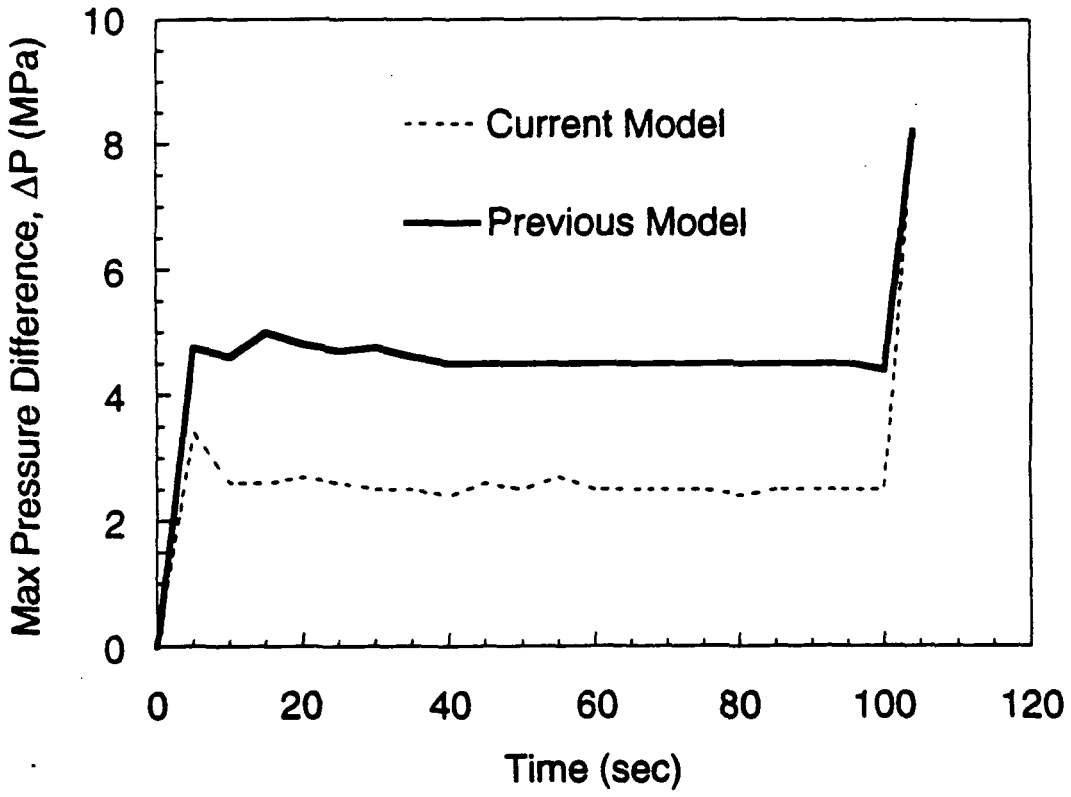

Figure 5-10. Maximum pressure difference comparison between current and previous models [37].

highest in the first 5 seconds, and then settles to a steady lower value. The previous model [12] does not predict the same phenomena. It simply rises to a peak value and remains at that value until shutoff.

Moisture loss and char volume as functions of position through the thickness of the plate are plotted in Figures 5-11 and 5-12 at 10, 50, 80, and 104 seconds. Both are expressed non-dimensionally, with 1.0 indicating complete charring or moisture loss. Both evaporation and charring reactions occur over a very narrow region and proceeds into the thickness of the plate with time. Also, the evaporation front precedes the char front. These observations are in agreement with the results from McManus's model [12]. However, the extent of both the evaporation and char regions are about 0.5 cm less than that predicted by McManus at the end of the calculations [12].

The through-thickness on-axis stress distributions at 104 seconds are shown in Figures 5-13 through 5-16. The stress distributions at 104 seconds are chosen because the maximum pressure differential occurs approximately at this time (see Figure 5-9). For each figure, two stress distributions are shown. The solid line distribution is showing only the internal pressure contribution to stress. This is achieved by setting the thermal expansion coefficient (α) to zero in the computation, hence excluding any thermal stress contributions. The dashed line distribution represents the overall contributions from both the internal pressure and thermal stresses.

For the current geometry (Φ = 15°, θ = 45°), the mechanical shear stresses ($\sigma^m_{x_1x_2}$ and $\sigma^m_{x_1x_3}$) are dominated by thermal stresses as shown in Figures 5-13 and 5-14. However, their magnitudes are quite small and do not exceed the failure strength of the material. Internal pressure and thermal stresses contribute approximately equally to the $\sigma^m_{x_1x_1}$ distribution (Figure 5-15). Note the magnitude of $\sigma^m_{x_1x_1}$ varies a great deal through the thickness.

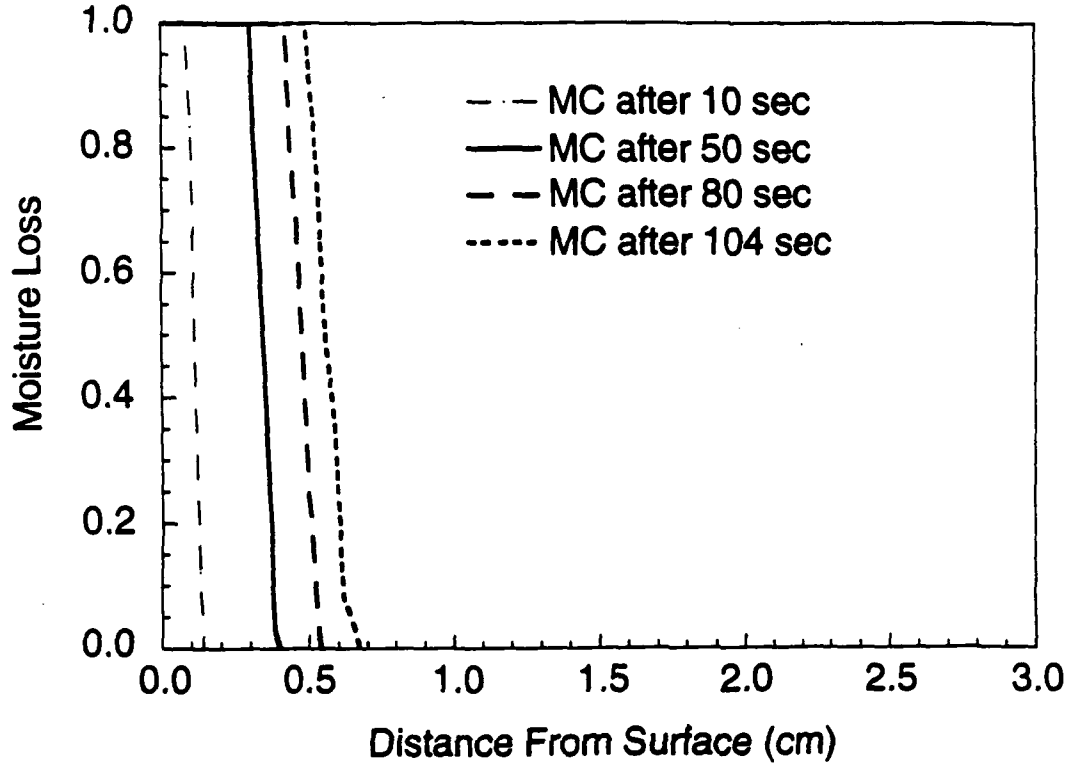

Figure 5-11. Moisture loss as a function of through-thickness position at 10, 50, 80, and 104 seconds.

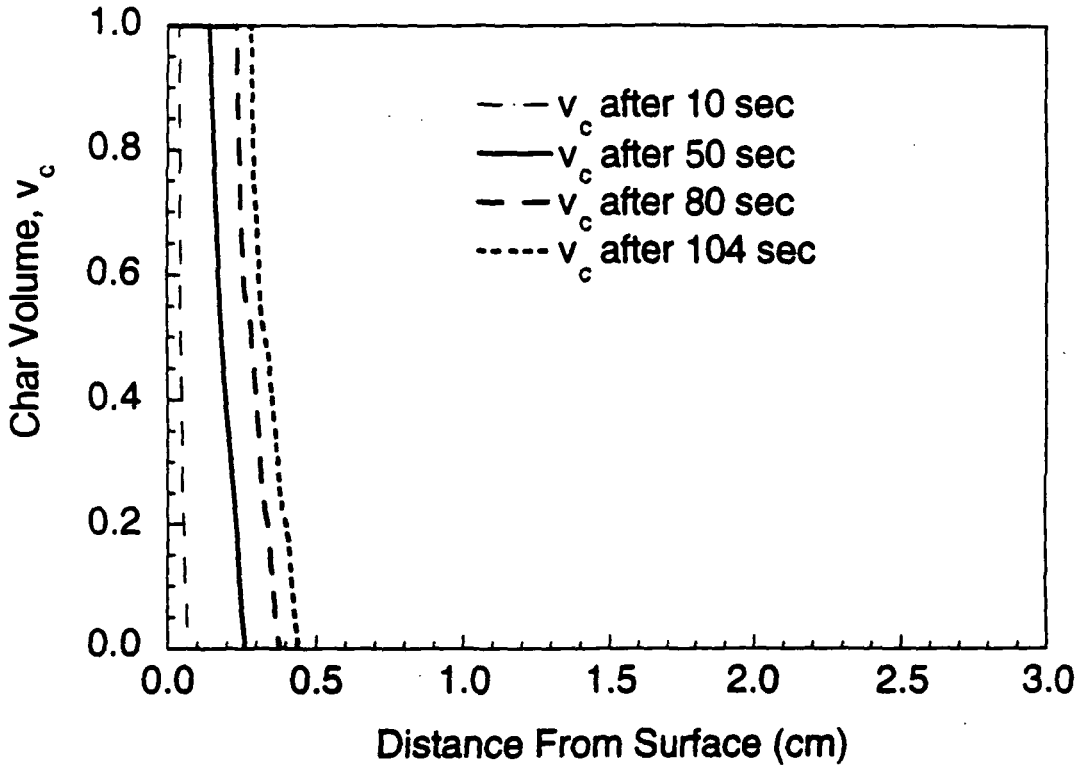

Figure 5-12. Char volume as a function of through-thickness position at 10, 50, 80, and 104 seconds.

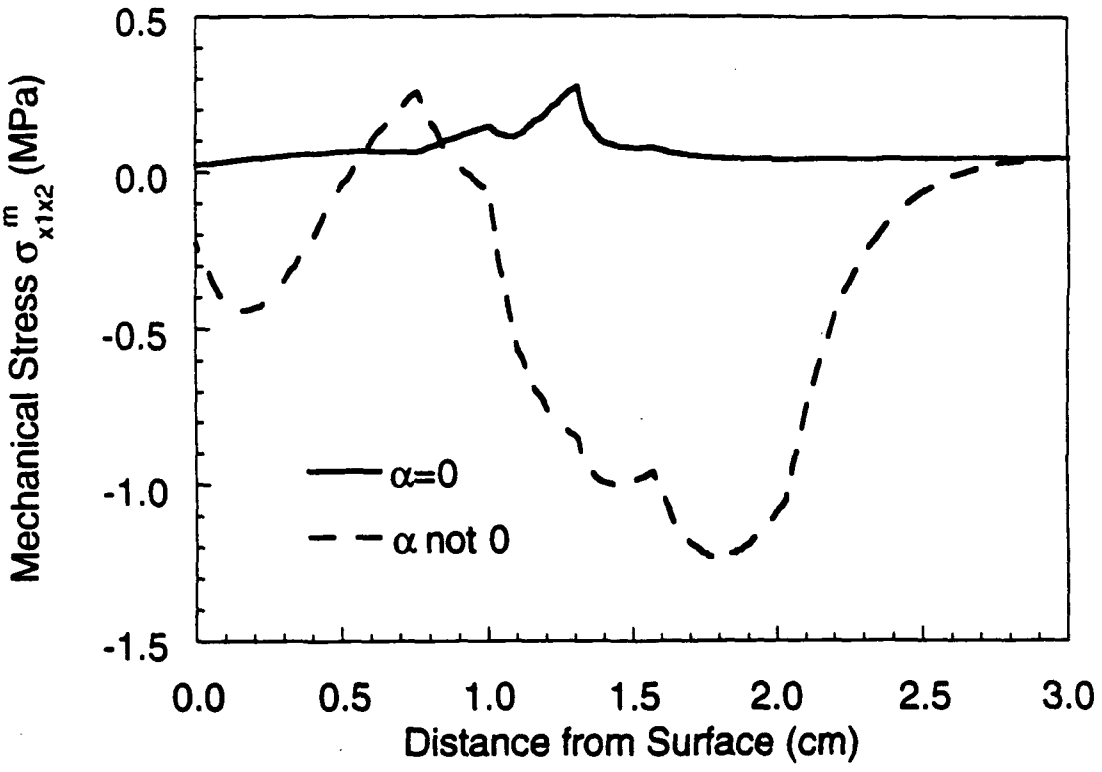

Figure 5-13. Mechanical $\sigma^{m}_{x_1x_2}$ distribution at 104 seconds.

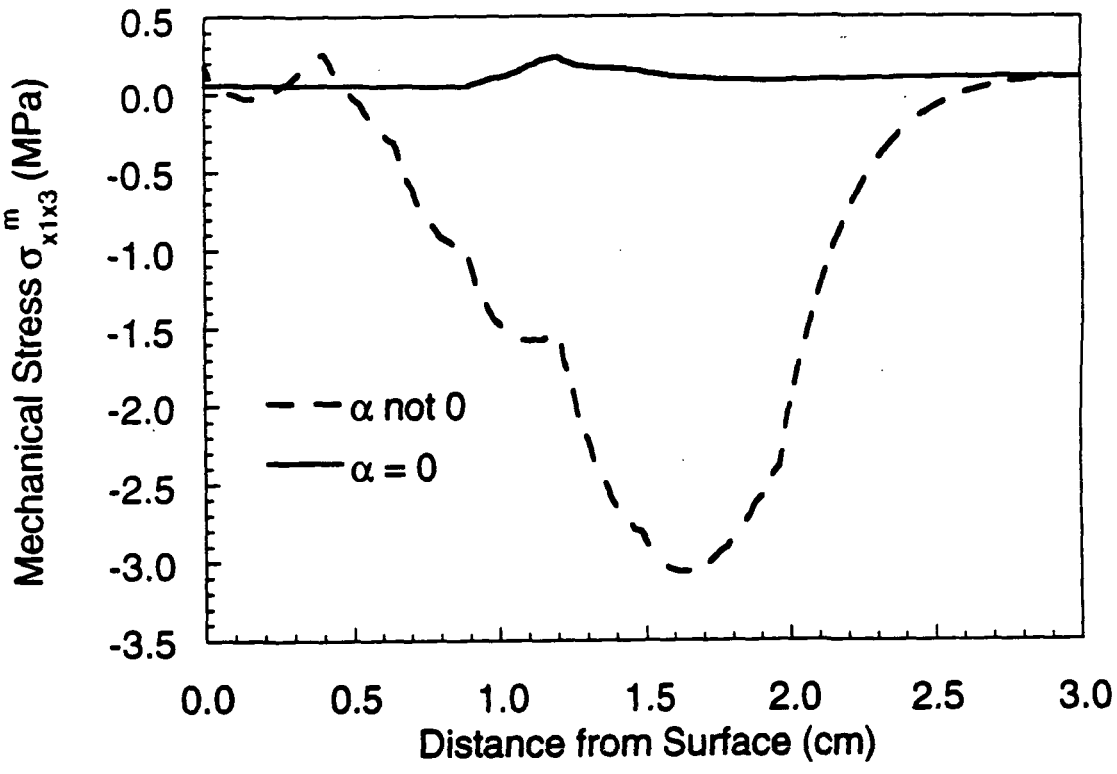

Figure 5-14. Mechanical $\sigma^{m}_{x_1x_3}$ distribution at 104 seconds.

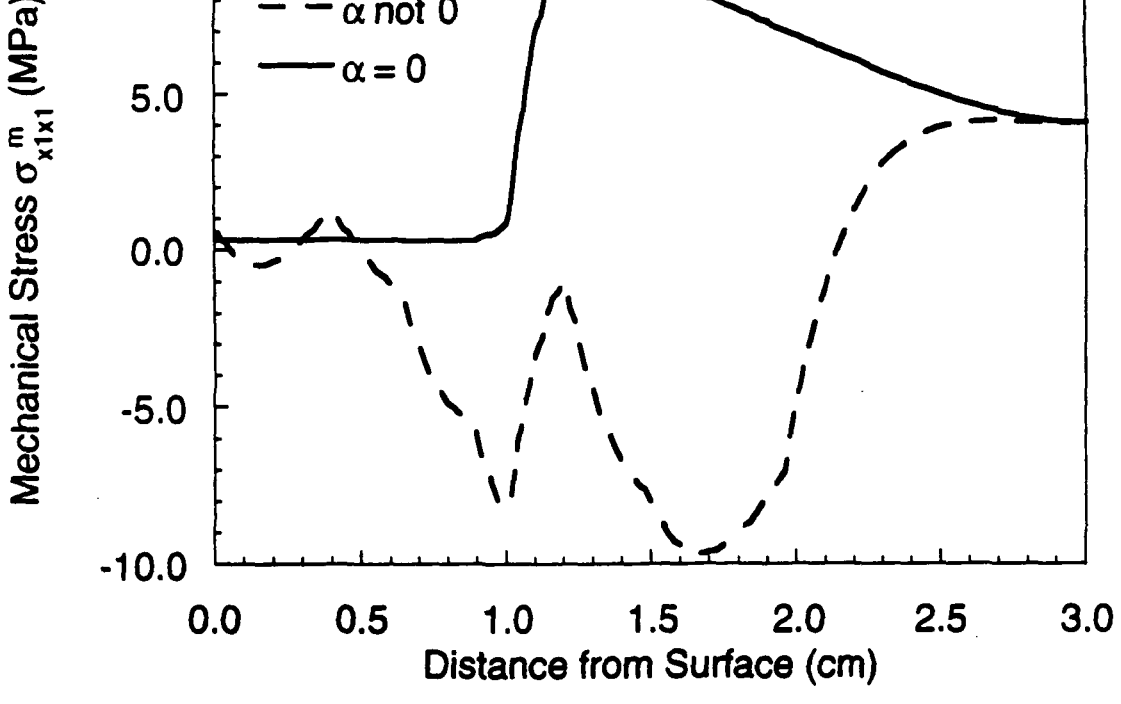

Figure 5-15. Mechanical $\sigma^{m}_{x_1x_1}$ distribution at 104 seconds.

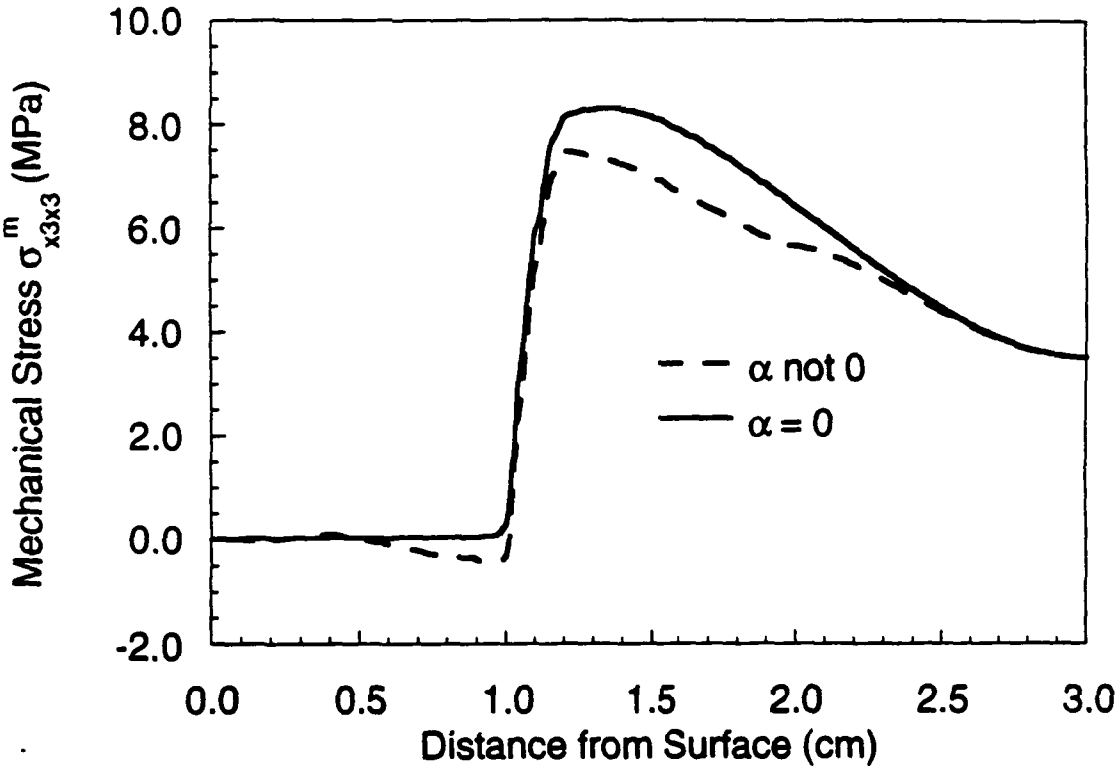

Figure 5-16. Mechanical $\sigma^{m}_{x_3x_3}$ distribution at 104 seconds.

This variation resembles the measured restraining stress at different temperatures for the restrained thermal growth (RTG) test. These results will be compared to the RTG experimental results in the following section. The distribution of $\sigma^m_{x_3x_3}$ is dominated by the internal pressure contribution shown in Figure 5-16. This is to be expected for a relatively small value of the ply angle $\Phi = 15^\circ$ [12]. In this case, the magnitude of $\sigma^m_{x_3x_3}$ is large enough to cause delamination (ply-lifts) according to the maximum stress failure criterion.

5.3 Restrained Thermal Growth (RTG)

In a restrained thermal growth (RTG) test, a cylindrical specimen is heated uniformly at a constant rate. The stress required to hold the specimen at a constant longitudinal strain is recorded. A schematic RTG test setup is shown in Figure 4-7. The measured restraining stresses to keep the specimen at a constant longitudinal strain for different temperatures are shown in Figure 4-8. In this section, the computed values of $\sigma^m_{x_1x_1}$ for the ablative composite plate problem are compared qualitatively to the experimental RTG results. Then the results of a direct numerical RTG simulation are shown and discussed. In the simulation two types of chemical reaction model are used: (1) pressure-dependent Arrhenius type rate equation and (2) pressure-independent Arrhenius type rate equation.

The results of an RTG experiment are shown side by side with the $\sigma^m_{x_1x_1}$ results from the ablative composite plate problem in Figure 5-17 for a qualitative comparison. Sullivan [38] has divided the measured material response into three regions: (1) thermoelastic, (2) transition, and (3) poroelastic. In the thermoelastic region the measured stress is a result of elastic thermal expansion. In the transition region the material response

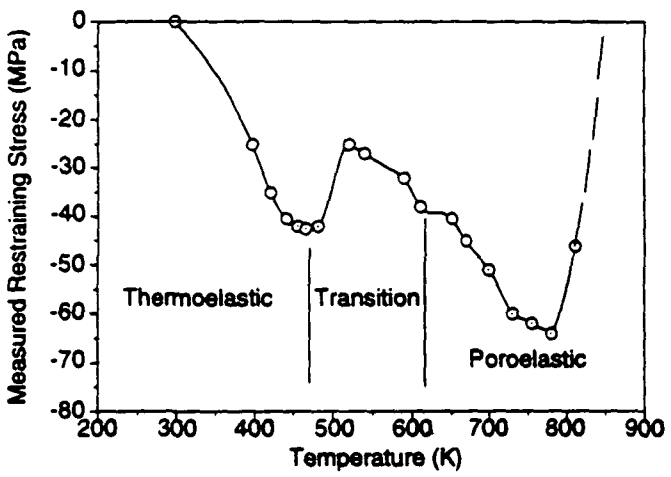

(a)

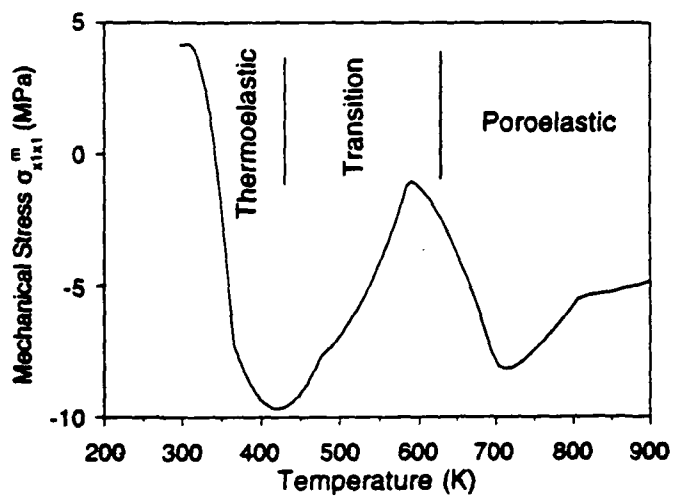

(b)

Figure 5-17. Comparison between experimental RTG and computed mechanical $\sigma^{m}_{x_1x_1}$ results.

changes from thermoelastic to poroelastic. The initial drop in the measured stress is due to material softening. As the temperature increases further, gases from the pyrolysis reaction begin to accumulate and the effects of the internal pressure become apparent. This causes an increase in the magnitude of the restraining stress. Finally, in the poroelastic region, the internal pressure becomes excessive and the response of the material is highly dependent upon the internal pressure, the material's permeability, and the material's poroelastic behavior. As one can see qualitatively, the computed results compare well with the experimental results. The three regions of material response are captured by the hybrid algorithm. The lack of quantitative agreement is due to the differences in geometry and boundary conditions between the RTG testing and the ablative composite plate.

In the numerical RTG simulation, the specimens have a radius of 0.635cm. The material properties used are the same as the ones listed in Table 1 of reference [38]. The boundary and initial conditions used in the numerical RTG simulation are listed in Tables 5.6 and 5.7, respectively. The values of the Arrhenius constants are listed in Appendix C.

The computed restraining stresses (σ_z^m) based on the pressure-dependent and pressure-independent chemical reaction models are shown along with the experimental results in Figure 5-18. Note that on the y-axis the absolute value of the compressive restraining stress is used. The pressure-dependent Arrhenius reaction model captures the trend of the RTG experiment better than the pressure-independent Arrhenius reaction model which does not capture the trend at all. The quantitative disagreement is due to the difference between the model geometry (a strip) and the real RTG geometry (a disc).

Table 5.6. Boundary Conditions Used for Numerical RTG Simulation

z=0 cm	z=0.635 cm
Impermeable, $\hat{m}_g$=0 kg/m^2 s	Fixed Ambient Pressure, P_b=0.1 MPa
Fixed Displacements, u_i=0 cm	Zero Surface Tractions, T_i^b=0 MPa

Table 5.7. Initial Conditions[a] Used in Numerical RTG Simulation

Initial Pressure (MPa)	Initial Temperature (K)
0.1	298

[a]Initial conditions are uniformly distributed.

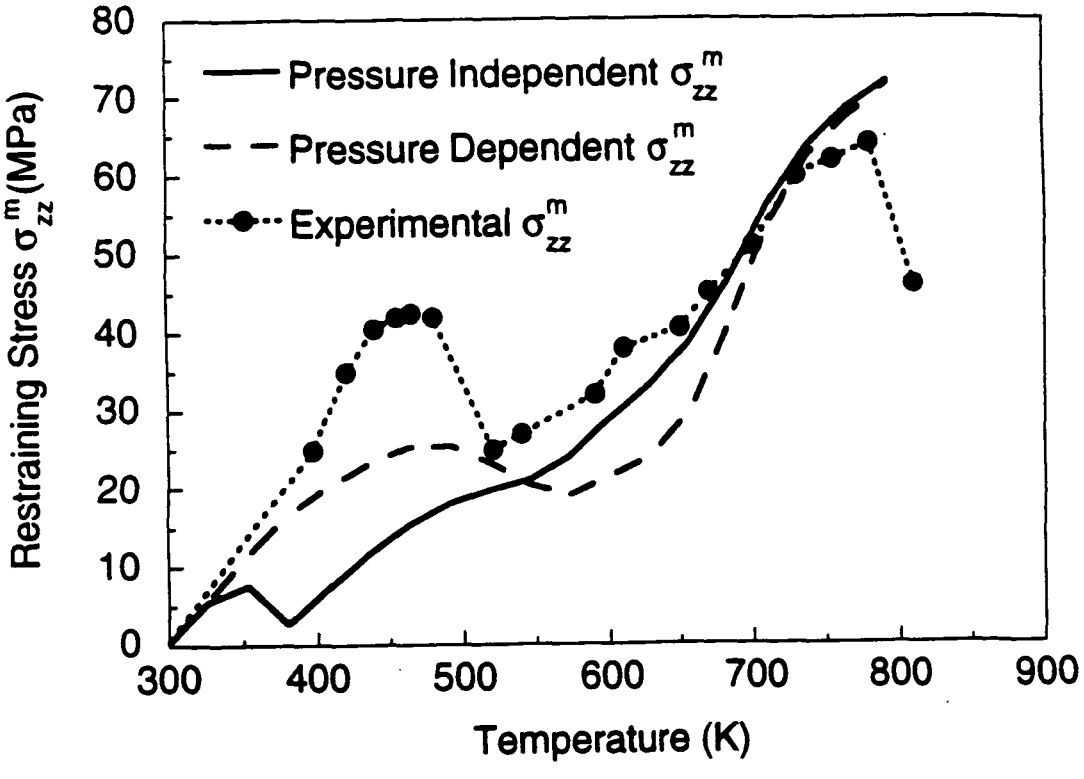

Figure 5-18. Restraining stress vs temperature for pressure-independent Arrhenius reaction model, pressure-dependent Arrhenius reaction model, and measured results [38].

The reason why the pressure-dependent Arrhenius model gives better results than the pressure independent Arrhenius model can be deduced from Figures 5-19 and 5-20, in which the moisture content and internal pressure are plotted with respect to temperature. As shown in Figure 5-19, the moisture content reaches zero at a lower temperature for the pressure-independent Arrhenius model, causing a large amount of vapor generation at relatively low temperature. This results in a much higher internal pressure (about two orders of magnitude) as shown in Figure 5-20. Therefore, the effects of internal pressure on the restraining stress are manifested much sooner in the pressure-independent model than in the pressure-dependent model. This can be seen in Figure 5-18 where the poroelastic material response is seen at a lower temperature. However, the internal pressure does not contribute much to the restraining stress since at low temperatures the material is relatively rigid.

5.4 Performance Study

The results of a performance study of the hybrid algorithm ablative code are presented in this section. All the metrics used to measure the performance of a parallel code have been discussed in Section 4 of Chapter 2. They are used here to determine the performance of the hybrid algorithm on the CM-5 massively parallel computer.

Two different simulation times are used, 0.2 second and 1.0 second. The reason for using two simulation times is to compare the purely parallel scheme with a hybrid scheme. In the 0.2 second simulation, none of the nodes for the mesh sizes used (51, 71, 91, 101, 111, 121, 131, 141, 151, 501, and 1001) has gone unstable, so the solution scheme is purely parallel (explicit scheme). However, in the 1.0 second simulation, some of the nodes

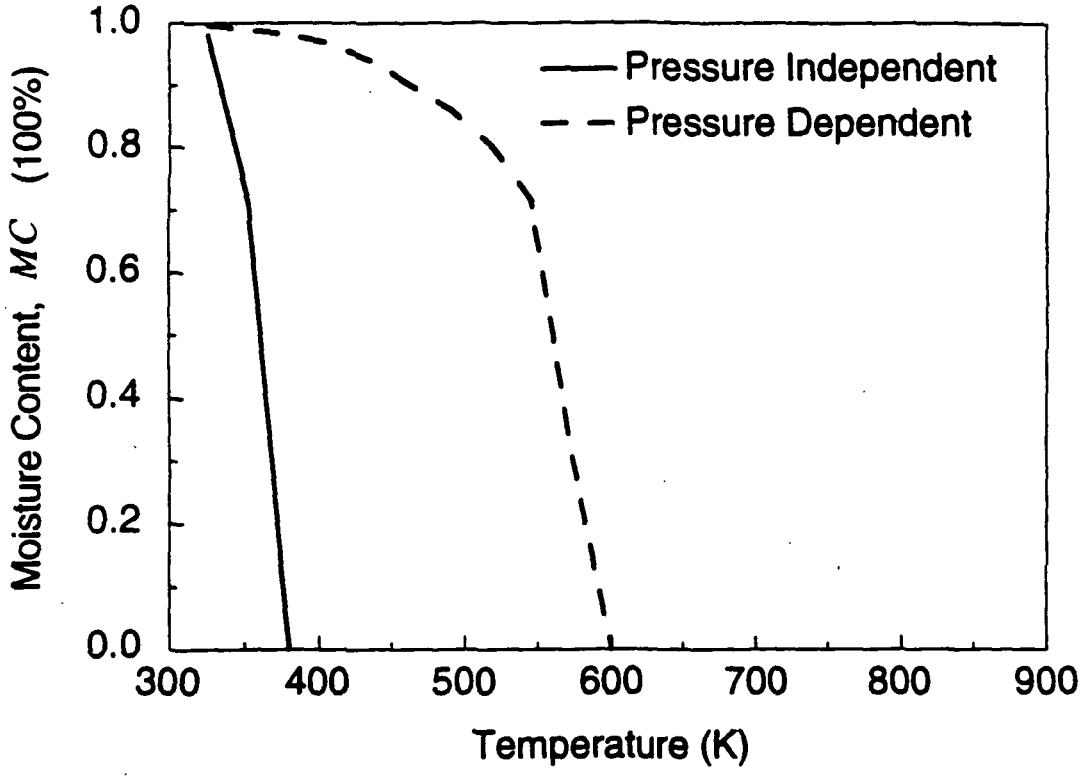

Figure 5-19. Moisture content, *MC*, vs. temperature for pressure-independent Arrhenius reaction model and pressure-dependent Arrhenius reaction model.

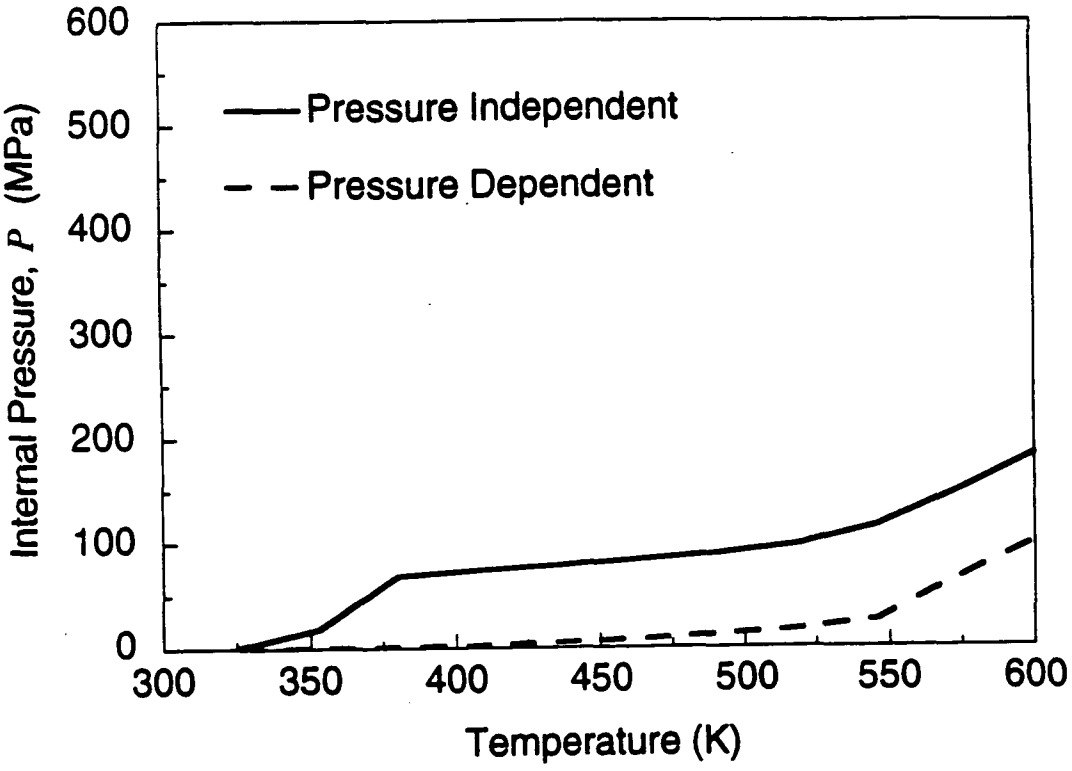

Figure 5-20. Internal pressure, P, vs temperature for pressure-independent Arrhenius reaction model and pressure-independent Arrhenius reaction model.

in the mesh have become unstable and a serial solution scheme (implicit scheme) has to be used. Table 5.8 lists the number of unstable nodes for each mesh size used in the 1.0 second simulation. "Unstable nodes" refers to nodes for which the solution scheme for pressure has switched from the EFDM to the IFDM. The time steps used in both 0.2 and 1.0 second simulations are determined by the third equation in Eqn. 4-41:

$$\Delta t = \frac{\Delta x^2}{\left(\frac{P\gamma}{\phi\mu}\right)} \tag{5-8}$$

As mentioned before in Chapter 4, this time step has been identified to be the most critical one in the ablative problem. The values used for pressure, permeability, porosity, and viscosity in Eqn. 5-8 are based on the typical values that exist in the evaporation zone (Figure 4-6). The reason for using these values is to ensure that the parallel solution scheme (explicit scheme), which incorporates complex physics, remains stable in the evaporation zone. This way, accurate information on pressure can be obtained which is needed to predict failure by ply-lifts. These values are listed in Table 5.9.

The results of the performance study of the 0.2 second simulations are listed in Tables 5.10 and 5.11. The results of the performance study for the 1.0 second simulation are listed in Tables 5.12 and 5.13. Three different numbers of CPUs (1, 32, and 64) are used. 1 CPU is used to simulate the code as if it was executed on a serial machine. In tables 5.10, the following results for the 0.2 second simulation are shown: mesh size, measured clock time for a single, 32, and 64 CPUs, speedup for 32 and 64 CPUs, effective Amdahl's fractions for 32 and 64 CPUs, and effective parallelization for 32 and 64 CPUs. In Table 5.11, the following results for the 0.2 second are shown: efficiency for 32 and 64 CPUs, and excess time for 32 and 64 CPUs.

Table 5.8. Number of Unstable Nodes for Different Mesh Sizes After 1.0 Second of Simulation Time.

Mesh Size	51	71	91	101	111	121	131	141	151	501
Number of Unstable Nodes	1	1	1	1	2	1	2	2	2	6

In Table 5.12, the same results as in Table 5.10 for the 1.0 second simulation are shown. In Table 5.13, the same results as in Table 5.11 for the 1.0 second simulation are shown. Note that for the 1.0 second simulation run (Tables 5.12 and 5.13), performance information for the 1001-noded mesh could not be obtained.

The thing to notice is that for a given simulation time, as the mesh size increases, the parallel algorithm outperforms the serial algorithm. However, when the problem size is small (smaller number of nodes in this case) the serial algorithm is actually better. This can be seen from Table 5.10 for 51 and 71 node mesh sizes where the effective parallelization (p) is actually negative. In Table 5.12, for the 51 nodes mesh size, the effective parallelization is also negative. Another measure that also points out the serial algorithm is better than the parallel one for relatively small problems is the speedup, S. In Table 5.10, for the mesh sizes of 51 and 71 nodes, the speedup in actually less than one which implies that the serial algorithm is actually faster. The same is also seen from Table 5.12 for the mesh size of 51 nodes.

The second thing worth noting is that in this particular case of the hybrid algorithm, larger numbers of CPUs do not always lead to better performance in terms of speedup, S. The results shown in Tables 5.10 and 5.12 indicated that using more CPUs actually slows down the computation. However, this result may not be true as the problem size or the simulation time is increased further. As the problem size or simulation time is increased, more of the CPU time is spent on performing parallel computing. As more of the CPUs are participating in the actual parallel computing, the performance of the hybrid algorithm using 64 CPUs may finally exceed that of the 32 CPUs. Hence, the following observation may be made of the results

Table 5.9. Typical Values of the Parameters In the Evaporation Zone.

P (MPa)	γ (m^2)	ϕ	μ (kg/m sec)
10	$5x10^{-18}$	0.11	$5x10^{-5}$

Table 5.10. 0.2 Second Simulation Results Summary I.

Mesh Size	$T_{N=1}$ (sec)	$T_{N=32}$ (sec)	$T_{N=64}$ (sec)	S_{32}	S_{64}	α_{e32}	α_{e64}	p_{32}	p_{64}
51	1.15	1.81	1.80	0.64	0.64	1.59	1.57	-0.59	-0.57
71	2.00	2.44	2.43	0.82	0.82	1.23	1.22	-0.23	-0.22
91	3.20	3.00	3.05	1.07	1.05	0.93	0.95	0.07	0.05
101	4.00	3.54	3.50	1.13	1.15	0.88	0.86	0.12	0.14
111	4.97	4.08	4.09	1.22	1.22	0.82	0.82	0.18	0.18
121	6.14	4.65	4.63	1.32	1.33	0.75	0.75	0.25	0.25
131	7.53	5.26	5.16	1.43	1.46	0.69	0.68	0.31	0.32
141	9.17	5.63	5.61	1.63	1.64	0.60	0.61	0.40	0.40
151	11.1	6.43	6.23	1.73	1.78	0.57	0.55	0.43	0.45
501	468.6	53.3	54.2	8.79	8.64	0.085	0.10	0.915	0.90
1001	4113	205.6	208.1	20.0	19.8	0.019	0.036	0.981	0.964

Table 5.11. 0.2 Second Simulation Results Summary II.

Mesh Size	e_{32}	e_{64}	t_{ex32} (sec)	t_{ex64} (sec)
51	0.020	0.010	1.77	1.78
71	0.026	0.013	2.38	2.40
91	0.033	0.016	2.90	3.00
101	0.035	0.018	3.41	3.40
111	0.038	0.019	3.93	4.01
121	0.041	0.021	4.46	4.53
131	0.045	0.023	5.02	5.04
141	0.051	0.026	5.34	5.46
151	0.054	0.028	6.08	6.05
501	0.275	0.135	38.7	46.9
1001	0.625	0.310	77.1	143.8

Table 5.12. 1.0 Second Simulation Results Summary I.

Mesh Size	$T_{N=1}$ (sec)	$T_{N=32}$ (sec)	$T_{N=64}$ (sec)	S_{32}	S_{64}	α_{e32}	α_{e64}	p_{32}	p_{64}
51	3.16	4.12	3.97	0.77	0.80	1.31	1.26	-0.31	-0.26
71	7.95	7.18	6.84	1.11	1.16	0.90	0.86	0.10	0.14
91	13.8	10.8	11.0	1.28	1.25	0.78	0.80	0.22	0.20
101	17.6	13.0	12.9	1.35	1.36	0.73	0.73	0.27	0.27
111	22.4	15.9	16.0	1.40	1.40	0.70	0.71	0.30	0.29
121	28.3	18.3	18.5	1.55	1.53	0.63	0.65	0.37	0.35
131	35.6	24.5	21.7	1.45	1.64	0.68	0.60	0.32	0.40
141	44.5	24.7	24.8	1.80	1.79	0.54	0.55	0.46	0.46
151	55.3	28.4	28.3	1.95	1.95	0.50	0.50	0.50	0.50
501	3316	306	319	10.8	10.4	0.06	0.08	0.94	0.92

Table 5.13. 1.0 Second Simulation Results Summary II.

Mesh Size	e_{32}	e_{64}	t_{ex32} (sec)	t_{ex64} (sec)
51	0.024	0.012	4.02	3.92
71	0.035	0.018	6.93	6.72
91	0.040	0.020	10.3	10.8
101	0.042	0.021	12.5	12.7
111	0.044	0.022	15.2	15.7
121	0.048	0.024	17.4	18.0
131	0.045	0.026	23.4	21.1
141	0.056	0.028	23.3	24.1
151	0.061	0.030	26.7	27.5
501	0.340	0.160	202	267

in Tables 5.10 and 5.12. Given the competing mechanisms (overhead costs and actual parallel computation) which determine the net performance, there may be an optimum number of CPUs that should be used to give the best performance for the hybrid algorithm.

The third thing to notice is that the effective parallelization, p, and efficiency, e, are consistently better for the 1.0 second simulation than the 0.2 second simulation (see Tables 5.10 through 5.13). This result is to be expected. As the simulation time increases, the number of time integration operations increases as well. The time integration operations are done in parallel. Therefore, it comes as no surprise that the effective parallelization and efficiency are consistently better for the 1.0 second simulation than for the 0.2 second simulation. Some of the nodes have become unstable in the 1.0 second simulation and thus the serial scheme (implicit scheme) has to be used for some of the calculation. However, the number of unstable nodes is much smaller than the total number of nodes in all cases, so most of the computation is still done by the parallel scheme.

For a large problems, the effective parallelization for the code is approximately one, but the efficiency is nowhere near that. This result indicates that even though the non-parallelizable part of the code is a small percentage of the whole code, it drastically reduces the efficiency of the parallel computation. This result can be attributed to the fact that a large number CPUs sit idle while the non-parallelizable part of the code is running. This result is worse for the case of 64 CPUs than for the case of 32 CPUs since more CPUs sits idle in the 64 CPUs case. Equation 5-9 below gives an expression for the efficiency (e) in terms of the numbers of CPU (N) and the effective parallelization (p):

$$e = \frac{1}{N(1-p)+p} \tag{5-9}$$

The above equation is derived by using Eqns. 2-9 through 2-11. Equation 5-9 is plotted vs p in Figure 5-21 for two different numbers N (32 and 64). As one can see from Figure 5-21, for both 32 and 64 CPUs, e drops very quickly as p decreases. Also note that e is consistently worse for the N = 64 case than the N = 32 case.

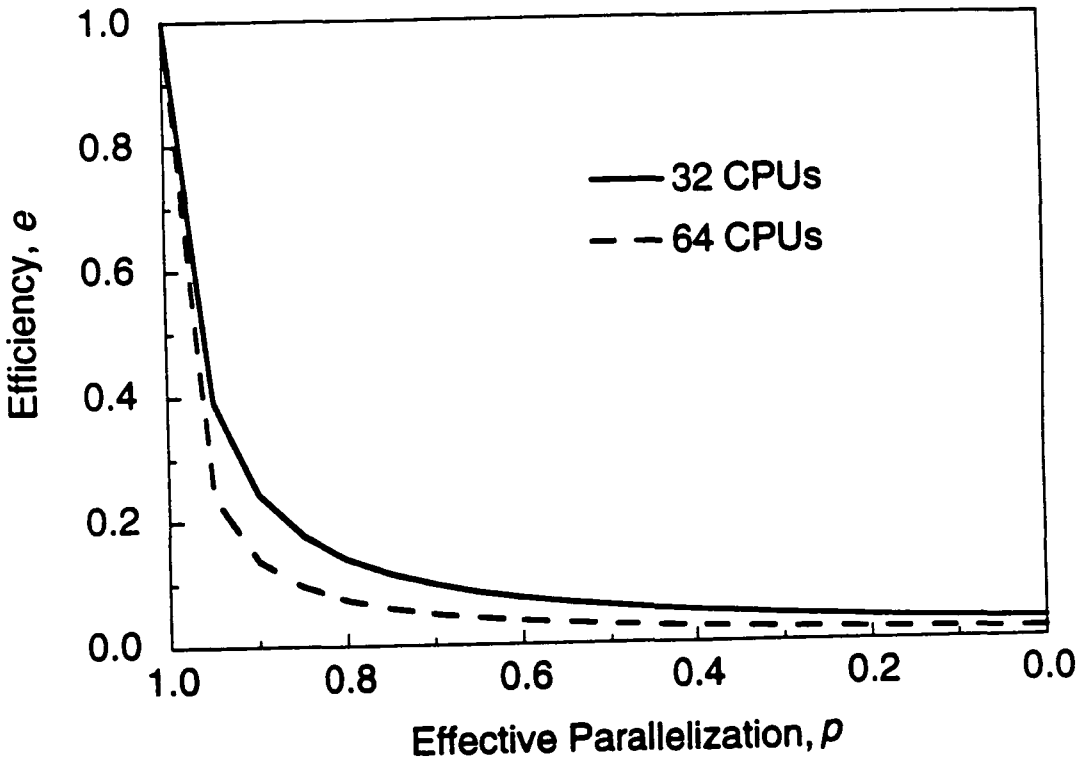

Figure 5-21. Plot of efficiency (e) vs effectively parallelization (p) for two different numbers of CPU (N = 32 and 64).

CHAPTER 6

CONCLUSIONS AND RECOMMENDATIONS

6.1 Conclusions

In this work, numerical solution schemes have been developed on a massively parallel computer (a Thinking Machines CM-5) to solve three problems: (1) transpiration cooling, (2) ablation of a composite plate, and (3) restrained thermal growth (RTG). The numerical solution schemes are based on two types of finite difference method: (1) the explicit finite difference method (EFDM) and (2) the implicit finite difference method (IFDM).

It has been found that a solution scheme based on EFDM requires relatively small time steps for stability but complex physics can be easily incorporated into the solution scheme. On the other hand, a solution scheme based on IFDM can use relatively large time steps and still maintain stability but complex physics are more difficult to incorporate.

An efficient solution scheme called the hybrid algorithm has been developed to combine the strengths and minimize the weaknesses of both solution methods as much as possible. The algorithm was developed by simplifying the physics of the problems judiciously. This simplification of physics was achieved based on observations that different time scales are associated with different physical processes. When the time scale of a physical process was much faster than the others and when transient effects in that process were not important, the response of the process was assumed to be quasistatic. This assumption was used to recast the mathematical

model of the problem. In all three problems considered, the stress response was always quasistatic and its calculation was decoupled from the others; pressure response was sometimes quasistatic and sometimes not. The hybrid algorithm developed picks regions for EFDM and IFDM in the pressure calculations continuously, moving the boundary as the calculation progresses. This solution scheme can be conceptually extended to other engineering problems where more than one time scale are involved due to different physical processes.

The algorithm was verified by comparing the numerical results to the exact solutions for the transpiration cooling problem. From the numerical results of the transpiration cooling problem, the time scales associated with stress, pressure, and temperature responses were compared and discussed as well. The ablation problem demonstrated the importance of advanced physics, such as gas storage terms, to solutions. This problem was also used to analyze the performance of the algorithm. The results of the RTG problem showed that by incorporating enough physics into the algorithm, the complex material responses captured during tests can be reproduced numerically as well.

As expected, it was found that the solutions can be obtained in a shorter wall-clock time using the CM-5 than a single CPU computer. The reduction of wall-clock time is a function of the size and execution time of the problem. The reduction of wall-clock time, however, was not linear with respect to the number of CPUs. For example, when using 32 CPUs, one would expect to obtain the solutions 32 times faster than when using 1 CPU. A speedup of only about 20 times was achieved for 32 CPUs. The speedup did not increase when 64 CPUs were used to solve the problem. This result

seemed to indicate that there is an optimum number of CPUs for a given problem.

By using a standard metric, the hybrid algorithm was found to be highly (94 percent) parallelized. However, this did not directly translate into high efficiency. When the six percent of the algorithm that ran sequentially was running, all but one of the CPUs sit idle and this drastically reduced the efficiency of the overall performance.

6.2 Recommendations

For future work, the following three recommendations are made:

(a) Extend the analysis to more complex geometries. For example, the analysis can be extended to 2-D, 3-D, and axisymmetric problems. EFDM makes this extension relatively easy.

(b) Include more advanced physics such as: an eroding surface, stress-dependent permeability, and Sullivan's thermodynamics model. Their effects on the calculated response of ablative materials can then be studied.

(c) Parallelize the code more by using more advanced system features designed for the CM-5 to obtain higher efficiency. For example, in the ablative composite problem, the IFDM subroutine used for sequential pressure calculation could take advantage of these features to minimize the idle time.

APPENDIX A

EQUATION DERIVATIONS FOR TRANSPIRATION COOLING

A.1 Nondimensional Damping Coefficient (Eqn. 4-10)

Eqn. 4-10 is an expression for the nondimensional damping coefficient. It is derived as follows. We begin with the equations of motion (Eqn. 4-9):

$$\rho_s \frac{\partial^2 u_i}{\partial t^2} + c\frac{\partial u_i}{\partial t} = \sigma_{ij,j} \tag{A-1}$$

Based on the thin plate assumption, the only nonzero spatial derivative is with respect to the z direction. By using this assumption, Eqn. A-1 reduces to the following:

$$\rho_s \frac{\partial^2 u_i}{\partial t^2} + c\frac{\partial u_i}{\partial t} = \sigma_{i,z} \tag{A-2}$$

The displacement vector of the porous solid (u_i) and the through-thickness direction variable (z) are nondimensionalized by the thickness of the plate (h). The nondimensionalized displacement vector and the through-thickness direction variable are:

$$\tilde{u}_i = \frac{u_i}{h} \qquad \tilde{z} = \frac{z}{h} \tag{A-3}$$

The total stress tensor is nondimensionalized by the Young's modulus of the porous solid:

$$\tilde{\sigma}_{iz} = \frac{\sigma_{iz}}{E} \tag{A-4}$$

where $\tilde{\sigma}_{iz}$ is the nondimensionalized total stress tensor. Substituting Eqns. (A-3) and (A-4) into Eqn. (A-2) yields:

$$\frac{\rho_s h^2}{E}\frac{\partial \tilde{u}_i}{\partial t^2} + \frac{ch^2}{E}\frac{\partial \tilde{u}_i}{\partial t} = \tilde{\sigma}_{iz,\tilde{z}} \tag{A-5}$$

Note that the coefficient, $\rho_s h^2/E$, has units of time squared. This coefficient is used to nondimensionalized the time variable:

$$\tilde{t} = \frac{t}{\sqrt{\rho_s h^2/E}} \tag{A-6}$$

Substituting Eqn. A-6 into Eqn. A-5 yields:

$$\frac{\partial \tilde{u}_i}{\partial \tilde{t}^2} + \frac{c}{\sqrt{\rho_s E/h^2}}\frac{\partial \tilde{u}_i}{\partial \tilde{t}} = \tilde{\sigma}_{iz,\tilde{z}} \tag{A-7}$$

Defining the circular natural frequency as [33]:

$$\omega_n = \sqrt{\frac{E}{\rho_s h^2}} \tag{A-8}$$

Then Eqn. A-7 can be written as:

$$\frac{\partial \tilde{u}_i}{\partial \tilde{t}^2} + \frac{c}{\rho_s \omega_n}\frac{\partial \tilde{u}_i}{\partial \tilde{t}} = \tilde{\sigma}_{iz,\tilde{z}} \tag{A-9}$$

According to reference [33], the nondimensional damping coefficient is defined as:

$$2\varsigma = \frac{c}{\rho_s \omega_n} \tag{A-10}$$

By using the above definition, Eqn. 4-10 is obtained easily.

A.2 Derivation of Eqn. 4-16

To derive the first equation in Eqn. 4-16, we make use of the continuity equation (Eqn. 4-14):

$$\frac{\partial m_g}{\partial t} = -\frac{\partial \hat{m}_g}{\partial z} \tag{A-11}$$

m_g is related to ρ_g by the following relation:

$$m_g = \phi \rho_g \tag{A-12}$$

$\hat{m}_g$ is given by Darcy's law (Eqns. 4-2 and 4-3):

$$\hat{m}_g = \frac{-\gamma \rho_g}{\mu} \frac{\partial P}{\partial z} \tag{A-13}$$

By substituting Eqns. A-12 and A-13 into Eqn. A-11, Eqn. A-11 becomes:

$$\frac{\partial (\phi \rho_g)}{\partial t} = \frac{\partial}{\partial z}\left(\frac{\gamma \rho_g}{\mu} \frac{\partial P}{\partial z} \right) \tag{A-14}$$

P is given by the ideal gas law:

$$P = \frac{RT\rho_g}{M} \tag{A-15}$$

Eqn. A-16 is obtained by substituting Eqn. A-15 into Eqn. A-14 for P:

$$\phi \frac{\partial \rho_g}{\partial t} = \frac{\gamma R}{\mu M} \frac{\partial}{\partial z}\left(\rho_g^2 \frac{\partial T}{\partial z} + \rho_g T \frac{\partial \rho_g}{\partial z} \right) \tag{A-16}$$

By expanding the derivative out on the right hand side of Eqn. A-16, the first equation in Eqn. 4-16 is derived:

$$\frac{\partial \rho_g}{\partial t} = \frac{\gamma R}{\phi \mu M}\left[T\left(\frac{\partial \rho_g}{\partial z} \right)^2 + 3\rho_g \left(\frac{\partial T}{\partial z} \right)\left(\frac{\partial \rho_g}{\partial z} \right) + \rho_g T \frac{\partial^2 \rho_g}{\partial z^2} + \rho_g^2 \frac{\partial^2 T}{\partial z^2} \right] \tag{A-17}$$

To derive the second equation in Eqn. 4-16, we make use of the energy equation (Eqn. 4-15):

$$\left(C_{P_s} m_s + C_{P_g} m_g \right) \frac{\partial T}{\partial t} = K_z \frac{\partial^2 T}{\partial z^2} - C_{P_g} \hat{m}_g \frac{\partial T}{\partial z} \tag{A-18}$$

m_s is related to ρ_s by the following relation:

$$m_s = (1 - \phi)\rho_s \tag{A-19}$$

By substituting Eqns. A-12, A-13, and A-19 into Eqn. A-18, the following equation is obtained:

$$\left[C_{P_s}(1-\phi)\rho_s + C_{P_g}\phi\rho_g\right]\frac{\partial T}{\partial t} = K_z\frac{\partial^2 T}{\partial z^2} + C_{P_g}\left(\frac{\gamma\rho_g}{\mu}\frac{\partial P}{\partial z}\right)\frac{\partial T}{\partial z} \qquad \text{(A-20)}$$

By making use of the ideal gas law (Eqn. A-15) for P, the following equation is obtained:

$$\left[C_{P_s}(1-\phi)\rho_s + C_{P_g}\phi\rho_g\right]\frac{\partial T}{\partial t} = K_z\frac{\partial^2 T}{\partial z^2} + C_{P_g}\left\{\frac{\gamma\rho_g}{\mu}\frac{\partial}{\partial z}\left(\frac{RT\rho_g}{M}\right)\right\}\frac{\partial T}{\partial z} \qquad \text{(A-21)}$$

Then by expanding the derivative out for the second term on the right hand side, the second equation in Eqn. 4-16 is obtained:

$$\frac{\partial T}{\partial t} = \frac{1}{\left(C_{P_s}(1-\phi)\rho_s + C_{P_g}\phi\rho_g\right)}\left[K_z\frac{\partial^2 T}{\partial z^2} + \frac{C_{P_g}\gamma R}{\mu M}\left(\rho_g T\frac{\partial\rho_g}{\partial z}\frac{\partial T}{\partial z} + \rho_g^2\left(\frac{\partial T}{\partial z}\right)^2\right)\right] \qquad \text{(A-22)}$$

A.3 Derivation of Equations of Motion (Eqn. 4-18)

To derive Eqn. 4-18, we start with Eqn. 4-17:

$$\begin{aligned}
\rho_s\frac{\partial^2 u_x}{\partial t^2} + c\frac{\partial u_x}{\partial t} &= \sigma_{xx,z} \\
\rho_s\frac{\partial^2 u_y}{\partial t^2} + c\frac{\partial u_y}{\partial t} &= \sigma_{yx,z} \\
\rho_s\frac{\partial^2 u_z}{\partial t^2} + c\frac{\partial u_z}{\partial t} &= \sigma_{zx,z}
\end{aligned} \qquad \text{(A-23)}$$

By using the definition of the total stress tensor (Eqn. 4-11), the three terms on the right hand side of Eqn. A-23 can be written in the following forms:

$$\begin{aligned}
\sigma_{xx} &= \sigma'_{xx} - P \\
\sigma_{xz} &= \sigma'_{xz} \\
\sigma_{yz} &= \sigma'_{yz}
\end{aligned} \qquad \text{(A-24)}$$

By substituting Eqn. A-24 into Eqn. A-23, we obtain another form of Eqn. A-23:

$$\begin{aligned}
\rho_s \frac{\partial^2 u_x}{\partial t^2} + c\frac{\partial u_x}{\partial t} &= \sigma^m_{xz,z} \\
\rho_s \frac{\partial^2 u_y}{\partial t^2} + c\frac{\partial u_y}{\partial t} &= \sigma^m_{yz,z} \\
\rho_s \frac{\partial^2 u_z}{\partial t^2} + c\frac{\partial u_z}{\partial t} &= \sigma^m_{zz,z} + P_{,z}
\end{aligned} \tag{A-25}$$

For the transpiration cooling problem, the strain-displacement relations are:

$$\begin{aligned}
&\varepsilon_{xx} = \varepsilon_{yy} = \varepsilon_{xy} = 0 \\
&\varepsilon_{xz} = \frac{1}{2}\frac{\partial u_x}{\partial z} \qquad \varepsilon_{yz} = \frac{1}{2}\frac{\partial u_y}{\partial z} \qquad \varepsilon_{zz} = \frac{\partial u_z}{\partial z}
\end{aligned} \tag{A-26}$$

By specializing the constitutive relations (Eqn. 4-13) for the transpiration cooling problem, the following constitutive relations are obtained:

$$\begin{aligned}
0 &= S_{xxxx}\sigma^m_{xx} + S_{xxyy}\sigma^m_{yy} + S_{xxyy}\sigma^m_{zz} + \Lambda\Delta P + \alpha\Delta T \\
0 &= S_{xxyy}\sigma^m_{xx} + S_{xxxx}\sigma^m_{yy} + S_{xxyy}\sigma^m_{zz} + \Lambda\Delta P + \alpha\Delta T \\
\varepsilon_{zz} &= S_{xxyy}\sigma^m_{xx} + S_{xxyy}\sigma^m_{yy} + S_{xxxx}\sigma^m_{zz} + \Lambda\Delta P + \alpha\Delta T \\
0 &= 2\left(S_{xxxx} - S_{xxyy}\right)\sigma^m_{xy} \\
\gamma_{xz} &= 2\left(S_{xxxx} - S_{xxyy}\right)\sigma^m_{xz} \\
\gamma_{yz} &= 2\left(S_{xxxx} - S_{xxyy}\right)\sigma^m_{yz}
\end{aligned} \tag{A-27}$$

where γ_{xz} and γ_{yz} are engineering shear strains. For an isotropic solid, S_{xxxx} and S_{xxyy} are given by the following equations:

$$S_{xxxx} = \frac{1}{E} \qquad S_{xxyy} = \frac{-\upsilon}{E} \tag{A-28}$$

By substituting the strain-displacement relation (Eqn. A-26) into the constitutive relations, Eqn. A-27 can be written as:

$$
\begin{aligned}
0 &= S_{xxxx}\sigma^m_{xx} + S_{xxyy}\sigma^m_{yy} + S_{xxyy}\sigma^m_{zz} + \Lambda\Delta P + \alpha\Delta T \\
0 &= S_{xxyy}\sigma^m_{xx} + S_{xxxx}\sigma^m_{yy} + S_{xxyy}\sigma^m_{zz} + \Lambda\Delta P + \alpha\Delta T \\
\frac{\partial u_z}{\partial z} &= S_{xxyy}\sigma^m_{xx} + S_{xxyy}\sigma^m_{yy} + S_{xxxx}\sigma^m_{zz} + \Lambda\Delta P + \alpha\Delta T \\
0 &= 2\left(S_{xxxx} - S_{xxyy}\right)\sigma^m_{xy} \\
\frac{\partial u_x}{\partial z} &= 2\left(S_{xxxx} - S_{xxyy}\right)\sigma^m_{xz} \\
\frac{\partial u_y}{\partial z} &= 2\left(S_{xxxx} - S_{xxyy}\right)\sigma^m_{yz}
\end{aligned}
\qquad \text{(A-29)}
$$

The first two equations in Eqn. A-29 are used to solve for σ^m_{xx} and σ^m_{yy}. The resulting two equations for σ^m_{xx} and σ^m_{yy} are then substituted into the third equation in Eqn. A-29. The resulting equation is then solved for σ^m_{zz}. The last two equations in Eqn. A-29 are used to solve for σ^m_{xz} and σ^m_{yz}. The three equations for σ^m_{xz}, σ^m_{yz}, and σ^m_{zz} are shown below:

$$
\begin{aligned}
\sigma^m_{xz} &= Du_{x,z} \\
\sigma^m_{yz} &= Du_{y,z} \\
\sigma^m_{zz} &= \frac{1}{A}\left(u_{z,z} - B\Delta P - C\Delta T\right)
\end{aligned}
\qquad \text{(A-30)}
$$

where the constants A, B, C, and D are defined in Eqn. 4-19. By substituting Eqn. A-30 into Eqn. A-25, the desired result (Eqn. 4-18) is obtained:

$$
\begin{aligned}
\rho_s \frac{\partial^2 u_x}{\partial t^2} + c\frac{\partial u_x}{\partial t} &= Du_{x,zz} \\
\rho_s \frac{\partial^2 u_y}{\partial t^2} + c\frac{\partial u_y}{\partial t} &= Du_{y,zz} \\
\rho_s \frac{\partial^2 u_z}{\partial t^2} + c\frac{\partial u_z}{\partial t} &= \frac{1}{A}\left(u_{z,zz} - (A+B)\Delta P_{,z} - C\Delta T_{,z}\right)
\end{aligned}
\qquad \text{(A-31)}
$$

APPENDIX B

DERIVATION OF EQUATIONS FOR ABLATIVE COMPOSITE PLATE

B.1 Derivation of Governing Equation for Pressure (Eqn. 4-27)

We begin the derivation of the governing equation for pressure (Eqn. 4-27) with the 1-D gas continuity equation for the ablative composite plate problem (Eqn. 4-23):

$$\frac{\partial m_g}{\partial t} = -\frac{\partial \hat{m}_g}{\partial z} + r_p + r_c \tag{B-1}$$

m_g is given by the ideal gas law as:

$$m_g = \frac{P\phi M}{RT} \tag{B-2}$$

$\hat{m}_g$ is given by the Darcy's law as:

$$\hat{m}_g = -\frac{\rho_g \gamma}{\mu}\frac{\partial P}{\partial z} \tag{B-3}$$

By substituting Eqns. B-2 and B-3 into Eqn. B-1, the following equation is obtained:

$$\frac{\partial}{\partial t}\left(\frac{P\phi M}{RT}\right) = \frac{\partial}{\partial z}\left(\frac{\rho_g \gamma}{\mu}\frac{\partial P}{\partial z}\right) + r_p + r_c \tag{B-4}$$

Another form of the ideal is gas law is given below:

$$\rho_g = \frac{PM}{RT} \tag{B-5}$$

By substituting Eqn. B-5 into Eqn. B-4 for ρ_g, the following equation is obtained:

$$\frac{\partial}{\partial t}\left(\frac{P\phi M}{RT}\right)=\frac{\partial}{\partial z}\left(\frac{PM}{RT}\frac{\gamma}{\mu}\frac{\partial P}{\partial z}\right)+r_p+r_e \tag{B-6}$$

M and R are the only constants in Eqn. B-6. By expanding Eqn. B-6 out and rearranging the terms, the governing equation for pressure (Eqn. 4-27) is obtained:

$$\begin{aligned}\frac{\partial P}{\partial t}=&\frac{T}{\phi}\frac{\partial}{\partial z}\left(\frac{\gamma}{T\mu}\right)P\frac{\partial P}{\partial z}+\frac{\gamma}{\phi\mu}\frac{\partial P}{\partial z}\frac{\partial P}{\partial z}+\frac{P\gamma}{\phi\mu}\frac{\partial^2 P}{\partial z^2}+\frac{RT}{\phi M}\left(r_p+r_e\right)\\&+\frac{P}{T}\frac{\partial T}{\partial t}-\frac{P}{\phi}\frac{\partial \phi}{\partial t}\end{aligned} \tag{B-7}$$

B.2 Derivation of Governing Equation for Temperature (Eqn. 4-28)

We begin the derivation of the governing equation for temperature (Eqn. 4-28) with the energy equation (Eqn. 4-8):

$$\left(\sum_i C_{P_i}m_i\right)\frac{\partial T}{\partial t}=\frac{\partial}{\partial z}\left(K_z\frac{\partial T}{\partial z}\right)-C_{P_g}\hat{m}_g\frac{\partial T}{\partial z}+\sum_k R_k\overline{Q}_k-\sum_i r_i h_i \tag{B-8}$$

Recall that in the ablative composite plate analysis, the system consists of four components: (1) porous virgin solid, (2) porous charred solid, (3) absorbed moisture, and (4) flowing gases (evaporation gas and pyrolysis gas). By specializing the energy equation to this system, we obtained the following equation:

$$\begin{aligned}&\left(C_{P_s}m_s+C_{P_c}m_c+C_{P_l}m_l+C_{P_g}m_g\right)\frac{\partial T}{\partial t}=\\&\frac{\partial}{\partial z}\left(K_z\frac{\partial T}{\partial z}\right)-C_{P_g}\hat{m}_g\frac{\partial T}{\partial z}+R_c\overline{Q}_c+R_w\overline{Q}_w-\\&\left(r_s h_s+r_c h_c+r_l h_l+r_e h_e+r_p h_p\right)\end{aligned} \tag{B-9}$$

r_s, r_c, r_l, r_e, and r_p are given in reference [12] by the following expressions:

$$
\begin{aligned}
r_s &= -\rho_s R_c \\
r_c &= \rho_c R_c \\
r_p &= (\rho_s - \rho_c) R_c \\
r_e &= R_w m_s + (MC)\rho_s R_c \\
r_l &= -\left[R_w m_s + (MC)\rho_s R_c\right]
\end{aligned}
\tag{B-10}
$$

Eqns. B-3 , B-5, and B-10 are substituted into Eqn. B-9 to give the governing equation for temperature (Eqn. 4-28):

$$
\frac{\partial T}{\partial t} = \frac{1}{\eta}\left[\frac{C_{P_g} m_g \gamma}{\phi \mu}\frac{\partial P}{\partial z}\frac{\partial T}{\partial z} + \frac{\partial K_z}{\partial z}\frac{\partial T}{\partial z} + K_z \frac{\partial^2 T}{\partial z^2} + R_c Q_c + R_w Q_w\right] \tag{B-11}
$$

Q_c and Q_w are given by the following expressions:

$$
\begin{aligned}
Q_c &= \left(\overline{Q}_c + \rho_s h_s - \rho_c h_c - (MC)\rho_s h_e + (MC)\rho_s h_l - (\rho_s - \rho_c) h_p\right) \\
Q_w &= \left(\overline{Q}_w - m_s h_e + m_s h_l\right)
\end{aligned}
\tag{B-12}
$$

APPENDIX C

IMPLEMENTATION OF FOUR-STEP ARRHENIUS REACTION MODEL

In this appendix, explicit expressions for r_e and r_p are given. They are used in Eqn. 4-43 to compute the pressure distribution in the numerical simulation of restrained thermal growth (RTG) testing.

The mass generation rates of evaporation and pyrolysis gases, r_e and r_p, are given by the following expressions:

$$\begin{aligned} r_e &= R_w m_s + (MC)\rho_s R_c \\ r_p &= R_w(\rho_s - \rho_c) \end{aligned} \tag{C-1}$$

R_w and R_c are given by the following expressions:

$$\begin{aligned} R_w &= \overline{v}_1^w R_1 + \overline{v}_2^w R_2 \\ R_c &= \overline{v}_2^c R_2 + \overline{v}_3^c R_3 + \overline{v}_4^c R_4 \end{aligned} \tag{C-2}$$

where R_k (k=1, 2, 3, and 4) are given by Eqn. 4-57 and the values for the constants in Eqn. 4-57 are listed in Tables 4.1- 4.3. $\overline{v}_k^w$ and $\overline{v}_k^c$ are given by the following expressions:

$$\begin{aligned} \overline{v}_k^w &= \frac{m_{l_k}}{m_{l_0}} \\ \overline{v}_k^c &= \frac{m_{c_k}}{m_{c_0}} \end{aligned} \tag{C-3}$$

where m_{l_k} is the mass of absorbed moisture converted to gas by the completion of the kth reaction, m_{c_k} is the mass of porous charred solid created by the completion of the kth reaction, m_{l_0} is the total mass of absorbed

moisture converted to gas, and m_{c_o} is the total mass of the porous charred solid created by all reactions. The values of m_{l_k}, m_{c_t}, m_{l_o}, and m_{c_o} used in the RTG numerical simulation are listed in Table C-1[40].

Table C-1 Reaction Constants

Reaction Number	m_{l_t} kg/m^3	m_{c_t} kg/m^3
1	22	0
2	27	80
3	0	618
4	0	314
	m_{l_o} =47 kg/m^3	m_{c_o} =1012 kg/m^3

APPENDIX D

MATERIAL PROPERTIES OF FM5055

Table D-1. Material properties of FM5055 carbon-phenolic - permeability data for various values of char volume, v_c.

	Permeability Units ($m^2 \times 10^{-18}$)		
Char Volume, v_c	γ_{x_1}	γ_{x_2}	γ_{x_3}
0.0	5	9	0.01
0.1	6	13	0.23
0.2	15	15	0.90
0.3	39	39	3.5
0.4	112	112	13
0.5	320	320	50
0.6	940	940	190
0.7	2700	2700	720
0.8	7800	7800	2700
0.9	23000	23000	10000
1.0	65000	65000	39000

Table D-2. Material properties of FM5055 carbon phenolic - thermal conductivity data for various values of temperature, T.

	Thermal Conductivity Units ($W/m^2°C$)		
Temp., T (°C)	K_{x_1}	K_{x_2}	K_{x_3}
0	1.08	1.08	0.80
200	1.50	1.50	0.93
275	1.55	1.55	1.00
400	1.55	1.55	1.00
600	1.55	1.55	1.00
827	1.55	1.55	1.00
1227	2.59	2.59	1.60
1727+	3.00	3.00	1.60

Table D-3. Material properties of FM5055 carbon phenolic - specific heat capacity[a] for virgin and charred solid for various values of temperature, T.

	Specific Heat Units (J/kg°C)	
Temp., T (°C)	C_{P_v}	C_{P_c}
0	880	1800
100	1165	1800
200	1450	1800
300	1475	1800
400	1500	1800
700	1500	1800
800+	1500	1900

[a]The specific heat capacities for the flowing gas and absorbed moisture are assumed to be constant. In computation, the value used for the flowing gas is C_{P_g}=2000 J/kg°C and the value used for the absorbed moisture is C_{P_l}=4200 J/kg°C.

Table D-4. Viscosities of flowing gas for two values of temperature, T.

Viscosities Units (kg/m sec x 10^{-5})	
Temp., (°C)	Viscosity, μ
-273	0.7975
2727	8.2975

Table D-5. Temperature at which reactions begin and end (°C) and heats of reaction (MJ/kg) for various values of pressure.

Moisture evaporation reaction				Charring Reaction		
P(MPa)	T_{bw}	T_{ew}	Q_w	T_{bc}	T_{ec}	Q_c
0.1	100	150	-2.251	400	538	-0.234
0.2	120	170	-2.197	400	538	-0.234
0.5	152	202	-2.108	400	538	-0.234
1.0	180	230	-2.008	400	538	-0.234
2.0	212	262	-1.871	400	538	-0.234
5.0	264	314	-1.623	400	538	-0.234
10.0	311	361	-1.351	400	538	-0.234
20.0+	367	417	-0.551	400	538	-0.234

Table D-6. Material Properties of FM5055 - Young's and shear Moduli for various values of temperature, T.

	Moduli Units (GPa)					
Temp.(°C)	E_{x_1}	E_{x_2}	E_{x_3}	$G_{x_1x_2}$	$G_{x_2x_3}$	$G_{x_1x_3}$
23	17.93	17.93	16.55	6.90	5.17	5.17
93	17.24	17.24	12.41	6.55	4.83	4.83
204	13.10	13.10	5.52	3.24	2.76	2.76
315	8.96	8.96	1.38	2.21	1.03	1.03
426	6.90	6.90	0.55	1.86	1.03	1.03
537	6.55	6.55	0.34	1.72	1.10	1.10
815	7.58	7.58	0.34	1.79	1.38	1.38
1093	8.27	8.27	0.34	1.93	1.52	1.52
1648	6.90	6.90	0.34	2.07	1.52	1.52
2204	2.76	2.76	0.34	1.52	1.24	1.24
2760	1.38	1.38	0.34	0.69	0.48	0.48

Table D-7. Material properties of FM5055 - Poisson's ratios for various values of temperature, T.

Temp. (°C)	$\upsilon_{x_1x_2}$	$\upsilon_{x_2x_3}$	$\upsilon_{x_1x_3}$
23	0.32	0.24	0.24
93	0.29	0.20	0.20
204	0.23	0.18	0.18
315	0.13	0.12	0.12
426	0.08	0.06	0.06
537	0.06	0.05	0.05
815	0.05	0.01	0.01
1093	0.06	0.01	0.01
1648	0.07	0.01	0.01
2204	0.08	0.02	0.02
2760	0.09	0.03	0.03

Table D-8. Material properties of FM5055 - thermal expansions $\upsilon_{x_1x_3}$ for various values of temperature, T.

	Thermal Expansion Units (m/m x 10^{-3})			
T(°C)	ΔT(°C)	$\alpha_{x_1}\Delta T$	$\alpha_{x_2}\Delta T$	$\alpha_{x_3}\Delta T$
23	0	0.0	0.0	0.0
93	60	0.8	0.8	1.0
204	181	1.6	1.6	4.0
315	292	2.0	2.0	7.0
426	403	2.0	2.0	10.0
537	514	1.0	1.0	13.0
815	792	0.0	0.0	12.0
1093	1060	0.0	0.0	-6.0
1648	1625	2.5	2.5	-21.0
2204	2181	17.5	17.5	-30.0
2760	2737	28.0	28.0	-60.0

APPENDIX E

ROTATIONAL MATRICES

Four matrices are listed in this appendix. The first two ($\mathbf{R}_z$ and $\mathbf{R}_y$) are associated with rotating second order tensorial quantities about the z and y axes. The latter two ($\mathbf{X}_z$ and $\mathbf{X}_y$) are associated specifically with rotating engineering strains about the z and y axes. Rotation of stress, engineering strain, and stiffness and compliance using engineering strain are illustrated here. Some relations used in this thesis are expressed in terms of tensor strain and tensor stiffness and compliance; the relation between tensor and engineering quantities is discussed thoroughly in [39].

$$\mathbf{R}_z = \begin{bmatrix} m^2 & n^2 & 0 & 0 & 0 & 2mn \\ n^2 & m^2 & 0 & 0 & 0 & -2mn \\ 0 & 0 & 1 & 0 & 0 & 0 \\ 0 & 0 & 0 & m & -n & 0 \\ 0 & 0 & 0 & n & m & 0 \\ -mn & mn & 0 & 0 & 0 & m^2 - n^2 \end{bmatrix} \tag{E-1}$$

$$\mathbf{R}_y = \begin{bmatrix} m'^2 & 0 & n'^2 & 0 & -2m'n' & 0 \\ 0 & 1 & 0 & 0 & 0 & 0 \\ n'^2 & 0 & m'^2 & 0 & 2m'n' & 0 \\ 0 & 0 & 0 & m' & 0 & n' \\ m'n' & 0 & -m'n' & 0 & m'^2 - n'^2 & 0 \\ 0 & 0 & 0 & -n' & 0 & m' \end{bmatrix} \tag{E-2}$$

$$\mathbf{X}_z = \begin{bmatrix} m^2 & n^2 & 0 & 0 & 0 & mn \\ n^2 & m^2 & 0 & 0 & 0 & -mn \\ 0 & 0 & 1 & 0 & 0 & 0 \\ 0 & 0 & 0 & m & -n & 0 \\ 0 & 0 & 0 & n & m & 0 \\ -2mn & 2mn & 0 & 0 & 0 & m^2 - n^2 \end{bmatrix} \tag{E-3}$$

$$\mathbf{X}_y = \begin{bmatrix} m'^2 & 0 & n'^2 & 0 & -m'n' & 0 \\ 0 & 1 & 0 & 0 & 0 & 0 \\ n'^2 & 0 & m'^2 & 0 & m'n' & 0 \\ 0 & 0 & 0 & m' & 0 & n' \\ 2m'n' & 0 & -2m'n' & 0 & m'^2 - n'^2 & 0 \\ 0 & 0 & 0 & -n' & 0 & m' \end{bmatrix} \tag{E-4}$$

where m is short for $cos\theta$, n is short for $sin\theta$, m' is short for $cos\Phi$, and n' is short for $sin\Phi$.

To illustrate how the matrices in Eqns. E-1 and E-2 are used to relate off-axis second order tensors to on-axis second order tensors, we use the two matrices to relate the on-axis $(x_1 - x_2 - x_3)$ stress tensor to the off-axis $(x - y - z)$ stress tensor:

$$\sigma_{off} = \mathbf{R}_y \mathbf{R}_z \sigma_{on} \tag{E-5}$$

where σ_{off} and σ_{on} are given by the following equations:

$$\sigma_{off} = \begin{bmatrix} \sigma_{xx} \\ \sigma_{yy} \\ \sigma_{zz} \\ \sigma_{xz} \\ \sigma_{yz} \\ \sigma_{xy} \end{bmatrix} \qquad \sigma_{on} = \begin{bmatrix} \sigma_{x_1x_1} \\ \sigma_{x_2x_2} \\ \sigma_{x_3x_3} \\ \sigma_{x_1x_3} \\ \sigma_{x_2x_3} \\ \sigma_{x_1x_2} \end{bmatrix} \tag{E-6}$$

Similarly, the on-axis engineering strains can be related to off-axis engineering strain by the same expression shown in Eqn. E-5, except now $\mathbf{R}_y$ and $\mathbf{R}_z$ are replaced by $\mathbf{X}_z$ and $\mathbf{X}_y$, respectively.

Eqn. E-7 gives the expression for relating the off-axis compliance tensor to the on-axis compliance tensor:

$$\mathbf{S}_{off} = \mathbf{R}_y \mathbf{R}_z \mathbf{S}_{on} \mathbf{X}_z^{-1} \mathbf{X}_y^{-1} \tag{E-7}$$

where $\mathbf{X}_z^{-1}$ is the inverse matrix for $\mathbf{X}_z$ and $\mathbf{X}_y^{-1}$ is the inverse matrix for $\mathbf{X}_y$.

The inverse matrices for $\mathbf{R}_z$, $\mathbf{R}_y$, $\mathbf{X}_z$, and $\mathbf{X}_y$ are listed below in Eqns. E-8 through E-11:

$$\mathbf{R}_z^{-1} = \begin{bmatrix} m^2 & n^2 & 0 & 0 & 0 & -2mn \\ n^2 & m^2 & 0 & 0 & 0 & 2mn \\ 0 & 0 & 1 & 0 & 0 & 0 \\ 0 & 0 & 0 & m & n & 0 \\ 0 & 0 & 0 & -n & m & 0 \\ mn & -mn & 0 & 0 & 0 & m^2 - n^2 \end{bmatrix} \tag{E-8}$$

$$\mathbf{R}_y^{-1} = \begin{bmatrix} m'^2 & 0 & n'^2 & 0 & 2m'n' & 0 \\ 0 & 1 & 0 & 0 & 0 & 0 \\ n'^2 & 0 & m'^2 & 0 & -2m'n' & 0 \\ 0 & 0 & 0 & m' & 0 & -n' \\ -m'n' & 0 & m'n' & 0 & m'^2 - n'^2 & 0 \\ 0 & 0 & 0 & n' & 0 & m' \end{bmatrix} \tag{E-9}$$

$$\mathbf{X}_z^{-1} = \begin{bmatrix} m^2 & n^2 & 0 & 0 & 0 & -mn \\ n^2 & m^2 & 0 & 0 & 0 & mn \\ 0 & 0 & 1 & 0 & 0 & 0 \\ 0 & 0 & 0 & m & n & 0 \\ 0 & 0 & 0 & -n & m & 0 \\ 2mn & -2mn & 0 & 0 & 0 & m^2 - n^2 \end{bmatrix} \tag{E-10}$$

$$\mathbf{X}_y^{-1} = \begin{bmatrix} m'^2 & 0 & n'^2 & 0 & m'n' & 0 \\ 0 & 1 & 0 & 0 & 0 & 0 \\ n'^2 & 0 & m'^2 & 0 & -m'n' & 0 \\ 0 & 0 & 0 & m' & 0 & -n' \\ -2m'n' & 0 & 2m'n' & 0 & m'^2 - n'^2 & 0 \\ 0 & 0 & 0 & n' & 0 & m' \end{bmatrix} \tag{E-11}$$

To relate the off-axis stress tensor to the on-axis stress tensor, the following expression is used:

$$\sigma_{on} = \mathbf{R}_z^{-1}\mathbf{R}_y^{-1}\sigma_{off} \qquad \text{(E-12)}$$

Eqn. E-12 is also valid for all second order tensorial quantities. To relate the off-axis engineering strain tensor to the off-axis engineering tensor, replace $\mathbf{R}_z^{-1}$ and $\mathbf{R}_y^{-1}$ by $\mathbf{X}_z^{-1}$ and $\mathbf{X}_y^{-1}$, respectively The off-axis compliance tensor is related to the on-axis tensor by the following equation:

$$\mathbf{S}_{on} = \mathbf{R}_z^{-1}\mathbf{R}_y^{-1}\mathbf{S}_{off}\mathbf{X}_y\mathbf{X}_z \qquad \text{(E-13)}$$

APPENDIX F

INPUT AND OUTPUT FILES OF TRANSPIRATION COOLING PROGRAM

There is one input file and two output files for the transpiration cooling program. The name of the input file is "input.txt." The names of the two output files are "outputs1.txt" and "outputs2.txt." The formats and contents of these file are shown below. Line numbers are shown for convenience; they are not included in the input files. Input values should be valid FORTRAN real or integer numbers. Lines are separated by carriage returns, values on the same line should be separated by spaces.

F.1 Format of Input File "Input.txt"

Input.txt

Line numbers:

1. CPS

   Specific heat capacity of porous solid (J/kg °C)

2. CPG

   Specific heat capacity of gas (J/kg °C)

3. PORE

   Porosity of porous solid

4. COND

   Area-average coefficient of thermal conductivity (W/m^2 °C)

5. PERM

   Permeability of porous solid (m^2)

6. MU

   Gas viscosity (kg/m sec)

7. MW

   Molecular weight of gas (kg/kmole)

8. E

   Young's modulus of porous solid (Pa)

9. v

   Poisson's ratio of porous solid

10. ALPHA

    Coefficient of thermal expansion of porous solid (1/°C)

11. DAMP

    Damping coefficient (N sec/m^4)

12. MS

    Density of porous solid (kg/m^3)

13. XO

    Thickness of plate (m)

14. NODE

    Number of nodes in the mesh

15. DT

    Time step (sec)

16. TIME

    Length of simulation time (sec)

17. TA

    Boundary temperature at z = 0.0 cm (Pa)

18. TB

    Boundary temperature at z = XO cm (Pa)

19. PA

    Boundary pressure at z = 0.0 cm (Pa)

20. PB

    Boundary pressure at z = XO cm (Pa)

21. T1B

    Surface traction T_1^b at z = XO cm (Pa)

22. T2B

    Surface traction T_2^b at z = XO cm (Pa)

23. T3B

    Surface traction T_3^b at z = XO cm (Pa)

24. TINIT

    Initial temperature value (°C)

25. PINIT

    Initial pressure value (Pa)

F.2 Format of Ouput Files

Outputs1.txt

Col. 1	Col. 2	Col. 3	Col. 4	Col. 5	Col. 6	Col. 7
Position	Pressure	Temp.	Displ. u_1	Displ. u_2	Displ. u_3	Sim.
(m)	(Pa)	(K)	(m)	(m)	(m)	Time (sec)

Outputs2.txt

Col. 1	Col. 2	Col. 3	Col. 4	Col. 5	Col. 6	Col. 7
Position	σ^m_{xx}	σ^m_{yy}	σ^m_{xz}	σ^m_{yz}	σ^m_{zz}	Sim.
(m)	(Pa)	(Pa)	(Pa)	(Pa)	(Pa)	Time(sec)

APPENDIX G

INPUT AND OUTPUT FILES OF ABLATIVE COMPOSITE PLATE PROGRAM

The input files for the ablative composite plate program consists of six categories: (1) general information, (2) mesh information, (3) material properties, (4) restart conditions, (5) boundary conditions, and (6) chemical reaction constants. In the general information category, there is one input file named: "input.in." In the mesh information category, there is one input file named: "mesh.in." In the material properties category, there are ten input files named: (1) "alpha.in," (2) "cond.in," (3) "denpor.in," (4) "mole.in," (5) "poisson.in," (6) "shear.in," (7) "speh.in," (8) "perm.in,"(9) "visc.in," and (10) "young.in." In the initial conditions category, there are four input files named: (1) "rechar.in," (2) "remois.in," (3) "retpinit.in," and (4) "trate.in." These files can also be used to restart runs, and are refered to as restart files. In the boundary conditions category, there are three input files named: (1) "heatb.flux," (2) "presb.in," and (3) "traction.in." In the chemical reaction category, there are two input files named: (1) "cchar1.in," and (2) "wchar2.in." There are six output files from the program and they are: (1) "char.out," (2) "press.out," (3) "stability.out" (4) "stress.out," (5) "temp.out," and (6) "volat.out." The contents and formats of the input and output files are shown in the following sections. Line numbers are shown for convienience; they are not included in the input files. Input values should be valid FORTRAN real

or integer numbers. Lines are separted by carriage returns, values on the same line should be separted by spaces.

G.1 General Information Input File

input.in

Line numbers:

1. SEP2

   Number of nodes using IFDM solution scheme for pressure (Eqn. 4-46)

2. SEPT2

   Number of nodes using 2nd EFDM solution scheme for temperature (Eqn. 4-48)

3. NF

   Number of specified output time

4. TSPEC(1)

   First specified time (sec)

   .

   .

   .

   TSPEC(NF)

   NFth specified time (sec)

5. GN

   Number of char volumes at which the permeability of the porous solid are specified

6. KN

   Number of temperatures at which the coefficients of thermal conductivity are specified

7. NET

   Number of temperatures at which mechanical properties are specified

8. NEC

   Number of char volumes at which mechanical properties are specified

9. CN

   Number of temperatures at which the specific heats of the porous virgin and charred solids are specified

10. MN

    Number of temperatures at which the gas viscosities are specified

11. TYPEC

    Type of char reaction. For ablative composite plate problem enter 1

12. TYPEW

    Type of evaporation reaction. For ablative composite plate problem enter 2

13. CHEMNC

    Number of pressures at which the values of Q_w, T_{bw}, and T_{ew} are specified

14. NODE

    Number of nodes in the mesh

G.2 Mesh Information Input File

mesh.in

1. XO

   Thickness of plate (m)

2. PT

   Ply angle (degrees)

3. FT

   Fiber angle (degrees)

4. DT

   Time step (sec)

5. TIME

   Length of simulation time (sec)

G.3 Material Properties Input Files

alpha.in (coefficients of thermal expansion of porous solid damaged and undamaged (1/°C))

Undamaged			Damaged		
Col. 1	Col. 2	Col. 3	Col. 4	Col. 5	Col. 6
$\alpha_{x_1x_1}(T_1, v_1)$	$\alpha_{x_2x_2}(T_1, v_1)$	$\alpha_{x_3x_3}(T_1, v_1)$	$\alpha_{x_1x_1}(T_1, v_1)$	$\alpha_{x_2x_2}(T_1, v_1)$	$\alpha_{x_3x_3}(T_1, v_1)$
.	.	.	.	.	.
.	.	.	.	.	.
$\alpha_{x_1x_1}$	$\alpha_{x_2x_2}$	$\alpha_{x_3x_3}$	$\alpha_{x_1x_1}$	$\alpha_{x_2x_2}$	$\alpha_{x_3x_3}$
(T_{NET}, v_1)	(T_{NET}, v_1)	(T_{NET}, v_1)	(T_{NET}, v_1)	(T_{NET}, v_1)	(T_{NET}, v_1)
.	.	.	.	.	.
.	.	.	.	.	.
$\alpha_{x_1x_1}$	$\alpha_{x_2x_2}$	$\alpha_{x_3x_3}$	$\alpha_{x_1x_1}$	$\alpha_{x_2x_2}$	$\alpha_{x_3x_3}$
(T_1, v_{NEC})	(T_1, v_{NEC})	(T_1, v_{NEC})	(T_1, v_{NEC})	(T_1, v_{NEC})	(T_1, v_{NEC})
.	.	.	.	.	.
.	.	.	.	.	.
$\alpha_{x_1x_1}$	$\alpha_{x_2x_2}$	$\alpha_{x_3x_3}$	$\alpha_{x_1x_1}$	$\alpha_{x_2x_2}$	$\alpha_{x_3x_3}$
(T_{NET}, v_{NEC})	(T_{NET}, v_{NEC})	(T_{NET}, v_{NEC})	(T_{NET}, v_{NEC})	(T_{NET}, v_{NEC})	(T_{NET}, v_{NEC})

cond.in (coefficients of thermal conductivity of porous solid damaged and undamaged (W/m^2 °C) and temperatures at which the coefficients of thermal conductivity are specified (°C))

	Undamaged			Damaged		
Col. 1	Col. 2	Col. 3	Col. 4	Col. 5	Col. 6	Col. 7
$K_{x_1}(T_1)$	$K_{x_2}(T_1)$	$K_{x_3}(T_1)$	$K_{x_1}(T_1)$	$K_{x_2}(T_1)$	$K_{x_3}(T_1)$	T_1
.	.	.	.	.	.	.
$K_{x_1}(T_{KN})$	$K_{x_2}(T_{KN})$	$K_{x_3}(T_{KN})$	$K_{x_1}(T_{KN})$	$K_{x_2}(T_{KN})$	$K_{x_3}(T_{KN})$	T_{KN}

denpor.in (intrinsic densities of virgin and charred solids (kg/m^3), porosity of virgin and charred solids, and initial moisture content)

Col. 1	Col. 2	Col. 3	Col. 4
ρ_s	ρ_c	ϕ_s	ϕ_c
MC_o			

mole.in (Molecular weights of evaporation and pyrolysis gases (kg/kmole))

Col. 1	Col. 2
M_e	M_p

poisson.in (Poisson's ratio of porous solid undamaged and damaged)

Undamaged			Damaged		
Col. 1	Col. 2	Col. 3	Col. 4	Col. 5	Col. 6
$\upsilon_{x_1x_2}(T_1,\nu_1)$	$\upsilon_{x_2x_3}(T_1,\nu_1)$	$\upsilon_{x_1x_3}(T_1,\nu_1)$	$\upsilon_{x_1x_2}(T_1,\nu_1)$	$\upsilon_{x_2x_3}(T_1,\nu_1)$	$\upsilon_{x_1x_3}(T_1,\nu_1)$
.	.	.	.	.	.
.	.	.	.	.	.
$\upsilon_{x_1x_2}$	$\upsilon_{x_2x_3}$	$\upsilon_{x_1x_3}$	$\upsilon_{x_1x_2}$	$\upsilon_{x_2x_3}$	$\upsilon_{x_1x_3}$
(T_{NET},ν_1)	(T_{NET},ν_1)	(T_{NET},ν_1)	(T_{NET},ν_1)	(T_{NET},ν_1)	(T_{NET},ν_1)
.	.	.	.	.	.
.	.	.	.	.	.
$\upsilon_{x_1x_2}$	$\upsilon_{x_2x_3}$	$\upsilon_{x_1x_3}$	$\upsilon_{x_1x_2}$	$\upsilon_{x_2x_3}$	$\upsilon_{x_1x_3}$
(T_1,ν_{NEC})	(T_1,ν_{NEC})	(T_1,ν_{NEC})	(T_1,ν_{NEC})	(T_1,ν_{NEC})	(T_1,ν_{NEC})
.	.	.	.	.	.
.	.	.	.	.	.
$\upsilon_{x_1x_2}$	$\upsilon_{x_2x_3}$	$\upsilon_{x_1x_3}$	$\upsilon_{x_1x_2}$	$\upsilon_{x_2x_3}$	$\upsilon_{x_1x_3}$
$(T_{\text{NET}},\nu_{\text{NEC}})$	$(T_{\text{NET}},\nu_{\text{NEC}})$	$(T_{\text{NET}},\nu_{\text{NEC}})$	$(T_{\text{NET}},\nu_{\text{NEC}})$	$(T_{\text{NET}},\nu_{\text{NEC}})$	$(T_{\text{NET}},\nu_{\text{NEC}})$

shear.in (Shear moduli of porous solid undamaged and damaged (Pa))

Undamaged			Damaged		
Col. 1	Col. 2	Col. 3	Col. 4	Col. 5	Col. 6
$G_{x_1x_2}(T_1,\nu_1)$	$G_{x_2x_3}(T_1,\nu_1)$	$G_{x_2x_3}(T_1,\nu_1)$	$G_{x_1x_2}(T_1,\nu_1)$	$G_{x_2x_3}(T_1,\nu_1)$	$G_{x_2x_3}(T_1,\nu_1)$
.	.	.	.	.	.
.	.	.	.	.	.
$G_{x_1x_2}$	$G_{x_2x_3}$	$G_{x_2x_3}$	$G_{x_1x_2}$	$G_{x_2x_3}$	$G_{x_2x_3}$
(T_{NET},ν_1)	(T_{NET},ν_1)	(T_{NET},ν_1)	(T_{NET},ν_1)	(T_{NET},ν_1)	(T_{NET},ν_1)
.	.	.	.	.	.
.	.	.	.	.	.
$G_{x_1x_2}$	$G_{x_2x_3}$	$G_{x_2x_3}$	$G_{x_1x_2}$	$G_{x_2x_3}$	$G_{x_2x_3}$
(T_1,ν_{NEC})	(T_1,ν_{NEC})	(T_1,ν_{NEC})	(T_1,ν_{NEC})	(T_1,ν_{NEC})	(T_1,ν_{NEC})
.	.	.	.	.	.
.	.	.	.	.	.
$G_{x_1x_2}$	$G_{x_2x_3}$	$G_{x_2x_3}$	$G_{x_1x_2}$	$G_{x_2x_3}$	$G_{x_2x_3}$
$(T_{\text{NET}},\nu_{\text{NEC}})$	$(T_{\text{NET}},\nu_{\text{NEC}})$	$(T_{\text{NET}},\nu_{\text{NEC}})$	$(T_{\text{NET}},\nu_{\text{NEC}})$	$(T_{\text{NET}},\nu_{\text{NEC}})$	$(T_{\text{NET}},\nu_{\text{NEC}})$

speh.in (specific heats for porous virgin and charred solids (J/kg °C), temperatures at which the specific heats of porous solid are specified (°C), specific heats for absorbed moisture, evaporation gas, and pyrolysis gas (J/kg °C))

Col. 1	Col. 2	Col. 3
$C_{P_v}(T_1)$	$C_{P_c}(T_1)$	T_1
.	.	.
$C_{P_v}(T_{CN})$	$C_{P_c}(T_{CN})$	T_{CN}
C_{P_l}	C_{P_g}	C_{P_v}

perm.in (permeability of porous solid undamaged and damaged (m^2) and char volumes at which the permeability of porous solid are specified)

Undamaged			Damaged			
Col. 1	Col. 2	Col. 3	Col. 4	Col. 5	Col. 6	Col. 7
$\gamma_{x_1}(\nu_1)$	$\gamma_{x_2}(\nu_1)$	$\gamma_{x_3}(\nu_1)$	$\gamma_{x_1}(\nu_1)$	$\gamma_{x_2}(\nu_1)$	$\gamma_{x_3}(\nu_1)$	ν_1
.	.	.	.	.	.	.
$\gamma_{x_1}(\nu_{GN})$	$\gamma_{x_2}(\nu_{GN})$	$\gamma_{x_3}(\nu_{GN})$	$\gamma_{x_1}(\nu_{GN})$	$\gamma_{x_2}(\nu_{GN})$	$\gamma_{x_3}(\nu_{GN})$	ν_{GN}

visc.in (viscosities of evaporation and pyrolysis gas (kg/m sec) and temperatures at which the gas viscosities are specified (°C))

Col. 1	Col. 2	Col. 3
$\mu_e\,(T_1)$	$\mu_p\,(T_1)$	T_1
.	.	.
$\mu_e\,(T_{MN})$	$\mu_p\,(T_{MN})$	T_{MN}

young.in (Young's moduli of porous solid undamaged and damaged (Pa), char volumes at which Young's moduli are specified, and temperatures at which Young's moduli are specified (°C))

	Undamaged			Damaged		
v_1						
T_1						
	$E_{x_1}(T_1, v_1)$	$E_{x_2}(T_1, v_1)$	$E_{x_3}(T_1, v_1)$	$E_{x_1}(T_1, v_1)$	$E_{x_2}(T_1, v_1)$	$E_{x_3}(T_1, v_1)$
.	.	.	.	.	.	.
T_{NET}						
	E_{x_1}	E_{x_2}	E_{x_3}	E_{x_1}	E_{x_2}	E_{x_3}
	(T_{NET}, v_1)	(T_{NET}, v_1)	(T_{NET}, v_1)	(T_{NET}, v_1)	(T_{NET}, v_1)	(T_{NET}, v_1)
.	.	.	.	.	.	.
v_{NEC}						
T_1						
	E_{x_1}	E_{x_2}	E_{x_3}	E_{x_1}	E_{x_2}	E_{x_3}
	(T_1, v_{NEC})	(T_1, v_{NEC})	(T_1, v_{NEC})	(T_1, v_{NEC})	(T_1, v_{NEC})	(T_1, v_{NEC})
.	.	.	.	.	.	.
T_{NET}						
	E_{x_1}	E_{x_2}	E_{x_3}	E_{x_1}	E_{x_2}	E_{x_3}
	(T_{NET}, v_{NEC})	(T_{NET}, v_{NEC})	(T_{NET}, v_{NEC})	(T_{NET}, v_{NEC})	(T_{NET}, v_{NEC})	(T_{NET}, v_{NEC})

G.4 Restart Conditions Input Files

rechar.in (restart through-thickness char and solid volume distributions)

VC(1)

.

.

VC(NODE)

VS(1)

.

.

VS(NODE)

remois.in (restart through-thickness moisture content distribution)

MC(1)

.

.

MC(NODE)

retpinit.in (restart through-thickness temperature (°C) and pressure (Pa) distributions)

T(1)

.

.

T(NODE)

P(1)

.

.

P(NODE)

trate.in (restart through-thickness rate of temperature change ($\partial T/\partial t$) distribution (°C/sec))

TRATE(1)

.

.

TRATE(NODE)

G.5 Boundary Conditions Input Files

heatb.flux (radiative and convective heat transfer parameters at exposed surface)

Col. 1	Col. 2	Col. 3	Col. 4	Col. 5	Col. 6	Col. 7	Col. 8
σ	ε	α	T_e	h_{c1}	h_{c2}	$T_{\infty 1}$	$T_{\infty 2}$
W/m^2K^4			K	W/m^2K	W/m^2K	K	K

presb.in (pressure at exposed surface and ambient pressure (Pa))

Col. 1	Col. 2	Col. 3
P_{b1}	P_{b2}	P_{amb}

traction.in (surface tractions at exposed surface (Pa))

T1B

T2B

T3B

G.6 Chemical Reaction Constants Input Files

cchar1.in (chemical reaction constants for pyrolysis reaction)

Col. 1	Col. 2	Col. 3
T_{bc} (°C)	T_{ec} (°C)	Q_c (J)

wchar2.in (chemical reaction constants for evaporation reaction and pressures at which these reaction constants are specified)

Col. 1	Col. 2	Col. 3	Col. 4
T_{bw} (P_1) (°C)	T_{ew} (P_1) (°C)	Q_w (P_1) (J)	P_1 (Pa)
.	.	.	. .
T_{bw} (P_{CHEMNC}) (°C)	T_{ew} (P_{CHEMNC}) (°C)	Q_w (P_{CHEMNC}) (J)	P_{CHEMNC} (Pa)

G.7 Output Files

char.out (through-thickness distributions of virgin and charred solid volumes at specified output times (sec))

Col. 1	Col. 2	Col. 3	Col. 4
Position (m)	v_s (TSPEC(1))	v_c (TSPEC(1))	TSPEC(1)
.	.	.	.
.	.	.	.
Position (m)	v_s(TSPEC(NF))	v_c (TSPEC(NF))	TSPEC(NF)

press.out (through-thickness distributions of pressure (Pa) at specified output times and time step used in simulation (sec))

Col. 1	Col. 2	Col. 3	Col. 4
Position (m)	*P* (TSPEC(1))	TSPEC(1)	DT
.	.	.	.
.	.	.	.
Position (m)	*P* (TSPEC(NF))	TSPEC(NF)	DT

stability.out (number of nodes that used Eqn. 4-46 and Eqn. 4-48 to calculate pressure and temperature at specified output times (sec))

Col. 1	Col. 2	Col. 3
SEP2 (TSPEC(1))	SEPT2 (TSPEC(1))	TSPEC(1)
.	.	.
.	.	.
SEP2 (TSPEC(NF))	SEPT2 (TSPEC(NF))	TSPEC(NF)

stress.out (through-thickness distributions of stress (Pa) at specified output times (sec))

Col. 1	Col. 2	Col. 3	Col. 4	Col. 5	Col. 6	Col. 7	Col. 8
Position (m)	$\sigma^m_{x_1x_1}$	$\sigma^m_{x_1x_2}$	$\sigma^m_{x_1x_3}$	$\sigma^m_{x_2x_2}$	$\sigma^m_{x_2x_3}$	$\sigma^m_{x_3x_3}$	TSPEC(1)
.	.	.	.	.	.	.	.
.	.	.	.	.	.	.	.
Position (m)	$\sigma^m_{x_1x_1}$	$\sigma^m_{x_1x_2}$	$\sigma^m_{x_1x_3}$	$\sigma^m_{x_2x_2}$	$\sigma^m_{x_2x_3}$	$\sigma^m_{x_3x_3}$	TSPEC (NF)

temp.out (through-thickness distributions of temperature (°C) at specified output times (sec))

Col. 1	Col. 2	Col. 3
Position (m)	*T* (TSPEC(1))	TSPEC(1)
.	.	.
.	.	.
Position (m)	*T* (TSPEC(NF))	TSPEC(NF)

volat.out (through-thickness distributions of moisture content and rate of temperature change (°C/sec) at specified output times (sec))

Col. 1	Col. 2	Col. 3	Col. 4
Position (m)	MC (TSPEC(1))	$\partial T/\partial t$ (TSPEC(1))	TSPEC(1)
.	.	.	.
.	.	.	.
Position (m)	MC (TSPEC(NF))	$\partial T/\partial t$ (TSPEC(NF))	TSPEC(NF)

APPENDIX H

INPUT AND OUTPUT FILES OF RTG PROGRAM

All of the input files of the RTG program have the same formats and contents as the input files of the ablative composite plate program except for the input file named: "input.in." Also, for the RTG program, there is one additional input file named: "rtg.in." The RTG program has the same output files as the ablative composite plate program. The formats and contents of the two input files (input.in and rtg.in) are shown in the following sections.

H.1 Formats and Contents of Input File "input.in"

input.in

1. TRATESPEC

   Constant heating rate (°C/sec)

2. SEP2

   Number of nodes using IFDM solution scheme for pressure (Eqn. 4-46)

3. SEPT2

   Number of nodes using 2nd EFDM solution scheme for temperature (Eqn. 4-48)

4. NF

   Number of specified output time

5. TSPEC(1)

   First specified output time (sec)

TSPEC(NF)

NFth specified output time (sec)

6. GN

   Number of char volumes at which the permeability of the porous solid are specified

7. KN

   Number of temperatures at which coefficients of thermal conductivity are specified

8. NET

   Number of temperatures at which mechanical properties are specified

9. NEC

   Number of char volumes at which mechanical properties are specified

10. CN

    Number of temperatures at which the specific heats of the porous virgin and charred solids are specified

11. MN

    Number of temperatures at which the gas viscosities are specified

12. TYPEC

    Type of char reaction. For RTG problem enter 4

13. TYPEW

    Type of evaporation reaction. For RTG problem enter 4

14. NRTG

    Types of chemical reactions

15. PRSP

    Number of pressure at which the reaction constants are specified

16 NODE

Number of nodes in the mesh

H.2 Formats and Contents of Input File "rtg.in"

rtg.in

P_1

First pressure at which the Arrhenius constants are specified (Pa)

.

.

P_{PRSP}

PRSPth pressure at which the Arrhenius constants are specified (Pa)

$E_{a_1}(P_1)$

Activation energy (J/mole) for first type chemical reaction evaluated at first specified pressure

.

$E_{a_1}(P_{PRSP})$

Activation energy (J/mole) for first type chemical reaction evaluated at PRSPth specified pressure

.

.

$E_{a_{NRTG}}(P_1)$

Activation energy (J/mole) for NRTGth type chemical reaction evaluated at first specified pressure

.

$E_{a_{NRTG}}(P_{PRSP})$

Activation energy (J/mole) for the NRTGth type chemical reaction evaluated at PRSPth specified pressure

3.

Col. 1	Col. 2	Col. 4	Col. 5
A_{o_1} (1/sec)	n_1	m_{i_1} (kg/m^3)	m_{c_1} (kg/m^3)
.	.	.	.
.	.	.	. .
$A_{o_{NRTG}}$ (1/sec)	n_{NRTG}	$m_{c_{NRTG}}$ (kg/m^3)	$m_{i_{NRTG}}$ (kg/m^3)

Rest of Arrhenius constants for NRTG types of chemical reactions

REFERENCES

1. *CM FORTRAN Manual*, Thinking Machines Corporation, Cambridge, MA, Jan., 1993.

2. Keyhani, M., and Krishnan, V., "A One-Dimensional Model for the Thermal Responses of a Decomposing Polymer", in *AMD-Vol. 136*, ASME, 1992, pp. 89-90.

3. Moyer, C. B., and Rindal, R., "An Analysis of the Coupled Chemically Reacting Boundary Layer and Charring Ablator", NASA CR 1061, NASA contractor report, 1963.

4. Henderson, J. B., Wiebelt, J.A., and Tant, M.R., "A Model for Thermal Response of a Polymer Composite Materials and Experimental Verifications", *Journal of Composite Materials*, Vol. 19, 1985, pp. 579-595.

5. Stokes, E., "The Effect of Moisture on the Mechanical and Thermal Response of FM5055 Carbon Phenolic Composites", Report No. SRI-EAS-87-1244-6245-6, Southern Research Institute, Birmingham, AL., 1987.

6. Hubbert, T. E., "Mechanical Properties of FM5055 Baseline Carbon Phenolic", Report No. SRI-MIME-89-1149-6071-23, Southern Research Institute, Birmingham, AL., 1990.

7. McManus, H. L., and Springer, G.S., "High Temperature Thermomechanical Behavior of Carbon-Phenolic and Carbon-Carbon Composites, II. Results", *Journal of Composite Materials*, Vol. 26, No. 2, 1992, pp. 230-255.

8. Florio, J., Henderson, J.B., and Test, F.L., "Experimental Determination of Volumetric Heat Transfer Coefficient in Decomposing Polymer Composites", *ASME Winter Annual Meeting*, San Francisco, CA, 1989, pp. 51-60.

9. Florio, J., Henderson, J.B., and Miriyale, S.K., "Effect of Non-Thermal Equilibrium on the Thermally-Induced Response of Polymer Composite Exposed to High Heat Fluxes", in *Computational Mechanics of Porous Materials and Their Thermal Decomposition*, Vol. AMD-VOl. 136, ASME, 1992, pp. 91-101.

10. Henderson, J. B., and Wiecek, T.E., "A Mathematical Model to Predict the Thermal Response of Decomposing, Expanding Polymer Composites", *Journal of Composite Materials*, Vol. 21, 1987, pp. 373-393.

11. Kuhlmann, T. L., "Thermo-Chemical-Structural Analysis of Carbon-Phenolic Composites with Pore Pressure and Pyrolysis Effects", University of California, Davis, CA, Ph.D. Thesis, 1991.

12. McManus, H. L. N., "High Temperature Thermo-Mechanical Behavior of Carbon-Phenolic and Carbon-Carbon Composites", Stanford University, Stanford, CA, Ph.D. Thesis, 1990.

13. Sullivan, R. M., "A Finite Element Model for Thermo-Chemically Decomposing Polymers", Pennsylvannia State University, University Park, PA, Ph.D. Thesis, 1990.

14. Weiler, F. C., "Advanced Governing Equations", *JANNAF Rocket Nozzle Technology Subcommittee Meeting*, NASA Marshall, AL., Nov. 5-7 1991.

15. Weiler, F. C., "Fully Coupled Thermo-Poro-Elasto Governing Equations", in *Computational Mechanics of Porous Materials and Their Thermal Decomposition*, Vol. AMD-Vol. 136, ASME, 1992, pp. 1-25.

16. Katsube, N., "The Anisotropic Thermo-Mechanical Constitutive Theory for a Fluid-Filled Porous Material with Solid/Fluid Outer Boundary", *International Journal of Solids and Structures*, Vol. 24, No. 4, 1988, pp. 375-380.

17. Biot, M. A., "General Theory of Three-Dimensional Consolidation", *Journal of Applied Physics*, Vol. 12, 1941, pp. 155-164.

18. Biot, M. A., "Theory of Elasticity and Consolidation for a Porous Anisotropic Solid", *Journal of Applied Physics*, Vol. 26, No. Feb., 1955, pp. 182-185.

19. Biot, M. A., and Willis, D.G., "The Elastic Coefficients of the Theory of Consolidation", *Journal of Applied Mechanics*, Vol. 24, No. Dec., 1957, pp. 594-601.

20. Katsube, N., "The Constitutive Theory for Fluid-Filled Porous Materials", *Journal of Applied Mechanics*, Vol. 52, No. Mar., 1985, pp. 185-189.

21. Katsube, N., and Carrol, M.M., "The Modified Mixture Theory for Fluid-Filled Porous Materials: Theory", *Journal of Applied Mechanics*, Vol. 54, No. Mar., 1987, pp. 35-46.

22. Tai, D., "A New Model of Moisture Evaporation in Composite Materials in Rapid Temperature Rise Environment", Massachussetts Institute of Technology, S.M. Thesis, 1994.

23. Sullivan, R. M., "On the Constitutive Relations for the High-Temperature, Nonlinear Expansion of Polymeric Composites", in *Material Nonlinear Effects*, Vol. AMD-Vol. 159, ASME, 1993, pp. 331-342.

24. Sullivan, R. M., *A Thermodynamic Model for Hygrothermal Behavior in Polymer Composites*. 1994, to be published in AIAA Journal.

25. Stokes, E. H., "Equilibrated Moisture Content of Several Carbon Phenolics and Their Relationship to Resin, Fiber and Interface Properties", *AIAA 32nd Structures, Structural Dynamics and Materials Conference*, Baltimore, MD, 1991.

26. Smith, G. D., *Numerical Solution of Partial Differential Equations: Finite Difference Methods*, Oxford University Press, Oxford, 1985, pp. 24-28.

27. Agarwal, R. K., "Parallel Computers and Large Problem in Industry", *Computational Methods in Applied Sciences, the First European Conference on Numerical Methods in Engineering*, Brussels, Belgium, Sept. 7-11 1992, pp. 1-11.

28. Shia, D. a. M., H.L., "A Massively Parallel Computational Approach to Coupled Thermoelastic/Porous Gas Flow Problems", *JANNAF Conference Proceeding*, Renton, WA, Jan., 1994.

29. Amdahl, G., "The Validity of the Single-Processor Approach to Achieving Large-Scale Computing Capabilities", *Proceeding of the American Federation of Information Processing Societies*, 1967, pp. 484-485.

30. Plaskacz, E. J., Ramirez, M.R., and Gupta, S., "Non-linear Explicit Transient Finite Element Analysis on the Intel Delta", *Computing Systems in Engineering*, Vol. 5, No. 1, 1994, pp. 1-17.

31. Scheidegger, A. E., *The Physics of Flow through Porous Media*, 3rd ed. University Toronto Press, 1974.

32. Reynolds, W. C., and Perkins, H.C., *Engineering Thermodynamics*, McGraw-Hill, New York, 1977.

33. Meirovitch, L., *Analytical Methods in Vibrations*, 1st ed. Macmillian Publishing Co., Inc., 1967, pp. 8-9.

34. McManus, H. L., "Application of Poroelasticity Theory of Decomposing Composites", *33rd AIAA/ASME/ASCE/AHS/ASC Structures, Structural Dynamics, and Materials Conference*, Dallas, TX, April 1992, pp. 3172-3178.

35. Anderson, D. A., Tannehill, J.C., and Pletcher, R.H., *Computational Fluid Mechanics and Heat Transfer*, 1st ed. Hemisphere Publishing Corp., 1984.

36. Press, W. H., Flannery, B.P., Teukolsky, S.A., and Vetterling, W.T., *Numerical Recipes, "FORTRAN Version"*, Cambridge University Press, New York, 1989, pp. 484-488.

37. Shia, D., and McManus, H.L., "Modeling of Composite Ablators Using Massively Parallel Computers", *35th AIAA/ASME/ASCE/AHS/ASC Structures, Structural Dynamics, and Materials Conference*, New Orleans, LA, April 1994.

38. Sullivan, R. M., and Salamon, N.J., "A Finite Element Method for the Thermochemical Decomposition of Polymeric Materials - II. Carbon Phenolic", *International Journal of Engineering Science*, Vol. 30, No. 7, 1992, pp. 939-951.

39. Tsai, S. W., *Theory of Composites Design*, 1st ed. THINK COMPOSITES, 1992, pp. 2-8.

40. McManus, H. L., "Critical Factors in the Analysis of Decomposing Composites", in *Computational Mechanics of Porous Materials and Their Thermal Decomposition*, ASME, 1992, pp. 113-119.

41. Reynolds, W. C., *Thermodynamics Properties in SI*, Department of Mechanical Engineering, Stanford University, Stanford, CA, 1979, pp. 104-105.

42. Glass, D., *Exact Solution for Through-Thickness Temperature Distribution in Transpiration Cooling Problem*. 1993.

43. McManus, H. L., "Exact Solutions to Quasi-steady State Internal Gas Flow Problems", *1992 JANNAF Rocket Nozzle Technology Subcommittee Meeting*, Lockheed Missiles and Space Company, Sunnyvale, CA, Dec. 8-10, 1992.

44. Boas, M. L., *Mathematical Methods in the Physical Sciences*, John Wiley & Sons, 1966, pp. 550-552.